Numerical Simulation of Hypersonic Flow Over a Blunt Delta Wing
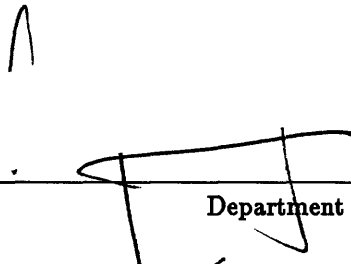
by

Kuok-Ming Lee

S.B. Aeronautics and Astronautics, Massachusetts Institute of Technology, 1988

SUBMITTED IN PARTIAL FULFILLMENT OF THE
REQUIREMENTS FOR THE DEGREE OF
Master of Science
in
Aeronautics and Astronautics
at the
Massachusetts Institute of Technology

October 1989

©1989, Massachusetts Institute of Technology

Signature of Author _____
Department of Aeronautics and Astronautics
October 13, 1989

Certified by _____
Professor Earll M. Murman
Thesis Supervisor, Department of Aeronautics and Astronautics

Accepted by _____
Professor Harold Y. Wachman
Chairman, Department Graduate Committee

Numerical Simulation of Hypersonic Flow Over a Blunt Delta Wing

by

Kuok-Ming Lee

Submitted to the Department of Aeronautics and Astronautics on
October 13, 1989
in partial fulfillment of the requirements for the Master of Science in
Aeronautics and Astronautics.

Abstract

Euler and Navier-Stokes results are presented for a blunt delta wing at Mach
7.15 and 30° angle of attack. The viscous calculations were done at a Reynolds
number based on chord of 5.85×10^6 with freestream and wall temperatures set to
$74K$ and $288K$ respectively.

The inviscid simulations were carried out using a finite volume, central difference
code written by Roberts [21] and Goodsell [7]. The Navier-Stokes results were
obtained on the semi-implicit extension of the inviscid code, developed by Loyd
[17].

The inviscid results showed a strong shock on the windward side of the wing
at a stand-off angle of about $-5°$ from the body. As the flow traverses around the
leading edge it accelerates strongly through an expansion fan. On the upper surface
of the wing, separation occurs at about 60% span resulting in a region of reverse
cross stream flow.

The viscous calculations display a similar shock structure. Furthermore the
boundary layer on the windward side is thin and variations in the circumferential
direction are small. The flow on the leeward side of the wing separates in 2 places.
The primary separation occurs just inside of the leading edge, and the secondary
separation region is located further inboard.

The inviscid C_L and C_D are 0.547 and 0.383 respectively, whereas the viscous
values are 0.547 and 0.386. The viscous component contributes only an insignificant
2.32×10^{-3} to the C_D of the Navier-Stokes calculations.

Thesis Supervisor: Dr. Earll M. Murman,

Professor of Aeronautics and Astronautics.

Acknowledgements

I would like to express my sincere and heartfelt gratitude to all my teachers whose dedication and hard work helped pave my academic path. I owe special thanks to Professor Earll M. Murman whose patience and guidence were instrumental in kindling the flame of my curousity and whose encouragement gave me the courage to challange my own limitations. To him and others like him, may God's blessing be always upon you.

I must also thank my family who bore the difficulty of separation for the last five years and whose love and support gave purpose to all my endeavors.

For the last year I was blessed with the companionship of Low Su-Lin. She was a comfort in difficult times and a joy always.

A special thanks to all my friends, without whom life at MIT would be utterly miserable.

Nomenclature

$[A]$	x-component of flux Jacobian
$[B]$	y-component of flux Jacobian
$[C]$	z-component of flux Jacobian
Cp	specific heat capacity at constant pressure
C_p	pressure coefficient
$\mathbf{D}$	dissipation vector
E	total energy per unit mass
$\vec{\mathbf{F}}$	flux vector
$\mathbf{F}$	x-component of flux vector
$\mathbf{G}$	y-component of flux vector
$\mathbf{H}$	z-component of flux vector
H	total enthalpy per unit mass
$[I]$	identity matrix
P	pressure
Pr	Prandtl number
$\mathbf{R}$	residual
R	Reimann invarients
Re	Reynolds number
S	surface area
V	volume
$\mathbf{W}$	state vector
a	speed of sound
$\vec{i}$	unit vector in the x-direction
$\vec{j}$	unit vector in the y-direction
$\vec{k}$	unit vector in the z-direction
k	thermal conductivity
$\vec{n}$	surface normal vector

q_i	i-component of the heat flux vector
t	time
u	x-component of velocity
v	y-component of velocity
w	z-component of velocity
α	angle of attack
δ	second difference operator
ϵ_{IS}	implicit smoothing coefficient
ϵ_{RS}	residual smoothing coefficient
η	body normal computational coordinate
γ	ratio of specific heats
κ	grid conductivity function
μ	coefficient of viscosity
ρ	density
τ_{ij}	stress tensor
ξ	streamwise computational coordinate
ς	circumferential computational coordinate

Superscript

T	transpose

Subscripts

f	face number

I	invicid
n	normal
V	viscous
$-$	incoming
$+$	outgoing

Contents

List of Figures

11

13

Chapter 1

Introduction

'Faster is better' is an age-old belief. The quest for higher speeds is an ongoing process with no visible end in sight. However it would be short-sighted to deride this quest as frivolous or vain, for without the speed afforded by today's transport technology, the world would be a much more splintered place. Where it once took years and considerable risks to traverse the continents and oceans, the jets of today accomplish this task within hours in comfort and safety. Nevertheless the quest is on for even faster modes of transport, and vehicles like the National Aerospace Plane (NASP) and the HERMES aircraft represent the beginnings of a new age in aerospace.

In the realm of space exploration, high speed travel is an absolute necessity. Maneuvers like orbital escape and reentry fall securely into the hypersonic region. Without a good knowledge of the aerodynamics of hypersonics, the quest for space travel would be greatly hampered.

Unfortunately present theoretical knowledge is inadequate for the demands of the new age hypersonic vehicles. The Navier-Stokes equations which govern the behavior of continuum fluid have defied efforts at analytical solutions. Physical experiments in this regime are difficult, expensive and sometimes even impossible. Fortunately the power of today's computers combined with the advances in applied mathematical theory allow us to obtain numerical solutions to the Navier-Stokes solutions and to uncover the physics so vital to our quest for hypersonic travel.

In order to apply numerical methods successfully in the solution of hypersonic

problems, it is necessary to gain an understanding of the strengths and weaknesses of present algorithms when applied to hypersonics. With this goal in mind, INRIA and GAMNI-SMAI are co-organizing a workshop on hypersonic flows for reentry problems. As part of this effort with SAAB Scania and FFA of Sweden, this study will investigate the applicability of a finite volume, central difference scheme coupled to the standard Jameson 4-stage time stepping algorithm. The above scheme will be applied to the solution of the Euler's equation. A semi-implicit variation of the above scheme by [Loyd] [17] will be used to solve the Navier-Stokes equations.

The application of a semi-implicit method promises substantial savings over explicit and truly implicit methods. In Navier-Stokes calculations where there is a need to pack cells densely near the body to capture the behavior of the boundary layer. Stability restrictions on an explicit scheme become severe and convergence deteriorates to a painfully slow rate. Techniques like multi-grid, and implicit residual smoothing can speed up convergence and increase stability, but the improvements become minimal as the Reynolds number increases. The implicit method ensures an instantaneous transfer of information, resulting in a very substantial increase in stability. However this technique requires the inversion of a huge block-tridiagonal matrix, a process that is both complicated and expensive. The problems pertaining to Navier-Stokes calculations stem from vastly disparate physical scales of a Navier-Stokes grid. The minute normal spacing reduces stability to such an extent that the explicit method practically comes to a standstill, while a fully implicit method designed to overcome this stability problem is expensive and results in waste when applied to the tangential directions where the stability requirement is not so restrictive. The Semi-Implicit Navier-Stokes Solver ($SINSS$) exploits the advantages of both techniques by integrating implicitly in the normal direction where the time step restriction is severe, and explicitly in the tangential direction to take advantage of the efficiency that the explicit method offers. Thus the problem of disparate scales can be overcome, resulting in a significant improvement in computational efficiency.

Instead of tackling the problem head on, we could also bypass it by making a simplification to the Navier-Stokes equations. In cases where convection is the dominant flow mechanism, viscous terms can be omitted resulting in the Euler equations. Since shear layers are absent in invicid flows, there is no need to pack cells densely near the body. Therefore the problem of disparate scales needed to resolve the boundary layer is eliminated and explicit methods are sufficient to solve the Euler equations.

Since this is part of a larger study, the body geometry and test conditions have been dictated by the requirements of the workshop. The Euler simulation is carried out at Mach 7.15, 30° angle of attack with a non-reacting gas model. The Navier-Stokes calculation is carried out under the above conditions and a Reynolds number of 5.85×10^6, with a freestream temperature of $74K$ and wall temperature of $288K$ on a laminar, non-reacting gas model.

This thesis presents semi-implicit Navier-Stokes and Euler calculations of the flow about a blunt leading-edge delta wing at the above conditions. The next chapter discusses the governing equations and boundary conditions. Chapter 3 surveys the implementation of the $SINSS$ algorithm and chapter 4 presents the grid structure. The following 2 chapters describe the solution procedure and present results for Euler and Navier-Stokes calculations. Chapter 7 compares the Euler and Navier-Stokes results and the final chapter summarizes the study and recommends future areas of research.

Chapter 2

Governing Equations and Boundary Conditions

2.1 Governing Equations

The Navier-Stokes equations embody the physics which govern the motion of viscous fluid flow. They enforce the fundamental laws of classical physics in this medium, namely the conservation of mass, momentum and energy. The three-dimensional Navier-Stokes equations can be conveniently expressed in the integral form below;

$$\frac{\partial}{\partial t} \iiint_V \mathbf{W} dV + \iint_S \vec{\mathbf{F}}(\mathbf{W}) \cdot \vec{n} dS = 0, \qquad (2.1)$$

where dV is an elemental control volume, dS its surface area and $\vec{n}$ the outward normal on the surface. The state variable $\mathbf{W}$ and flux vector $\vec{\mathbf{F}}$ are defined as follows;

$$\mathbf{W} = (\ \rho \quad \rho u \quad \rho v \quad \rho w \quad \rho E \ )^T \qquad (2.2)$$

$$\vec{\mathbf{F}} = (\mathbf{F}_I - \mathbf{F}_V)\vec{i} + (\mathbf{G}_I - \mathbf{G}_V)\vec{j} + (\mathbf{H}_I - \mathbf{H}_V)\vec{k} \qquad (2.3)$$

where ρ is the density, u, v and w are the three components of velocity and E the energy is defined as

$$E = C_v T + \frac{1}{2}(u^2 + v^2 + w^2). \qquad (2.4)$$

The subscripts I and V denote the inviscid and viscous components, given in the following equations;

$$\mathbf{F}_I = \begin{pmatrix} \rho u \\ \rho u^2 + P \\ \rho u v \\ \rho u w \\ \rho u H \end{pmatrix} \quad , \quad \mathbf{G}_I = \begin{pmatrix} \rho v \\ \rho u v \\ \rho v^2 + P \\ \rho v w \\ \rho v H \end{pmatrix} \quad , \quad \mathbf{H}_I = \begin{pmatrix} \rho w \\ \rho u w \\ \rho v w \\ \rho w^2 + P \\ \rho w H \end{pmatrix} \quad , \qquad (2.5)$$

$$\mathbf{F}_V = \begin{pmatrix} 0 \\ \tau_{xx} \\ \tau_{xy} \\ \tau_{xz} \\ u\tau_{xx} + v\tau_{xy} + \\ w\tau_{xz} - q_x \end{pmatrix} \quad , \quad \mathbf{G}_V = \begin{pmatrix} 0 \\ \tau_{xy} \\ \tau_{yy} \\ \tau_{yz} \\ u\tau_{xy} + v\tau_{yy} + \\ w\tau_{yz} - q_y \end{pmatrix} \quad , \quad \mathbf{H}_V = \begin{pmatrix} 0 \\ \tau_{xz} \\ \tau_{yz} \\ \tau_{zz} \\ u\tau_{xz} + v\tau_{yz} + \\ w\tau_{zz} - q_z \end{pmatrix} .$$

$$(2.6)$$

The total enthalpy H is defined as;

$$H = E + \frac{P}{\rho}, \qquad (2.7)$$

and P, the static pressure, is obtained from the equation of state for a perfect gas and simplifies to the expression;

$$P = \rho(\gamma - 1)\left[E - \frac{1}{2}(u^2 + v^2 + w^2)\right]. \qquad (2.8)$$

The stress tensor τ_{ij} has the form;

$$\tau_{xx} = \frac{2}{3}\mu\left(2\frac{\partial u}{\partial x} - \frac{\partial v}{\partial y} - \frac{\partial w}{\partial z}\right) \qquad \tau_{xy} = \tau_{yx} = \mu\left(\frac{\partial u}{\partial y} + \frac{\partial v}{\partial x}\right)$$

$$\tau_{yy} = \frac{2}{3}\mu\left(2\frac{\partial v}{\partial y} - \frac{\partial u}{\partial x} - \frac{\partial w}{\partial w}\right) \qquad \tau_{xz} = \tau_{zx} = \mu\left(\frac{\partial u}{\partial z} + \frac{\partial w}{\partial x}\right) \qquad (2.9)$$

$$\tau_{zz} = \frac{2}{3}\mu\left(2\frac{\partial w}{\partial z} - \frac{\partial u}{\partial x} - \frac{\partial v}{\partial y}\right) \qquad \tau_{yz} = \tau_{zy} = \mu\left(\frac{\partial v}{\partial z} + \frac{\partial w}{\partial y}\right) \quad ,$$

and the heat fluxes are;

$$q_x = -\frac{\mu}{Pr}\left(\frac{\partial H}{\partial x} - u\frac{\partial u}{\partial x} - v\frac{\partial v}{\partial x} - w\frac{\partial w}{\partial x}\right)$$

$$q_y = -\frac{\mu}{Pr}\left(\frac{\partial H}{\partial y} - u\frac{\partial u}{\partial y} - v\frac{\partial v}{\partial y} - w\frac{\partial w}{\partial y}\right) \qquad (2.10)$$

$$q_z = -\frac{\mu}{Pr}\left(\frac{\partial H}{\partial z} - u\frac{\partial u}{\partial z} - v\frac{\partial v}{\partial z} - w\frac{\partial w}{\partial z}\right) \ .$$

The Prandtl number (Pr) is defined as $Pr = \frac{\mu Cp}{k}$, where μ is the coefficient of viscosity, Cp is the specific heat capacity of the gas at constant pressure and k is the thermal conductivity of the gas.

The coefficient of viscosity is found using Sutherland's formula

$$\frac{\mu}{\mu_\infty} = \left(\frac{h}{h_\infty}\right)^{\frac{3}{2}}\frac{h_\infty + h_1}{h + h_1} \qquad (2.11)$$

which relates the local enthalpy to the freestream value h_∞ and a dimensional constant h_1 (=111421 in SI units).

2.1.1 Thin Layer Approximation

By the chain rule the derivatives with respect to x, y and z are;

$$\frac{\partial}{\partial x} = \frac{\partial \xi}{\partial x}\frac{\partial}{\partial \xi} + \frac{\partial \eta}{\partial x}\frac{\partial}{\partial \eta} + \frac{\partial \varsigma}{\partial x}\frac{\partial}{\partial \varsigma} = \xi_x\frac{\partial}{\partial \xi} + \eta_x\frac{\partial}{\partial \eta} + \varsigma_x\frac{\partial}{\partial \varsigma}$$

$$\frac{\partial}{\partial y} = \frac{\partial \xi}{\partial y}\frac{\partial}{\partial \xi} + \frac{\partial \eta}{\partial y}\frac{\partial}{\partial \eta} + \frac{\partial \varsigma}{\partial y}\frac{\partial}{\partial \varsigma} = \xi_y\frac{\partial}{\partial \xi} + \eta_y\frac{\partial}{\partial \eta} + \varsigma_y\frac{\partial}{\partial \varsigma} \qquad (2.12)$$

$$\frac{\partial}{\partial z} = \frac{\partial \xi}{\partial z}\frac{\partial}{\partial \xi} + \frac{\partial \eta}{\partial z}\frac{\partial}{\partial \eta} + \frac{\partial \varsigma}{\partial z}\frac{\partial}{\partial \varsigma} = \xi_z\frac{\partial}{\partial \xi} + \eta_z\frac{\partial}{\partial \eta} + \varsigma_z\frac{\partial}{\partial \varsigma},$$

where η is the body normal direction, and ξ and ς are streamwise and body circumferential directions respectively.

In a thin boundary layer, changes in the body normal direction usually dominate the streamwise and cross stream terms. This allows us to apply the thin layer approximation which assumes that;

$$\frac{\partial}{\partial \eta} >> \frac{\partial}{\partial \xi}, \frac{\partial}{\partial \varsigma} \qquad (2.13)$$

which enables us to eliminate all $\frac{\partial}{\partial \xi}$ and $\frac{\partial}{\partial \varsigma}$ terms, resulting in the set of simplified equations shown below;

$$\tau_{xx} \cong \frac{2}{3}\mu \left(2\eta_x \frac{\partial u}{\partial \eta} - \eta_y \frac{\partial v}{\partial \eta} - \eta_z \frac{\partial w}{\partial \eta}\right) \quad \tau_{xy} = \tau_{yx} \cong \mu \left(\eta_y \frac{\partial u}{\partial \eta} + \eta_x \frac{\partial v}{\partial \eta}\right)$$

$$\tau_{yy} \cong \frac{2}{3}\mu \left(2\eta_y \frac{\partial v}{\partial \eta} - \eta_x \frac{\partial u}{\partial \eta} - \eta_z \frac{\partial w}{\partial \eta}\right) \quad \tau_{xz} = \tau_{zx} \cong \mu \left(\eta_z \frac{\partial u}{\partial \eta} + \eta_x \frac{\partial w}{\partial \eta}\right) \qquad (2.14)$$

$$\tau_{zz} \cong \frac{2}{3}\mu \left(2\eta_z \frac{\partial w}{\partial \eta} - \eta_x \frac{\partial u}{\partial \eta} - \eta_y \frac{\partial v}{\partial \eta}\right) \quad \tau_{yz} = \tau_{zy} \cong \mu \left(\eta_z \frac{\partial v}{\partial \eta} + \eta_y \frac{\partial w}{\partial \eta}\right) \; ,$$

$$q_x \cong -\frac{\mu}{Pr}\eta_x \left(\frac{\partial H}{\partial \eta} - u\frac{\partial u}{\partial \eta} - v\frac{\partial v}{\partial \eta} - w\frac{\partial w}{\partial \eta}\right)$$

$$q_y \cong -\frac{\mu}{Pr}\eta_y \left(\frac{\partial H}{\partial \eta} - u\frac{\partial u}{\partial \eta} - v\frac{\partial v}{\partial \eta} - w\frac{\partial w}{\partial \eta}\right) \qquad (2.15)$$

$$q_z \cong -\frac{\mu}{Pr}\eta_z \left(\frac{\partial H}{\partial \eta} - u\frac{\partial u}{\partial \eta} - v\frac{\partial v}{\partial \eta} - w\frac{\partial w}{\partial \eta}\right) \; .$$

Therefore only the body normal derivatives($\frac{\partial}{\partial \eta}$) are preserved in the final form of the approximate equations. This simplification results in substantial savings in memory requirements.

2.1.2 Nondimensionalization

Freestream values and the root chord of the wing are used as reference quantities resulting in the non-dimensional variables given below;

$$
\begin{array}{lll}
x' = \frac{x}{c} & y' = \frac{y}{c} & z' = \frac{z}{c} \\[6pt]
u' = \frac{u}{a_\infty} & v' = \frac{v}{a_\infty} & w' = \frac{w}{a_\infty} \\[6pt]
\rho = \frac{\rho}{\rho_\infty} & p' = \frac{p}{\rho_\infty a_\infty^2} & t' = \frac{t}{c/a_\infty} \\[6pt]
\mu' = \frac{\mu}{\mu_\infty}\frac{M_\infty}{Re_\infty} & E' = \frac{E}{a_\infty^2} & H' = \frac{H}{a_\infty^2}.
\end{array}
\qquad (2.16)
$$

Therefore the non-dimensionalized freestream state vector can be expressed as;

$$\vec{\mathbf{W}}' = \begin{pmatrix} 1 \\ M_\infty cos\alpha \\ 0 \\ M_\infty sin\alpha \\ \frac{1}{\gamma(\gamma-1)} + \frac{M_\infty^2}{2} \end{pmatrix} \qquad (2.17)$$

For convenience the primes will henceforth be dropped and only nondimensional variables will be used.

2.2 Physical Boundary Conditions

A problem is only well posed if the correct number of boundary conditions is specified. Since this is a hypersonic calculation, the flow ahead of the wing should be uniform freestream. On the solid wall, there is no flux through the surface, and in the viscous calculation, physics dictate a no-slip wall boundary condition. The implementation of these boundary conditions will be treated in the next chapter.

Chapter 3

Solution Algorithm

To render the Navier-Stokes equations solvable via numerical techniques, they have to be discretized. Since these are partial differential equations in space and time, both spatial and temporal discretization are necessary. Although these two discretization processes are strongly interdependent, it is common to formulate them in two stages; spatial and temporal. The spatial discretization employed is a cell-centered finite volume technique, while the temporal discretization is based on the Jameson 4-stage numerical integration scheme, modified by the semi-implicit formulation.

The spatial discretization described above permits odd/even decoupling in adjacent cells. In order to damp out these non-physical disturbances, artificial viscosity has to be added. Furthermore artificial viscosity is needed to capture shock waves and damp out pressure overshoots in the regions of strong shocks and expansion.

3.1   Spatial Discretization

The discretization process attempts to find an approximate representation to the real governing equations. By obtaining a correct solution to these approximate equations, we hope to get an approximate solution to the correct equations. Needless to say, the accuracy of the approximate equations is vital to a good solution. For more information on the accuracy of the discretization process employed, the reader is advised to refer to [Loyd][17].

Spatial discretization is applied to the surface integral in equation (2.1) which calculates the net fluxes of mass, momentum and energy leaving a control volume dV. In the physical domain, the control volumes are hexahedrals and therefore the surface flux integrals can be represented as;

$$\iint_{\partial V} \vec{F}(\mathbf{W}) \cdot \hat{n} dS = \sum_{f=1}^{6} \vec{F}(\mathbf{W})_f \cdot \vec{S}_f = \sum_{f=1}^{6} (FS_x + GS_y + HS_z)_f \qquad (3.1)$$

where the face numbering and computational grid orientation are given in the figures 3.1 and 3.2 respectively. Faces 5 and 6 are assumed to be parallel to the solid surface.

The vector $\vec{S}_f$ is the surface normal whose components are the projection of the surface area onto the three Cartesian planes. $\vec{S}_f$ is taken to be positive pointing out of the control volume. This is calculated by taking half the vector product of the cell face diagonals, which uses the assumption that the 4 points defining the face are coplaner. The above representation is exact in the case of hexahedrals. To make the discretized version solvable, a few simplifying assumptions have to be made. Firstly the fluxes are assumed to be constant over each face. Secondly the fluxes at a face are calculated from the state vector in the center of the two adjacent cells. For example, the inviscid fluxes are given by;

$$
\begin{aligned}
F_{I_1} &= \tfrac{1}{2}(F_{I_{i+1,j,k}} + F_{I_{i,j,k}}) & F_{I_2} &= \tfrac{1}{2}(F_{I_{i,j,k}} + F_{I_{i-1,j,k}}) \\
F_{I_3} &= \tfrac{1}{2}(F_{I_{i,j+1,k}} + F_{I_{i,j,k}}) & F_{I_4} &= \tfrac{1}{2}(F_{I_{i,j,k}} + F_{I_{i,j-1,k}}) \\
F_{I_5} &= \tfrac{1}{2}(F_{I_{i,j,k+1}} + F_{I_{i,j,k}}) & F_{I_6} &= \tfrac{1}{2}(F_{I_{i,j,k}} + F_{I_{i,j,k-1}})
\end{aligned}
\qquad (3.2)
$$

And the viscous terms involving $\frac{\partial}{\partial \eta}$ need only be evaluated for faces 5 and 6 as

$$\frac{\partial ()}{\partial \eta}|_5 = \frac{()_{j+1} - ()_j}{\Delta \eta} \qquad \frac{\partial ()}{\partial \eta}|_6 = \frac{()_j - ()_{j-1}}{\Delta \eta}. \qquad (3.3)$$

To simplify the computations, $\Delta \eta$ can arbitrarily be set to 1.
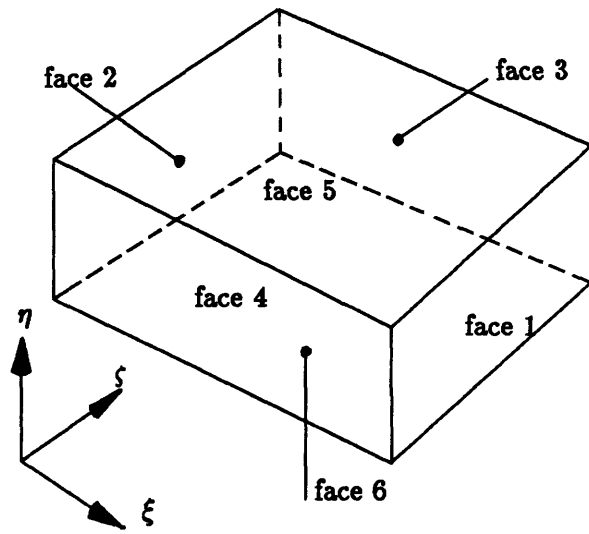
Figure 3.1: Cell nomenclature
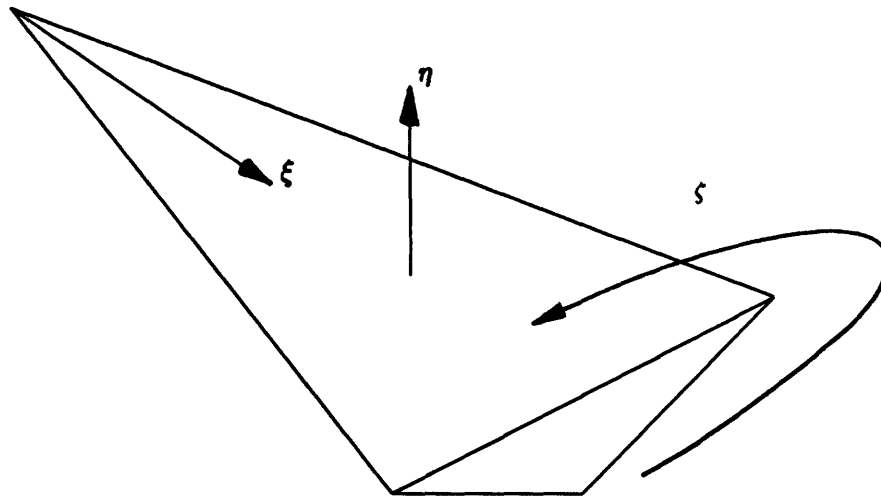
Figure 3.2: Orientation of computational coordinates

The semi-discrete form of equation 2.1 then becomes;

$$\frac{d}{dt} V_{i,j,k} \mathbf{W}_{i,j,k} = -\mathbf{R}_{i,j,k}$$

$$\mathbf{R}_{i,j,k} = \sum_{f=1}^{6} (\mathbf{F} S_x + \mathbf{G} S_y + \mathbf{H} S_z)_{f_{i,j,k}}$$

(3.4)

where $V_{i,j,k}$ is the volume of the cell.

3.2 Artificial Viscosity

Damping is present as a result of the viscous terms in the Navier-Stokes equations. However these terms become insignificant far away from the body . In the absence of dissipation, the cell centered discretization discussed in the last section permits decoupling of odd and even modes. To damp out noise that result from this decoupling, a slight amount of background smoothing is necessary.

In regions of shocks, the physical viscous terms are significant, but the scale of the physical shock is so small (order of the mean free path of the gas molecules) that to resolve the shock without the addition of even more artificial viscosity would require a grid spacing of this size. Clearly such a situation is unacceptable, and additional damping is required to capture the shock in a reasonably sized grid.

The dissipation model used is a blend of 2nd and 4th differences [Jameson] [10]. The 3-D operator is the sum of one-dimensional differences in each of the 3 directions;

$$\mathbf{D}(\mathbf{W}) = \mathbf{D}_\xi(\mathbf{W}) + \mathbf{D}_\eta(\mathbf{W}) + \mathbf{D}_\zeta(\mathbf{W})$$

(3.5)

where the one-dimensional difference operators in the streamwise, normal and circumferential directions are;

28

$$\mathbf{D}_\xi(\mathbf{W}) = \mathbf{d}_{i+\frac{1}{2},j,k} - \mathbf{d}_{i-\frac{1}{2},j,k}$$
$$\mathbf{D}_\eta(\mathbf{W}) = \mathbf{d}_{i,j+\frac{1}{2},k} - \mathbf{d}_{i,j-\frac{1}{2},k} \tag{3.6}$$
$$\mathbf{D}_\zeta(\mathbf{W}) = \mathbf{d}_{i,j,k+\frac{1}{2}} - \mathbf{d}_{i,j,k-\frac{1}{2}},$$

the difference operator $\mathbf{d}_{i+\frac{1}{2},j,k}, \mathbf{d}_{i-\frac{1}{2},j,k}$, etc. are constructed from 2nd and 4th differences in the following manner;

$$\mathbf{d}_{i+\frac{1}{2}} = (\tfrac{V}{\Delta t})_{i+\frac{1}{2}}[\quad \epsilon^{(2)}_{i+\frac{1}{2}}(\mathbf{W}_{i+1} - \mathbf{W}_i) -$$
$$\epsilon^{(4)}_{i+\frac{1}{2}}(\mathbf{W}_{i+2} - 3\mathbf{W}_{i+1} + 3\mathbf{W}_i - \mathbf{W}_{i-1})]$$
$$\mathbf{d}_{i-\frac{1}{2}} = (\tfrac{V}{\Delta t})_{i-\frac{1}{2}}[\quad \epsilon^{(2)}_{i-\frac{1}{2}}(\mathbf{W}_i - \mathbf{W}_{i-1}) - \tag{3.7}$$
$$\epsilon^{(4)}_{i-\frac{1}{2}}(\mathbf{W}_{i+1} - 3\mathbf{W}_i + 3\mathbf{W}_{i-1} - \mathbf{W}_{i-2})].$$

For the sake of clarity, all j and k indices have been omitted. The differences in the other 2 directions are similar.

The coefficients $\epsilon^{(2)}$ and $\epsilon^{(4)}$ are defined as;

$$\epsilon^{(2)}_{i+\frac{1}{2}} = \tfrac{\kappa^{(2)}}{2}(\nu_{\xi_{i+1}} + \nu_{\xi_i})$$
$$\epsilon^{(4)}_{i+\frac{1}{2}} = max(0, \kappa^{(4)} - \epsilon^{(2)}_{i+\frac{1}{2}}) \tag{3.8}$$

where ν a pressure weighted scaling factor;

$$\nu_{\xi_i} = \frac{|P_{i+1} - 2P_i + P_{i-1}|}{P_{i+1} + 2P_i + P_{i-1}} \tag{3.9}$$

that is designed to switch on in regions of high pressure gradient.

The final form of the semi-discrete equation is;

$$\tfrac{d}{dt}V_{i,j,k}\mathbf{W}_{i,j,k} = -\mathbf{R}_{i,j,k} + \mathbf{D}_{i,j,k} \tag{3.10}$$

where $\mathbf{R}_{i,j,k}$ is given in equation 3.4, and $\mathbf{D}_{i,j,k}$ is the dissipation vector.

The formulation of the dissipation operator in boundary regions is based on a scheme by [Eriksson and Rizzi][6]. Values of the state vector in the ghost cells are obtained by linear extrapolations from the interior;

$$
\begin{aligned}
\mathbf{W}_0 &= 2\mathbf{W}_1 - \mathbf{W}_2 \\
\mathbf{W}_{-1} &= 3\mathbf{W}_1 - 2\mathbf{W}_2 .
\end{aligned}
\tag{3.11}
$$

The damping operator in the boundary cells can be calculated in the same manner as for interior cells. However this technique tends to introduce too much dissipation in the boundary layer. Therefore in the Navier-Stokes calculation, the 2nd and 4th order dissipation in the normal direction is set to zero in the first 2 cells adjacent to the wall [Loyd][17].

3.3   Implicit Formulation

The temporal integration scheme is based on the 4-stage algorithm by [Jameson et. al.] [9], and proceeds in the following manner;

$$
\begin{aligned}
\mathbf{W}^0 &= \mathbf{W}^n \\[4pt]
\mathbf{W}^1 &= \mathbf{W}^0 - \alpha_1 \tfrac{\Delta t}{V} \left(\mathbf{R}^0 - \mathbf{D}^0 \right) \\[4pt]
\mathbf{W}^2 &= \mathbf{W}^0 - \alpha_2 \tfrac{\Delta t}{V} \left(\mathbf{R}^1 - \mathbf{D}^0 \right) \\[4pt]
\mathbf{W}^3 &= \mathbf{W}^0 - \alpha_3 \tfrac{\Delta t}{V} \left(\mathbf{R}^2 - \mathbf{D}^0 \right) \\[4pt]
\mathbf{W}^4 &= \mathbf{W}^0 - \alpha_4 \tfrac{\Delta t}{V} \left(\mathbf{R}^3 - \mathbf{D}^0 \right) \\[4pt]
\mathbf{W}^{n+1} &= \mathbf{W}^4 ,
\end{aligned}
\tag{3.12}
$$

where

$$\mathbf{R}^m = \sum_{f=1}^{6} (\mathbf{F}^m S_x + \mathbf{G}^m S_y + \mathbf{H}^m S_z)_f . \tag{3.13}$$

The superscripts m indicate the time level and subscripts f denote the cell faces while $\mathbf{D}^0$ is the dissipation vector calculated at the start of the numerical integration and frozen throughout all four stages. The time step coefficients are;

$$\alpha_1 = \tfrac{1}{4} \quad \alpha_2 = \tfrac{1}{3} \quad \alpha_3 = \tfrac{1}{2} \quad \alpha_4 = 1. \tag{3.14}$$

In explicit mode, this is precisely what *SINSS* does. But the semi-implicit formulation requires some modifications. The purpose of the semi-implicit scheme is to eliminate the stability restrictions that small body-normal spacing imposes on the algorithm. To realize this, the fluxes in faces 5 and 6 are treated implicitly. Applying this to the first stage of the 4 stage scheme results in;

$$\mathbf{W}^1 - \mathbf{W}^0 = -\alpha_1 \frac{\Delta t}{V} \left[\mathbf{Res}_1^0 + \mathbf{Res}_2^0 + \mathbf{Res}_3^0 + \mathbf{Res}_4^0 + \mathbf{Res}_5^1 + \mathbf{Res}_6^1 - \mathbf{D}^0) \right] \tag{3.15}$$

where

$$\mathbf{Res}_f^m = (\mathbf{F}^m S_x + \mathbf{G}^m S_y + \mathbf{H}^m S_z)_f \tag{3.16}$$

The fluxes through faces 5 and 6 have to be calculated from the unknown state vector at the next time level. To do this we first have to carry out the Newton linearization of the fluxes $\mathbf{F}, \mathbf{G}$ and $\mathbf{H}$;

$$\mathbf{F}^1 = \mathbf{F}^0 + \frac{\partial \mathbf{F}^0}{\partial t} \Delta t + O(\Delta t^2) = \mathbf{F}^0 + [A]^0 \Delta \mathbf{W}^1 + O(\Delta t^2)$$

$$\mathbf{G}^1 = \mathbf{G}^0 + \frac{\partial \mathbf{G}^0}{\partial t} \Delta t + O(\Delta t^2) = \mathbf{G}^0 + [B]^0 \Delta \mathbf{W}^1 + O(\Delta t^2) \tag{3.17}$$

$$\mathbf{H}^1 = \mathbf{H}^0 + \frac{\partial \mathbf{H}^0}{\partial t} \Delta t + O(\Delta t^2) = \mathbf{H}^0 + [C]^0 \Delta \mathbf{W}^1 + O(\Delta t^2)$$

where $[A], [B]$ and $[C]$ are 5×5 Jacobian matrices;

$$[A] = [\tfrac{\partial \mathbf{F}}{\partial \mathbf{W}}], \quad [B] = [\tfrac{\partial \mathbf{G}}{\partial \mathbf{W}}], \quad [C] = [\tfrac{\partial \mathbf{H}}{\partial \mathbf{W}}], \tag{3.18}$$

and

$$\Delta \mathbf{W}^1 \equiv \mathbf{W}^1 - \mathbf{W}^0. \tag{3.19}$$

31

The equations contain only one unknown $\Delta \mathbf{W}$, the 5-component vector for the change in the state vector in each cell. All other quantities can be calculated from the known state vector $\mathbf{W}^0$. Combining equations 3.15 and 3.17 and grouping the Jacobian terms on the left hand side result in the final form of the semi-implicit equation;

$$\left[[I] + \alpha_1 \frac{\Delta t}{V} \left([A]_5 S_{x_5} + [A]_6 S_{x_6} + [B]_5 S_{y_5} + [B]_6 S_{y_6} + [C]_5 S_{x_5} + [C]_6 S_{x_6} \right) \right] \Delta \mathbf{W} =$$

$$-\alpha_1 \frac{\Delta t}{V} \left[\sum_{j=1}^{6} (\mathbf{F} S_x + \mathbf{F} S_y + \mathbf{H} S_z)_j - \mathbf{D} \right]^0 . (3.20)$$

For convenience, the matrix in brackets on the left of $\Delta \mathbf{W}$ will henceforth be abbreviated as $[LHS]$. Using the algorithm based on [Jameson et al.][9], the 4-stage time integration of the semi-implicit equations takes on the form;

$$\mathbf{W}^0 = \mathbf{W}^n$$

$$[LHS]^0 \Delta \mathbf{W}^1 = -\alpha_1 \tfrac{\Delta t}{V} (\mathbf{R}^0 - \mathbf{D}^0)$$

$$[LHS]^1 \Delta \mathbf{W}^2 = -\alpha_2 \tfrac{\Delta t}{V} (\mathbf{R}^1 - \mathbf{D}^0) - \Delta \mathbf{W}^1$$

$$[LHS]^2 \Delta \mathbf{W}^3 = -\alpha_3 \tfrac{\Delta t}{V} (\mathbf{R}^2 - \mathbf{D}^0) - (\Delta \mathbf{W}^2 + \Delta \mathbf{W}^1)$$

$$[LHS]^3 \Delta \mathbf{W}^4 = -\alpha_4 \tfrac{\Delta t}{V} (\mathbf{R}^3 - \mathbf{D}^0) - (\Delta \mathbf{W}^3 + \Delta \mathbf{W}^2 + \Delta \mathbf{W}^1)$$

$$\mathbf{W}^{n+1} = \mathbf{W}^3 + \Delta \mathbf{W}^4$$

$$(3.21)$$

where $\mathbf{R}^m$ is the residual at time level m whose form is given in equation 3.13 and $\Delta \mathbf{W}^m = \mathbf{W}^m - \mathbf{W}^{m-1}$.

In the explicit Euler calculation, the time step is given by [Loyd][17];

$$\Delta t_{i,j,k} \leq \left[\frac{CFL_{max} Vol}{|uS_x|_{max} + |vS_y|_{max} + |wS_z|_{max} + a|S_{max}|} \right]_{i,j,k} \quad (3.22)$$

where S_x, S_y and S_z are the x, y and z component of cell faces, and S is the surface normal vector whose magnitude is the area of the face. Through stability analysis, it can be shown that CFL_{max} is $2\sqrt{2}$. When executing the Navier-Stokes semi-implicit integration, the stability limit in the body-normal direction is eliminated and the time step limitation can be relaxed to [Loyd][17];

$$\Delta t_{i,j,k} \leq \left[\frac{CFL_{max}Vol}{|uS_x|_{max_{1,2,3,4}} + |vS_y|_{max_{1,2,3,4}} + |wS_z|_{max_{1,2,3,4}} + a|S_{max_{1,2,3,4}}|} \right]_{i,j,k}$$

(3.23)

where 1 and 2, and 3 and 4 indicate faces in the streamwise and circumferential directions. The values thus calculated are the local time steps and vary from one cell to another. In steady state calculations where the final solution is not time dependent, local time steps increase the rate of convergence. Whenever possible, local time steps are used in the present calculations. However in semi-implicit computations, this was found to be unstable and ring-wise constant time step were used, and the time step was a function of i and j indices only.

3.4 Residual Smoothing

The restriction on the CFL number can be relaxed by smoothing the residuals before updating the state vector [Jameson & Baker][12]. This in effect increases the range of the solution stencil by taking information in a cell and spreading it around to its neighbors. The result is an increase in stability. The smoothing is applied implicitly in the following manner;

$$\left(1 - \epsilon_{RS}\delta_{xx}\right)\mathbf{R}^1 = \mathbf{R}$$

$$\left(1 - \epsilon_{RS}\delta_{yy}\right)\mathbf{R}^2 = \mathbf{R}^1 \tag{3.24}$$

$$\left(1 - \epsilon_{RS}\delta_{zz}\right)\mathbf{R}^3 = \mathbf{R}^2$$

where $\mathbf{R}$ the residual is the sum of the flux and dissipation residuals and δ is the second difference operator. Residual smoothing is applied at the *2nd* and *4th* stages of the inviscid calculation and only at the *4th* stage in the viscous case. In all calculations the value the residual smoothing coefficient ϵ_{RS} was set to 1.0.

3.5 Implicit Smoothing

The matrix $[LHS]$ loses diagonal dominance and becomes ill conditioned when the aspect ratio of the cells is high. For example, in a Cartesian cell with a very high aspect ratio such that $\Delta x = \Delta z$ and $\Delta y = \Lambda\Delta x = \Lambda\Delta z$ where $\Lambda << 1$, the $[LHS]$ matrix becomes

$$
\begin{aligned}
[LHS] \quad &= [I] + \alpha\tfrac{\Delta t}{V}\left([A]_5 S_{x_5} + [A]_6 S_{x_6} + [B]_5 S_{y_5} + [B]_6 S_{y_6} + [C]_5 S_{z_5} + [C]_6 S_{z_6}\right)\\[4pt]
&= [I] + \alpha\tfrac{\Delta t}{\Lambda\Delta x^3}\left([A]_5\Lambda\Delta x^2 + [A]_6\Lambda\Delta x^2 + [B]_5\Delta x^2 + [B]_6\Delta x^2 + [C]_5\Lambda\Delta x^2 + [C]_6\Lambda\Delta x^2\right)\\[4pt]
&\cong [I] + \alpha\tfrac{\Delta t}{\Lambda\Delta x}\left([B]_5 + [B]_6\right)\\[4pt]
&\cong [I] + \alpha\tfrac{\Delta t}{\Lambda\Delta x}\left([B]_{j+1} + [B]_{j-1}\right).
\end{aligned}
$$

$$\tag{3.25}$$

This results in the Jacobians contributing mainly to the off-diagonal terms. The smaller the Λ is, the more acute the problem. The second difference operator below can be applied to $[LHS]$ to regain diagonal dominance;

$$- \epsilon_{SI}\left[\mathbf{W}_{j+1} - 2\mathbf{W}_j + \mathbf{W}_{j-1}\right] \tag{3.26}$$

34

Since the terms are added to the left hand side of the equation, implicit smoothing does not affect the final solution. However it may retard the rate of convergence [Loyd][17]. For this computation, the value of ϵ_{SI} was set to 0.005.

3.6 Implementation of the Boundary Conditions

For this numerical simulation, boundary conditions are required on the wing surface, at the inflow, outflow, farfield and symmetry boundaries. These boundary conditions are implemented by assigning appropriate values to ghost cells placed just outside the boundary.

3.6.1 Farfield Boundaries

Reimann invariants are employed at the farfield boundaries to determine the value of the state vector in the ghost cells. This technique is based on the theory of characteristic lines and the transfer of fluid mechanical information in one dimensional flow [Jameson & Baker][12]. It enables the propagation of information through boundaries, resulting in minimal reflection of waves and a higher rate of convergence. The incoming and outgoing Reimann invariants are;

$$
\begin{aligned}
R_- &= \vec{u}_\infty \cdot \hat{n} - 2\frac{a_\infty}{\gamma-1} &= u_n - 2\frac{a}{\gamma-1} \\
R_+ &= \vec{u}_{ex} \cdot \hat{n} + 2\frac{a_{ex}}{\gamma-1} &= u_n - 2\frac{a}{\gamma-1}
\end{aligned}
\tag{3.27}
$$

where the subscript ∞ denotes freestream conditions, ex represents values extrapolated from the first cell within the boundary, and $\hat{n}$ is the unit normal pointing out of the domain. The normal velocity and the speed of sound at the boundary cells can be obtained from the Reimann invariants;

$$
\begin{aligned}
u_n &= \tfrac{1}{2}(R_+ + R_-) \\
a &= \tfrac{\gamma-1}{4}(R_+ - R_-)
\end{aligned}
\tag{3.28}
$$

35

The resultant velocity at the outflow is;

$$\vec{u} = \vec{u}_{ex} + (u_n - \vec{u}_{ex} \cdot \vec{n})\vec{n} \qquad (3.29)$$

and for the inflow;

$$\vec{u} = \vec{u}_\infty + (u_n - \vec{u}_\infty \cdot \vec{n})\vec{n}. \qquad (3.30)$$

The entropy at the outflow boundary is extrapolated from the interior,

$$s = s_{ex} = \frac{p_{ex}}{\rho_{ex}^\gamma} \qquad (3.31)$$

and at the inflow it is specified as,

$$s = s_\infty = \frac{1}{\gamma}. \qquad (3.32)$$

The outflow boundary conditions at the trailing edge are treated in 2 distinct ways depending on the nature of the computation. In the inviscid calculation, Reimann invariants are used, but for the viscous calculation, it turns out better to extrapolate the interior values to the boundary.

3.6.2   Solid Wall

Again the inviscid and viscous calculations demand different treatments. In the inviscid case, no convective fluxes pass through the solid wall, therefore only the pressure term in the momentum fluxes is preserved. In initial calculations pressure was set equal to the value in the first cell. More recent calculations make use of the normal momentum equations to determine the pressure in the ghost cell, but this did not affect the results.

The above conditions apply to the viscous calculation too. The pressure approximation is even better since the body-normal pressure gradient within a boundary

layer is very small. In addition to the pressure term, viscous components contribute to the flux summation. The no-slip and isothermal wall conditions are enforced by assigning appropriate values of velocity and energy to the ghost cells. The value of density was extrapolated to the ghost cell,

$$\rho_0 = 2\rho_1 - \rho_2 \tag{3.33}$$

and the velocities were determined as,

$$\vec{u}_0 = -\vec{u}_1 \tag{3.34}$$

and the energy term was set in the following manner;

$$\rho_0 E_0 = 2\rho_{wall} E_{wall} - \rho_1 E_1. \tag{3.35}$$

E_{wall} is determined from the given value of T_{wall} and ρ_{wall} comes form linear extrapolation of the first two interior values.

3.6.3   Symmetry Plane

Since the simulations are carried out for zero yaw angle, a symmetry plane exists along the root chord of the wing. Boundary conditions in the symmetry plane are straightforward since the flows on either side of the plane are mirror images of each other. This condition is obtained by setting all variables in the ghost cell to the value of the corresponding interior cell with the exception of the velocity normal to the symmetry plane, which is set to the negative of the value in the interior cell. In this calculation, only the y-component of the velocity undergoes a sign reversal when assigned to the ghost cell.

37

Chapter 4

Grid

This chapter presents the geometry of the wing and describes the necessary conditions for an optimum grid.
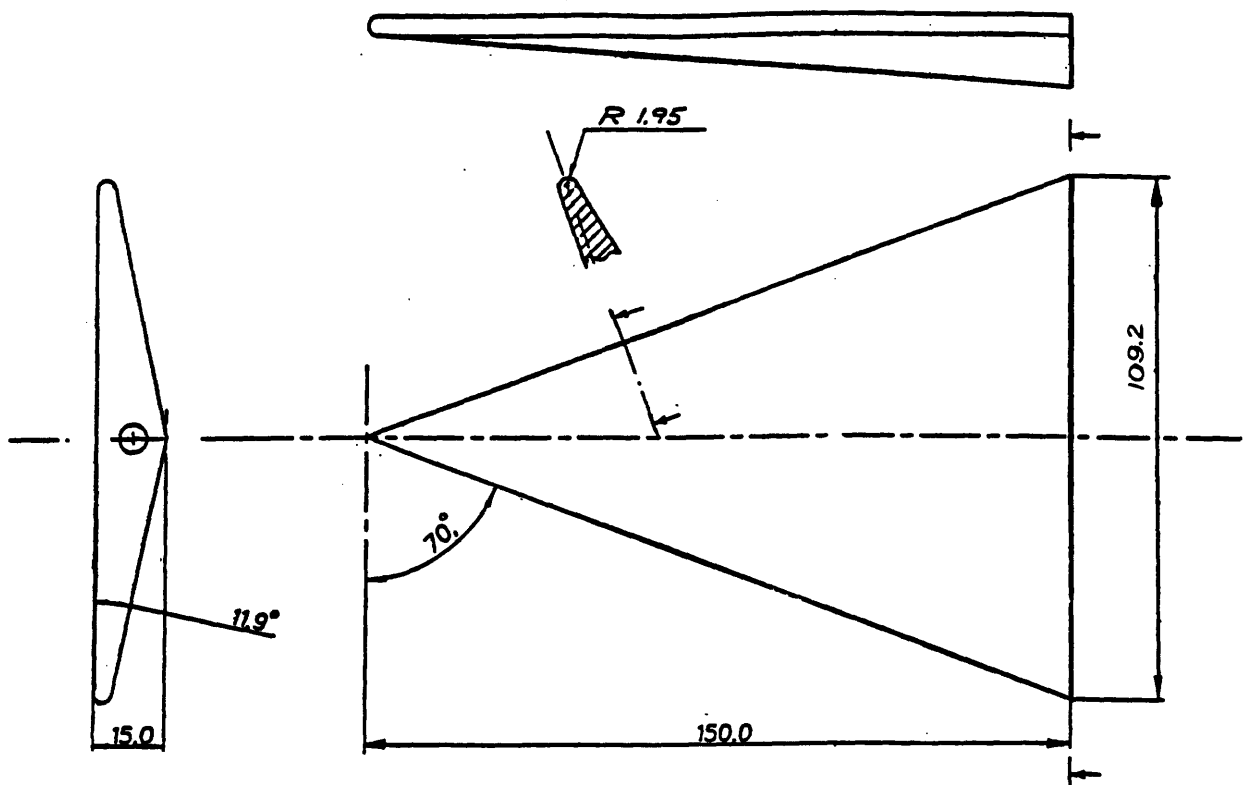
4.1 Wing Geometry

Figure 4.1: Geometry of the wing

The model is a blunt leading edge delta wing with a leading edge sweep of 70.0°. It is 150.0cm long, 15.0cm thick at the center of the trailing edge, and has a leading edge radius of 1.95cm. This leading edge radius is constant throughout, resulting in a non-conical wing. A detailed diagram of the wing geometry is shown in Figure 4.1. A sting attached to the base is used to hold the model during wind tunnel tests.

4.2   Grid Requirements

The solution of the Navier-Stokes equations is an extremely expensive endeavor. The cost stems from the need to cluster cells near the body in order to capture the important viscous phenomena. This clustering has two consequences. Firstly we need more cells to discretize a given region. Secondly (and of greater consequence) the small normal spacing increases the stiffness of the system to the extent that expensive implicit schemes are necessary. Needless to say, a grid that gives the necessary resolution with the minimum number of cells is a highly desirable goal. Therefore appropriate attention is being given to the construction of a good grid.

The obvious way to decrease the number of grid points is to reduce the range of the grid. The geometry of the wing at the base makes it impossible to construct a computational OH-grid without making modifications to the trailing edge region. Using an interfaced grid or employing an unstructured flow solver will overcome this difficulty. Since the purpose of this calculation is to investigate the suitablility of the present code in modelling the problem, the above solutions are not applicable. Modifying the base geometry to fit a mesh would probably result in an error that is of the same order of magnitude as neglecting the wake region. Therefore for the sake of economy, the wake region has been omitted in this calculation. However the flat base trailing edge does contribute to the total drag. Assuming that the region aft of the base is vacuum would yield the upper bound of the base drag contribution whereas setting the base pressure to freestream would result in the lower limit of the

drag. The difference between the 2 gives the maximum possible error that can result from excluding the base region from the calculation. This analysis indicates that the maximum contribution of base drag to the total drag coefficient is of the order of 10^{-3}. Since the drag coefficient should be of the order of 10^{-1}, the contribution of the base is at most a meager 1% and can safely be neglected. In this calculation the ommision of the wake area results in a drag calculation that assumes vacuum in the base region and yields the upper bound of the drag coefficient. Another region that need not be discretized is the domain upstream of the wing. Unlike calculations for blunt-nose bodies where a bow shock is expected ahead of the body, the apex of the present wing is sharp. Therefore an attached shock is expected and the wing produces no upstream influence making it unnecessary to extend the calculation ahead of the wing. Since calculations are carried out for zero yaw angle, a cut can be made along the symmetry plane and the solution obtained for only half of the wing.

As a result of the above simplifications, the grid spans only the length of the wing, and covers half the surface from the symmetry plane to the leading edge. The 3D grid is formed by stacking O-grid slices in successive streamwise stations, resulting in an OH-grid topology with the orientation shown in figure 3.2.

To obtain the optimal resolution for a given number of grid points, it is necessary to group points into regions where the state vector is changing most rapidly. Since this is a viscous calculation, we know apriori that the boundary layer is one such region. Within the boundary layer, changes in the body normal direction dominate, therefore fine spacing must be maintained in this direction. Furthermore the thin layer approximation assumes that the η direction is normal to the body surface. Therefore it is important to impose cell face orthogonality in the boundary layer in order to maintain solution accuracy.

Since this is not a conical wing, the cross stream profile of the wing changes
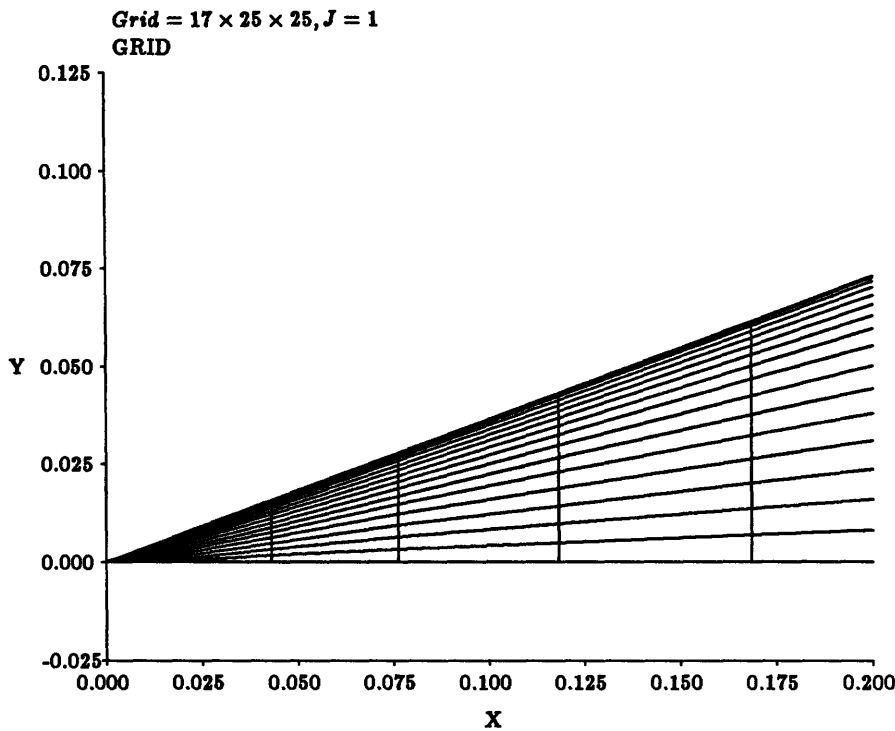
Figure 4.2: Top surface of the wing, showing the distribution of streamwise stations

at each streamwise station. These changes are most pronounced near the apex. Furthermore the apex is a region where rapid changes in the flowfield occur for it is here that the freestream first impinges upon the wing. To capture these changes it is necessary to cluster points near the apex. A sinusoidal distribution of streamwise stations was selected to give the necessary packing. The diagram of the wing surface in figure 4.2 exhibits this distribution.

Other than the above general inferences, it is impossible to make any more decisions concerning the optimal grid. To determine other regions of rapid changes, it was necessary to run a trail calculation. Results showed the approximate shock position and helped determine the position and size of the farfield boundary. The experiment showed that changes in the circumferential direction were more pronounced on the leeward side and near the leading edge of the wing. Therefore $\frac{2}{3}$ of the circumferential points was placed on the leeward surface, with some clustering around the leading edge.

The 2 dimensional crossflow planes were generated by using an elliptic grid generator which solves the set of second order elliptic partial differential equations below:

$$\eta_{yy} + \eta_{zz} = 0$$

$$\varsigma_{yy} + \varsigma_{zz} = 0.$$

(4.1)

However with the straightforward function shown above, the grid points will be evenly spaced and the desired clustering of cells cannot be attained. To remedy the situation, a 'conductivity' term κ is introduced in the following manner:

$$(\kappa\eta_y)_y + (\kappa\eta_z)_z = 0$$

$$(\kappa\varsigma_y)_y + (\kappa\varsigma_z)_z = 0.$$

(4.2)

Grid points tend to cluster around regions of small κ. Therefore clustering can be controlled by manipulating the form of κ. The form of κ given in equation 4.3 gives a nice clustering in the body normal direction

$$\kappa = 1. + \epsilon_j J.$$

(4.3)

The values of ϵ_j were set to 0.025 and 0.1 for the Euler and Navier-Stokes grid respectively.

As a consequence of the clustering in the body-normal direction, the points on the symmetry boundary must be allowed to float, so that the constant J lines can hit this boundary with an appropriate slope. This slope is a weighted average of the values on the wing body and the outer boundary. A close up of the grid showing the grid structure near the wall is shown in Figure 4.3.

Since there are twice as many cells on the top surface of the wing as there are below, packing is tighter on the upper surface. This results in discontinuous circumferential spacing at the leading edge as shown in Figure 4.4.
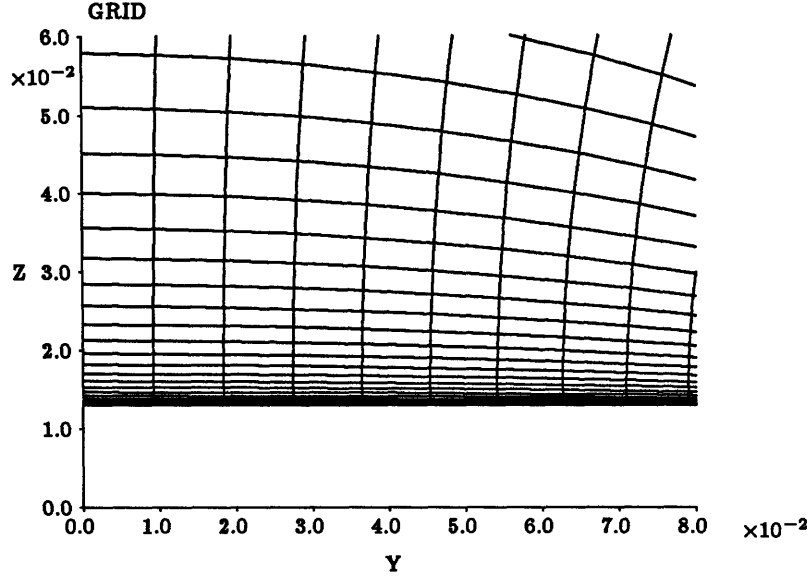
42

Figure 4.3: Grid structure near the wall

To remedy the situation, a K dependence was introduced into the κ function in the following manner:

$$\kappa = 1. + \epsilon_j J \left[\frac{K_{add}}{K_{add}+K} \right] \qquad K \leq K_{tip}$$

$$\kappa = \kappa|_{K_{tip}} \qquad K > K_{tip}$$

(4.4)

Where K_{add} is a constant. By manipulating K_{add}, the grid with the desired circumferential distribution can be obtained. The final grid which exhibits an acceptable structure in at the leading edge is shown in figure 4.5. This was obtained by setting K_{add} to 26 for a grid of 97 circumferential points. However the constant K_{add} has to be varied from one streamwise station to another making it necessary to include a streamwise dependence in the κ expression.

$$\kappa = 1. + \epsilon_j J \left[\frac{K_{add}+\epsilon_i(IMAX-I)}{K_{add}+\epsilon_i(IMAX-I)+K} \right] \qquad K \leq K_{tip}$$

$$\kappa = \kappa|_{K_{tip}} \qquad K > K_{tip}$$

(4.5)

The additional term effectively changes the value of K_{add} as we move from one

43

streamwise station to another. ϵ_i was set to 1.0 and 0.6 for the Euler and Navier-Stokes grids respectively. The final Euler grid consists of $33 \times 49 \times 97$ nodes in the streamwise, body-normal and circumferential directions respectively, and the Navier-Stokes grid has $33 \times 97 \times 97$ nodes. Fine grids used for Euler and Navier-Stokes calculations are shown in figures 4.6 and 4.7.
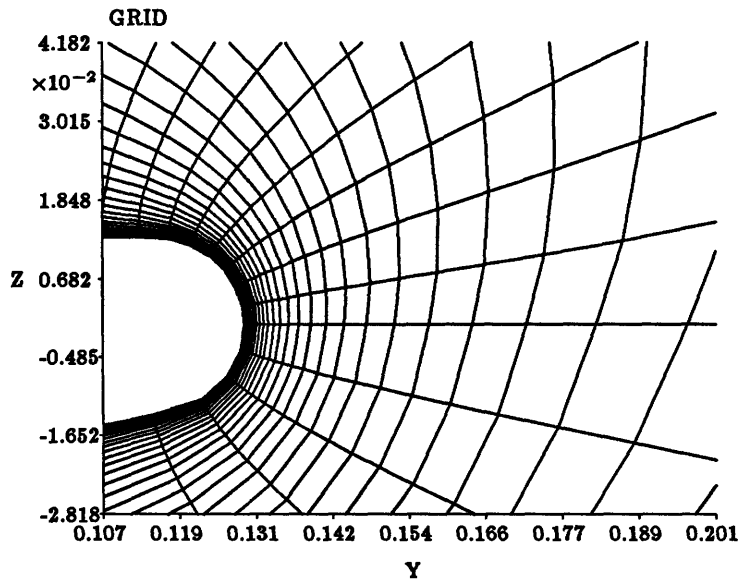
Figure 4.4: Grid structure at the leading edge, without circumferential correction
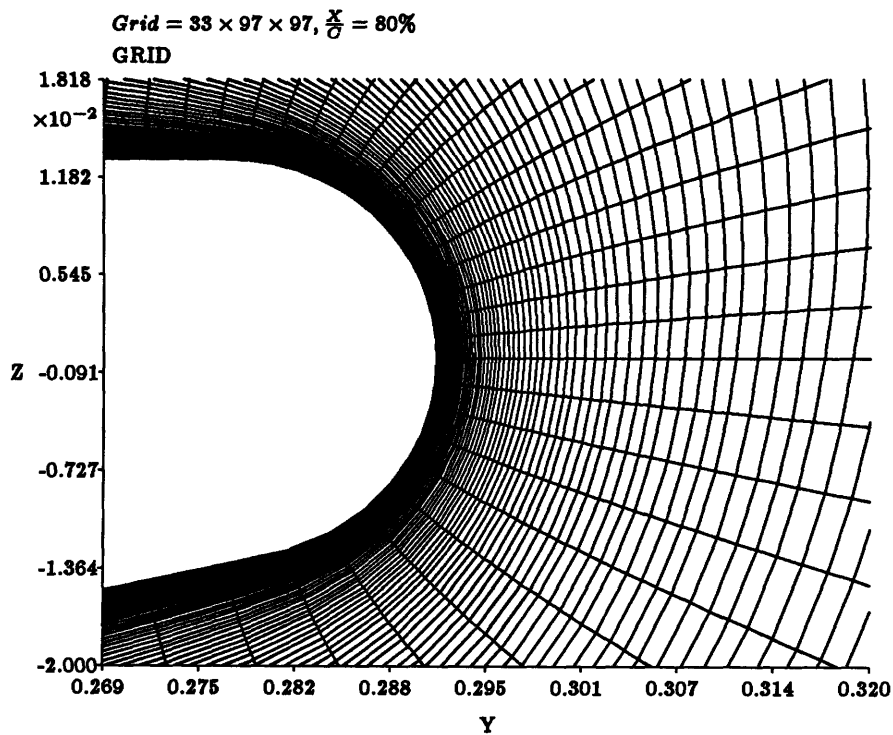
Grid = 33 × 97 × 97, $\frac{X}{C}$ = 80%

Figure 4.5: Final Navier-Stokes grid with correct circumferential spacing

$M = 7.15, Re = 0.585E + 07, \alpha = 30.00°, Grid = 33 \times 97 \times 97, X/C = 0.50$
GRID
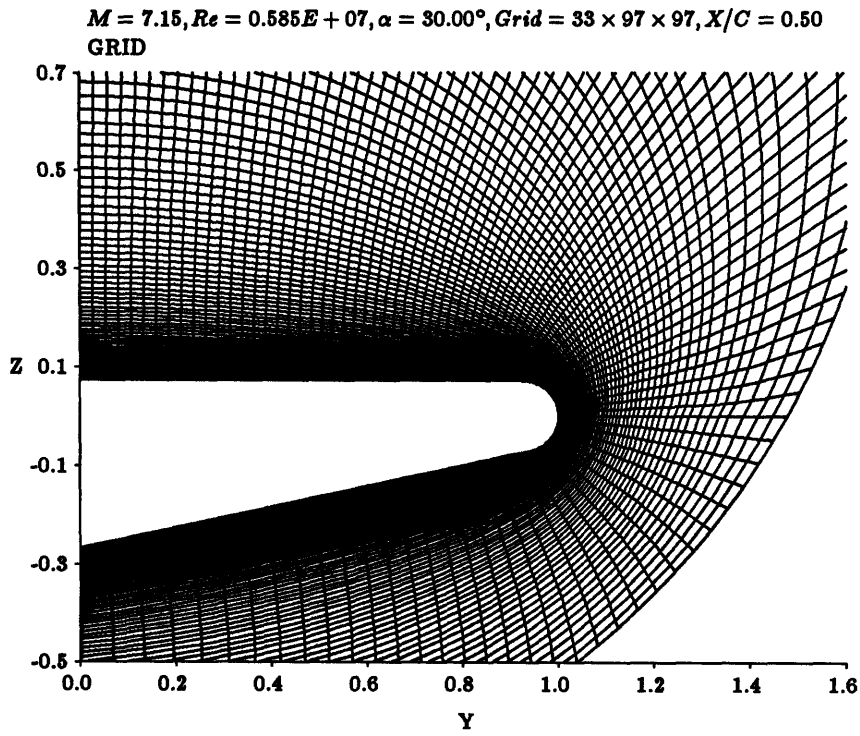
Figure 4.6: Grid used for final Navier-Stokes calculations

$Grid = 33 \times 49 \times 97, X/C = 0.80$
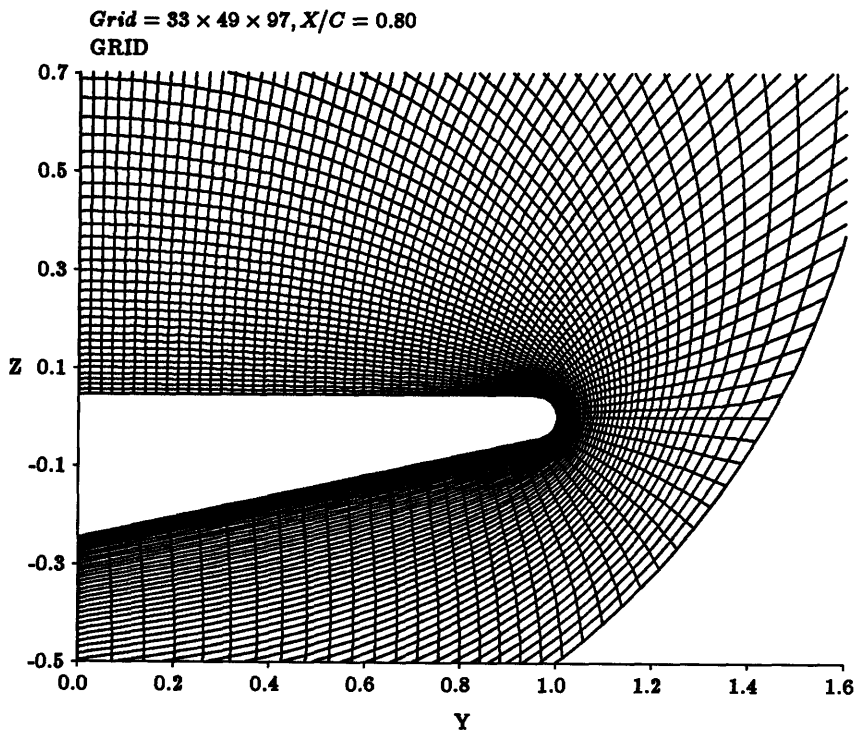GRID

Figure 4.7: Grid used for final Euler calculations

Chapter 5

Inviscid Calculations For Blunt Leading Edge Delta Wing

In certain classes of flows, for example high Reynolds number flows and flows dominated by shocks, the effects of physical viscosity can become insignificant. In these cases, it is possible to model the flow as inviscid. Since the solution to the Euler equation is much cheaper, this is a viable alternative to solving the full Navier-Stokes equations. The purpose of carrying out an Euler simulation in this thesis is to determine if the present conditions qualify the flow to be treated in an inviscid manner.

This chapter presents inviscid calculations at Mach 7.15 and 30° angle of attack. The solutions are obtained using the Jameson 4 stage temporal integration technique. The procedure for obtaining a starting solution and results exhibiting prominent features of the flow are discussed.

5.1   Solution Procedure

The starting solution was obtained on the coarse grid shown in figure 5.1 which consists of 17 streamwise, 25 body-normal and 49 circumferential stations. Through experiment it was found that initializing the flow to freestream will result in a converged solution only at 0° angle of attack. Furthermore the 2nd and 4th order dissipation coefficients had to be set at 0.5 and 0.005 respectively. It appears that

the high 2nd order dissipation is needed to damp out strong pressure overshoots in the region of a shock. The initial CFL number was set to 2.5 but had to be decreased to 1.5 at 20° angle of attack when the solution began showing signs of instability. Considerable difficulty was experienced at 30° and the 2nd order dissipation coefficient had to be increased to 1.5 to obtain convergence. All other parameters were set to the final values shown in Appendix A. The calculations averaged about 14 minutes per 100 iterations on the *AlliantFX* − 3 and the starting solution was obtained in about $3\frac{1}{2}$ hours. A plot showing the convergence history of the starting solution can be found in figure 5.2

The starting solution was interpolated onto a fine grid consisting of 33 streamwise, 49 body-normal and 97 circumferential cells (figures 5.3 and 5.4) and transfered onto a Cray2 for final calculations. After 1000 iterations and two hours of CPU time, the rms residuals dropped three orders of magnitude and the solution was considered to be converged.

5.2 Convergence Criterion

The convergence criterion used is based on the root mean square average of the density residual defined below:

$$RMS = \sqrt{\frac{1}{I \times J \times K} \sum_{i,j,k=1}^{I,J,K} \left[\frac{1}{\Delta t^2} \frac{|\rho^{n+1} - \rho^n|^2}{|\rho_\infty|^2}\right]_{i,j,k}} \qquad (5.1)$$

where I, J and K are the maximum indices in each direction of the computational coordinate. This definition of the residual which compensates for the size of the time step taken between time levels n and $n + 1$ is probably a better measure of convergence. Since time step is dependent on grid structure, a formulation that fails to factor it out can be misleading when comparing the rates of convergence between
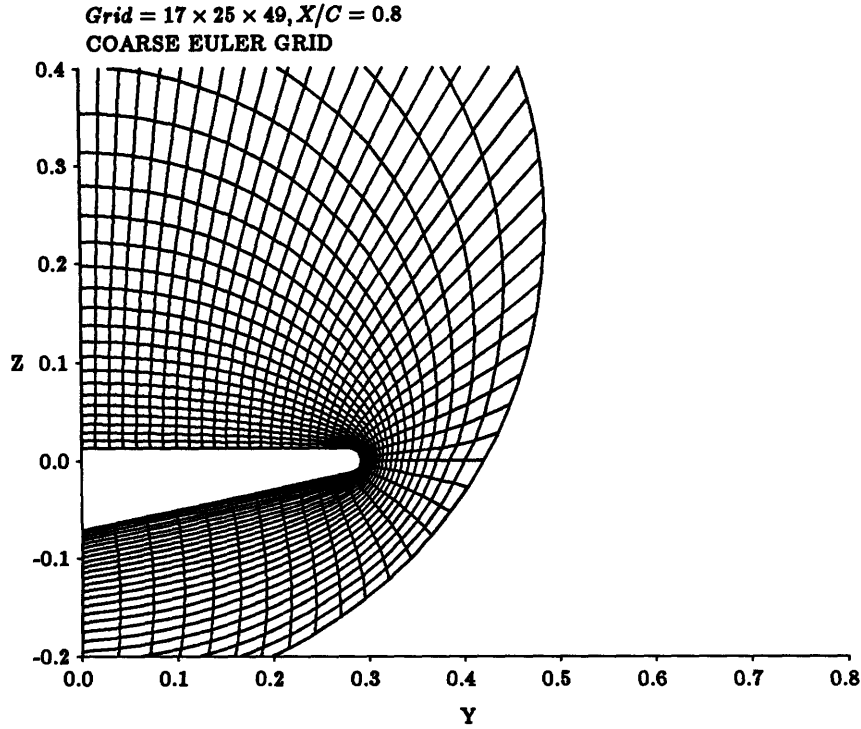
Grid = 17 × 25 × 49, **X/C** = 0.8
COARSE EULER GRID

Figure 5.1: Coarse grid used to obtain starting solution

Grid = 16 × 25 × 97
LOG_{10} RMS RESIDUAL VS ITERATION NUMBER

$\kappa_2 = 0.5$
$\alpha = 0°$
CFL = 2.5

$\kappa_2 = 0.5$
$\alpha = 10°$
CFL = 2.5

$\kappa_2 = 0.5$
$\alpha = 20°$
CFL = 1.5

$\kappa_2 = 1.5$
$\alpha = 30°$
CFL = 1.5
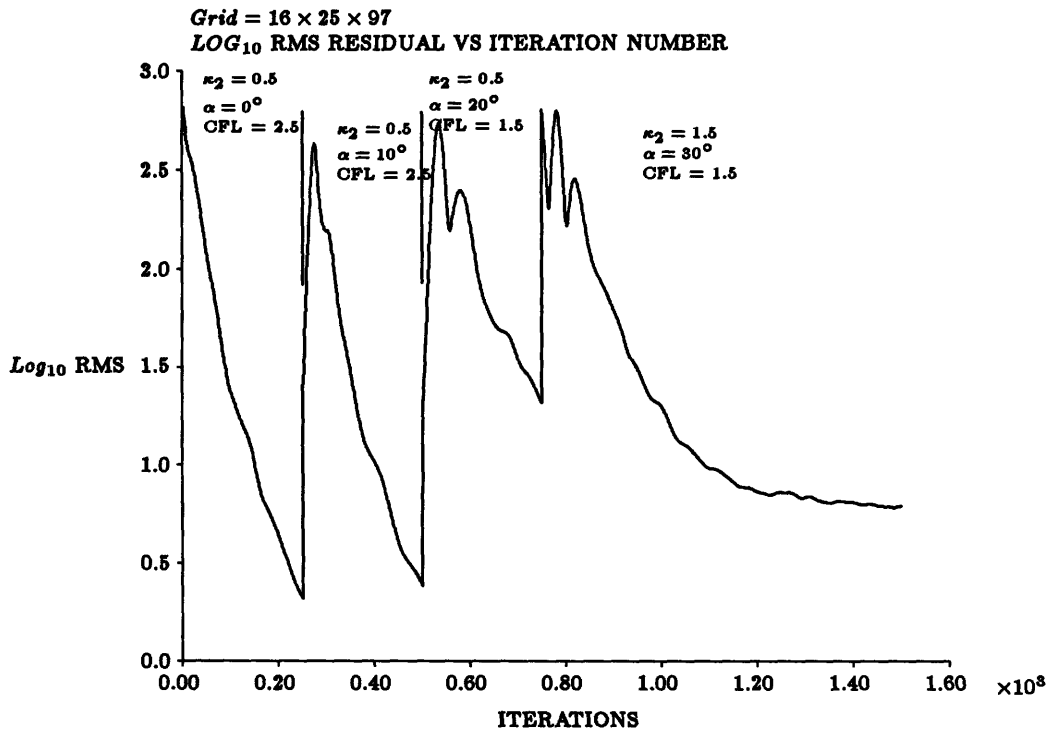
Figure 5.2: Convergence history for starting solution

Grid = 33 × 49 × 97, *X/C* = 0.80
GRID
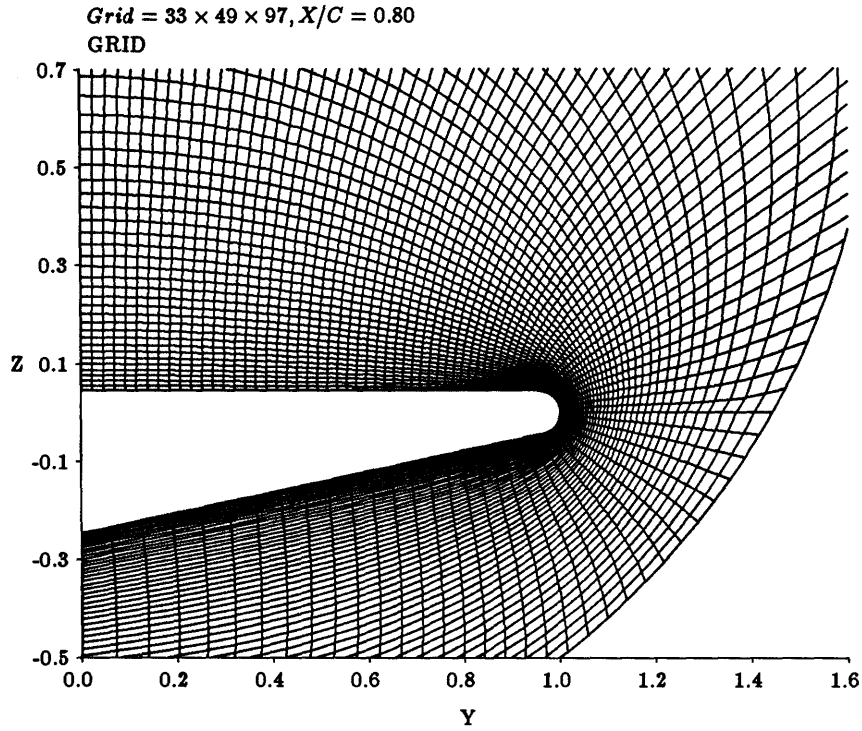
Figure 5.3: Final grid at 80% chord

Grid = 33 × 49 × 97, upper surface
GRID

Figure 5.4: Plot of final surface grid

50

$M = 7.15, Re = \infty, \alpha = 30.0°, Grid = 33 \times 49 \times 97$

LOG RMS RESIDUAL VS ITERATION NUMBER
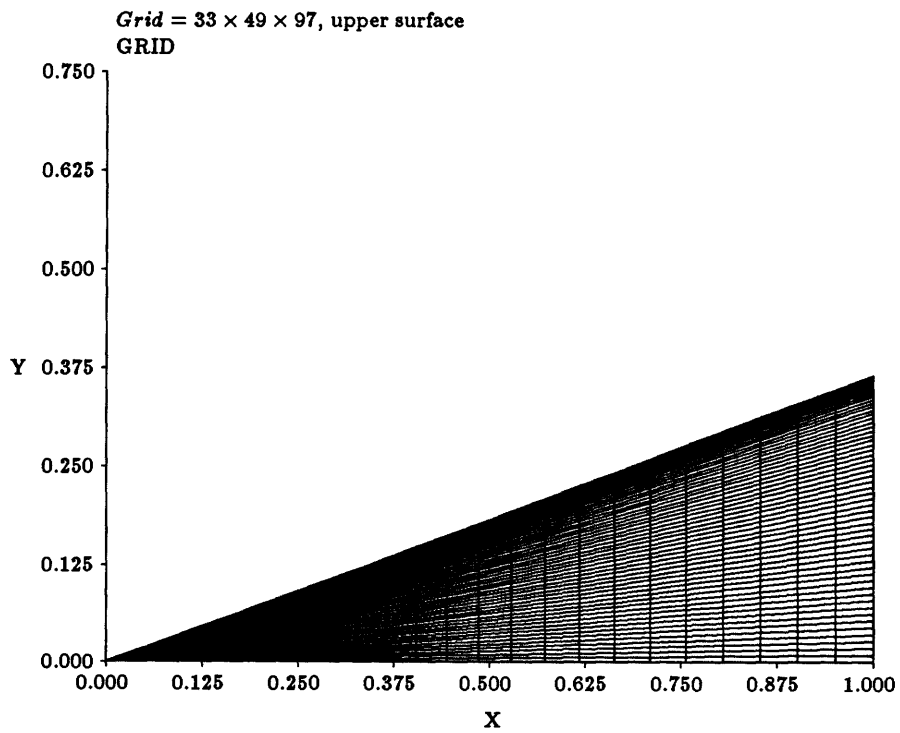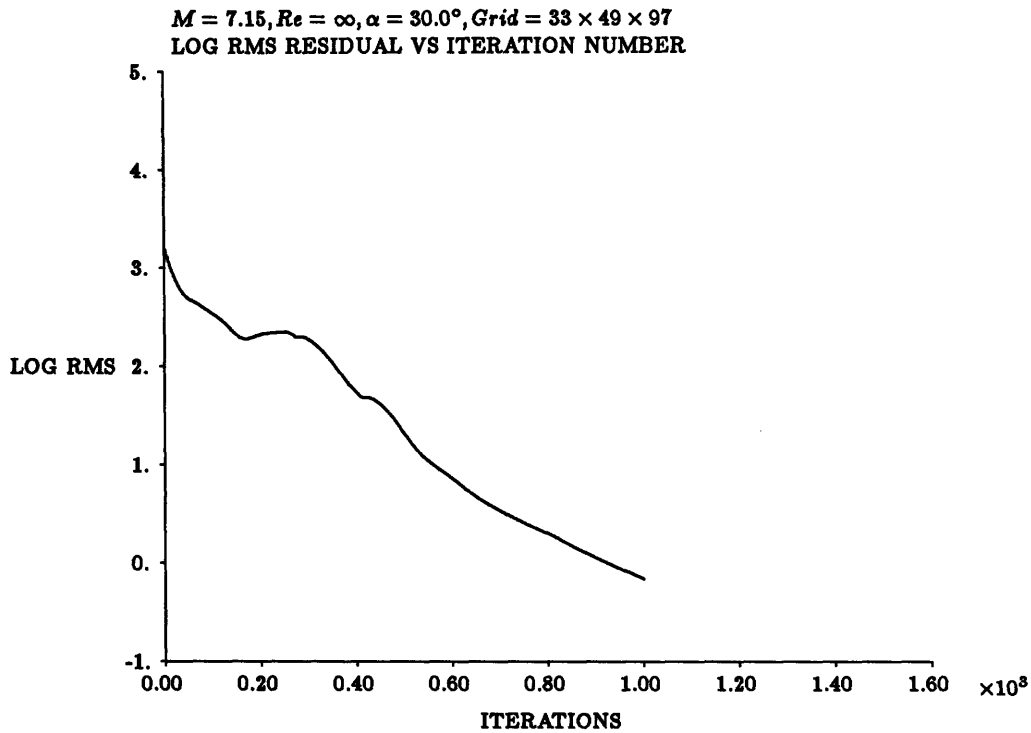

Figure 5.5: Convergence history for final solution

different grids. A plot of the residual for the final calculations is shown in figure 5.5

5.3 Results

The global values of lift and drag coefficients have the most engineering significance. The force coefficients in the normal and tangential directions are 0.6637 and 0.0593. After accounting for the tilt that results from the 30° angle of attack, the lift and drag coefficients are 0.545 and 0.383 respectively. Therefore most of the drag results from the tilting of the normal force vector.

For the purpose of displaying the results, the state vector was interpolated from the center of the cells to the nodes. The state vector at the node was taken to be the average of the values in the 8 nearest cells. At the boundaries, this technique requires values of the state vector from ghost cells outside the computational domain. In

the upstream, downstream and farfield boundaries, Reimann invariants are used to determine the boundary values in the ghost cells. However the ghost cells adjacent to the wing body require special treatment because the 'no-through-flow' boundary condition applied at the wall does not require these values to be determined during the computation, since only the pressure term contributed to the flux summation on this surface. This boundary condition implicitly assumes that the velocity vector on the surface is tangential to the wall. To obtain this result the velocity vector at the wall can be approximated by;

$$\vec{u}_{wall} = \vec{u}_1 - \vec{u}_n \qquad (5.2)$$

where $\vec{u}_1$ is the velocity vector within the first cell inside the computational domain and $\vec{u}_n$ is the component that is normal to the wing surface. To obtain this value of $\vec{u}_{wall}$, the velocity in the ghost cell must be set to;

$$\vec{u}_0 = \vec{u}_1 - 2\vec{u}_n \qquad (5.3)$$

where $\vec{u}_0$ is velocity in the ghost cell. The other components of the state vector are determined by assuming no density and pressure gradients at the wall. To reduce computation time during the graphical display process and to maintain a high level of accuracy, the value of vorticity magnitude was calculated from the cell centered values and stored into data files.

To facilitate comparison and analysis it is desirable to present data in non-dimensional forms. The definition for pressure, total pressure loss and total temperature loss coefficients are:

$$C_p = \frac{p - p_\infty}{\frac{1}{2}\rho_\infty u_\infty^2} \qquad (5.4)$$

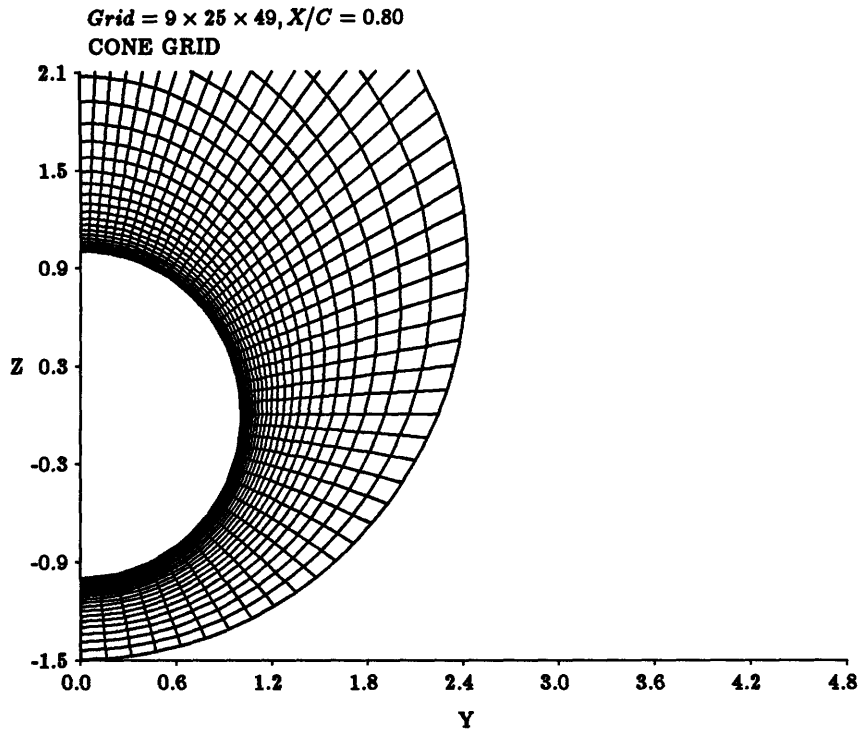$$C_{pl} = 1 - \frac{p_0}{p_{0_\infty}} \qquad (5.5)$$

Figure 5.6: Cone grid used for code validation

$$C_{tl} = 1 - \frac{T_0}{T_{0_\infty}} \tag{5.6}$$

5.3.1 Code Validation

The high second order damping coefficient needed to smooth out pressure over-shoots in the region of the shock is a source of concern. The possibility that this will introduce excessive dissipation in other regions of the flow and lead to corruption of the results is a serious issue. To determine the accuracy of this calculation, a comparison was carried out with the theoretical results obtained by [Jones] [14] for a 12.5° cone at Mach 7.0 and 12.5° angle of attack. The verification case was conducted using the same damping coefficients as the final calculations on the grid shown in figure 5.6 which consists of 9 streamwise by 25 body-normal and 49 circumferential stations. Since the solution is conical, the number of streamwise stations

is not important. In the crossflow plane, this grid has one quarter the resolution of the grid used for the final wing calculations. The lower resolution leads to a higher level of inherent dissipation. Therefore the error incurred through artificial viscosity should at least be comparable (if not lower) for the final wing calculation.

Figures 5.8 to 5.10 show the results obtained after 500 iterations and the residuals have dropped about two orders of magnitude form 1×10^4 to 0.2×10^2. The pressure correlates well with the theoretical results, but the Mach number and density are very far off. An examination of the Mach number contour plot in figure 5.11 reveals abnormal behavior near the body. Here the contour lines change direction rapidly near the body indicating the presence of some kind of layer. When the calculation was carried out for another 3500 iterations, the residual dropped to 0.3 and the results shown in figures 5.12 to 5.14 were obtained. Again the match in the pressure coefficient is very good. The correspondence between numerical and theoretical results for Mach number and density improved tremendously, although the Mach number on the leeward surface near the symmetry plane is overpredicted. The Mach number contour plots in figure 5.15 show that the contour lines approach the surface without any sudden change in direction. However the presence of a layer close to the body is still distinguishable. As the isomach lines approach the body, they become more tangential to the body surface, this effect results in the bunching up of isomach lines on the top surface of the cone.

This observation is consistent with theoretical results for inviscid high speed flows over a cone [22]. The illustration in figure 5.7 shows a crossflow section of a cone at an angle of attack. The streamline along the plane AB wets the body. Other streamlines approach the body as they move towards point A'. Another streamline moves along the plane B'A' towards the body. Since the streamlines cross the shock at different points, they experience different shock strengths. Therefore the entropy production varies from one streamline to another. The Euler equations show that the entropy along a streamline is constant, indicating that the entropy at
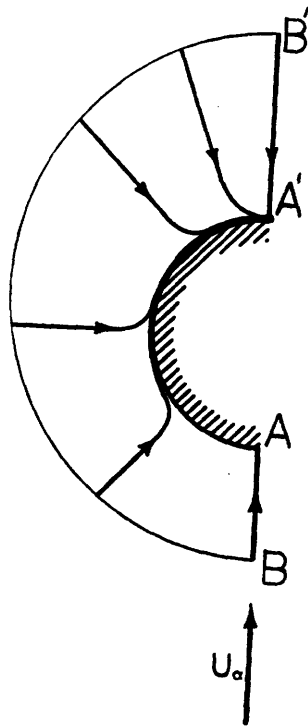
Figure 5.7: Singular points on a cone [22]

point A' on the cone is multi-valued since all streamlines converge onto this point. Furthermore the proximity of streamlines near the body results in a thin layer of rapidly changing entropy on the surface of the cone. A more detailed explanation of the above phenomena can be found in [22].

The presence of a singular point on the cone provides an explanation for the Mach number spike observed on the body in the calculated results. To capture the flow in the vicinity of this singularity, high grid resolution is necessary. Unfortunately the present grid does not fulfill this requirement. Only three circumferential stations are embedded within the region of the Mach number spike. It is unlikely that the singularity can be resolved, but the error incurred in the Mach number will decrease as we refine the singular region.

The above observation about the effects of convergence is interesting, because

it shows that the pressure coefficient converges much faster than Mach number and density. Moreover the contour plots show that the convergence of Mach number and density is only inhibited in cells near the body. The entropy layer close to the body is probably causing this deterioration, but the precise reason for this is uncertain. It is quite likely that the treatment of the dissipation near the wall is the source of this problem, so a different scheme was attempted. In the new scheme, the 4th order dissipation was taken out of the two cells nearest to the wall and the 2nd order dissipation was zeroed out in the cell adjacent to the wall. The new scheme produces essentially no difference in the results and displayed the same problems with the convergence rate near the body. If the treatment of dissipation at the wall is responsible for the poor rate of convergence near the wall, then further study in necessary .

Despite the above problems, the calculated results are in close agreement with the theory. The good match in pressure coefficient should result in equally accurate lift and drag coefficients. With the exception of the singular point, the Mach number corresponds well with the theoretical results. For the present model of the delta wing, a similar singular point is not present, therefore the Mach number mismatch at the singularity should not manifest itself in the calculation over the delta wing.

There is no indication that the high 2nd order dissipation coefficient employed in this calculation led to any significant deterioration of the results, and the good match with theoretical results indicates a reasonably high level of accuracy.

$M = 7.00, Re = \infty, \alpha = 12.50°, Grid = 9 \times 25 \times 49, X/C = 0.80$

iterations $= 500, residual \approx 0.2 \times 10^2$

PRESSURE COEFFICIENT ON THE BODY

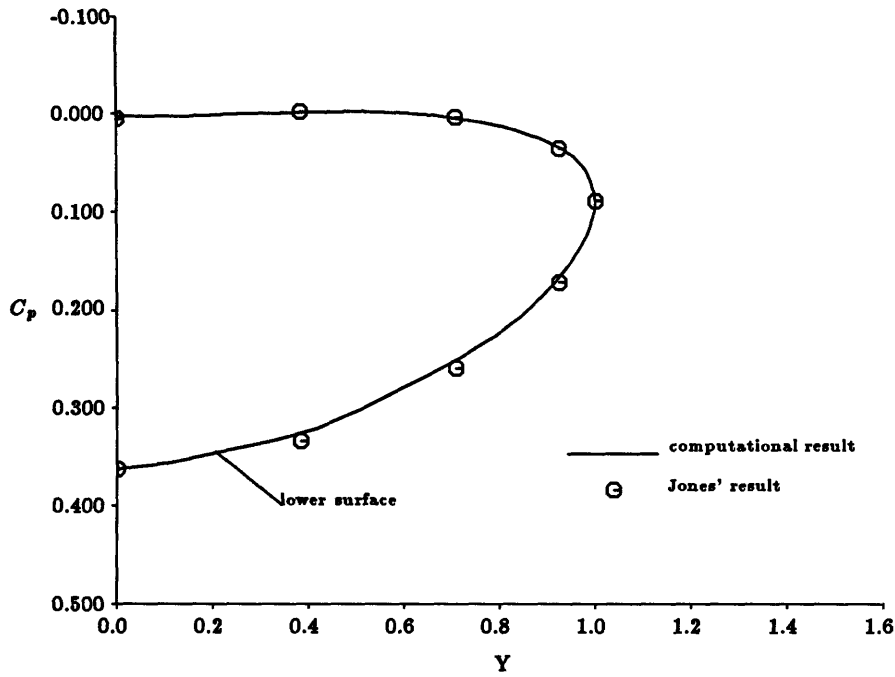Figure 5.8: Pressure coefficient on the surface before complete convergence

$M = 7.00, Re = \infty, \alpha = 12.50°, Grid = 9 \times 25 \times 49, X/C = 0.80$

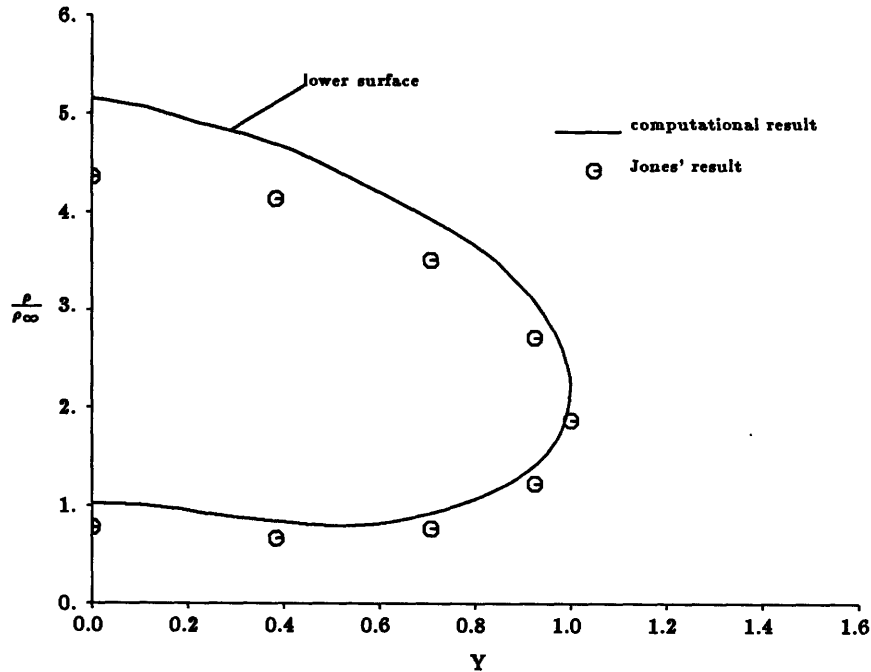*iterations* $= 500, residual \approx 0.2 \times 10^2$

DENSITY ON THE BODY

Figure 5.9: Density on the surface before complete convergence

57

$M = 7.00, Re = \infty, \alpha = 12.50°, Grid = 9 \times 25 \times 49, X/C = 0.8000$

iterations $= 500, residual \cong 0.2 \times 10^2$

MACH NUMBER ON BODY
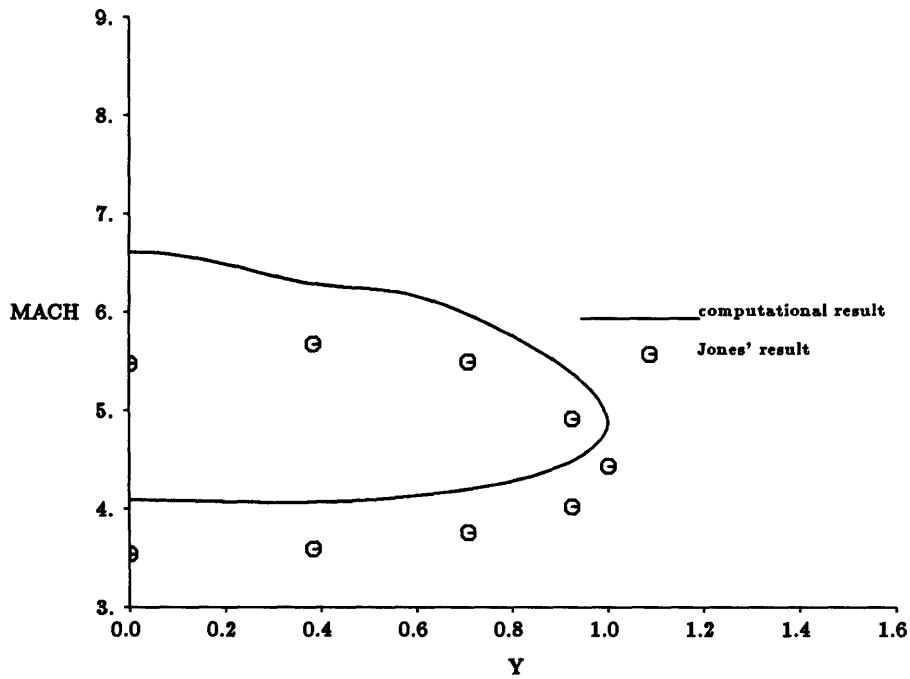

Figure 5.10: Mach number on the surface before complete convergence

$M = 7.00, Re = \infty, \alpha = 12.5°, Grid = 9 \times 25 \times 49, X/C = 0.80$

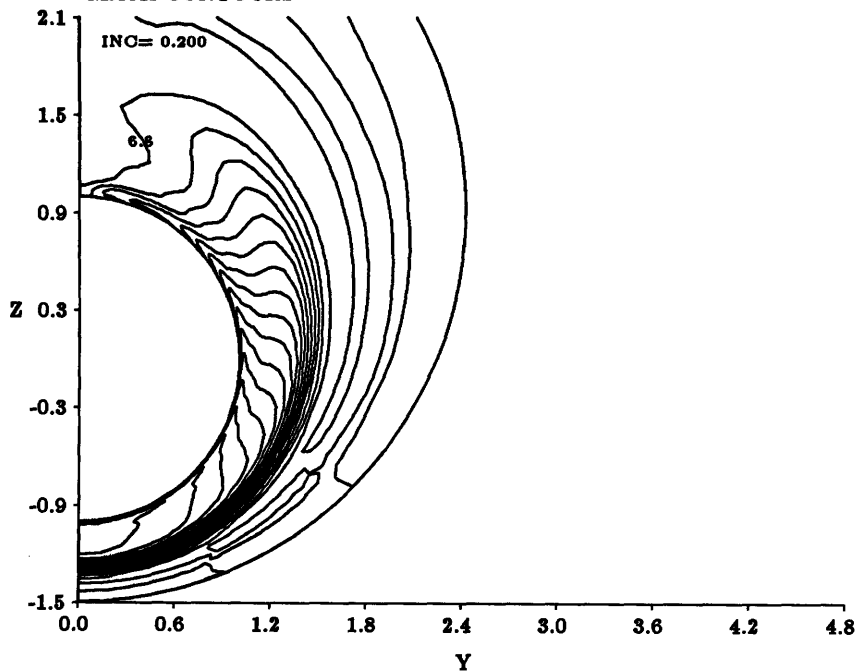*iterations* $= 500, residual \approx 0.2 \times 10^2$

MACH CONTOURS

Figure 5.11: Mach number contours before complete convergence

58

$M = 7.00, Re = \infty, \alpha = 12.50°, Grid = 9 \times 25 \times 49, X/C = 0.80$
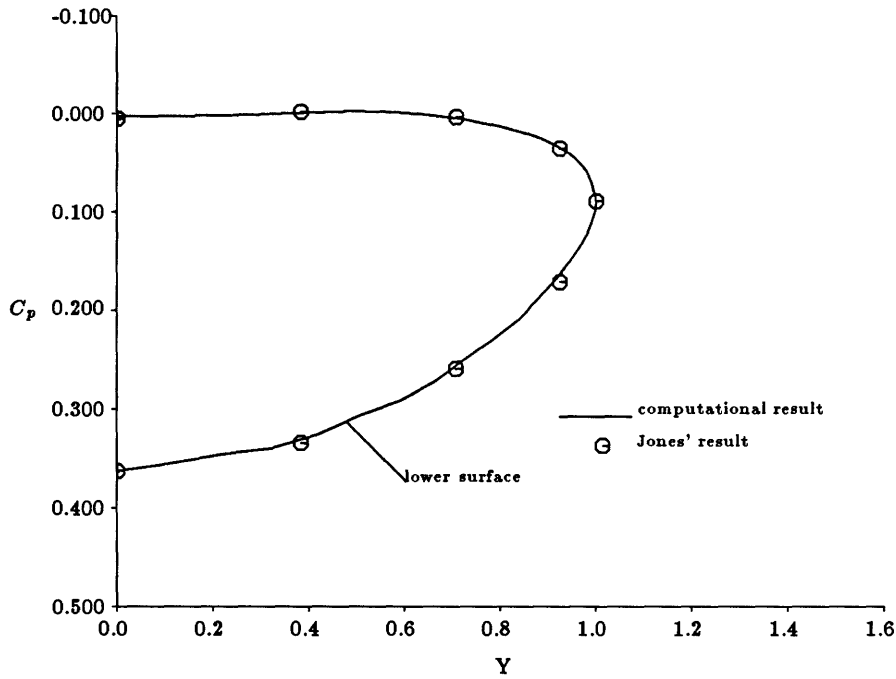$iterations = 4000, residual \approx 0.3$
PRESSURE COEFFICIENT ON THE BODY

Figure 5.12: Pressure coefficient on the surface

$M = 7.00, Re = \infty, \alpha = 12.50°, Grid = 9 \times 25 \times 49, X/C = 0.80$
$iterations = 4000, residual \approx 0.3$
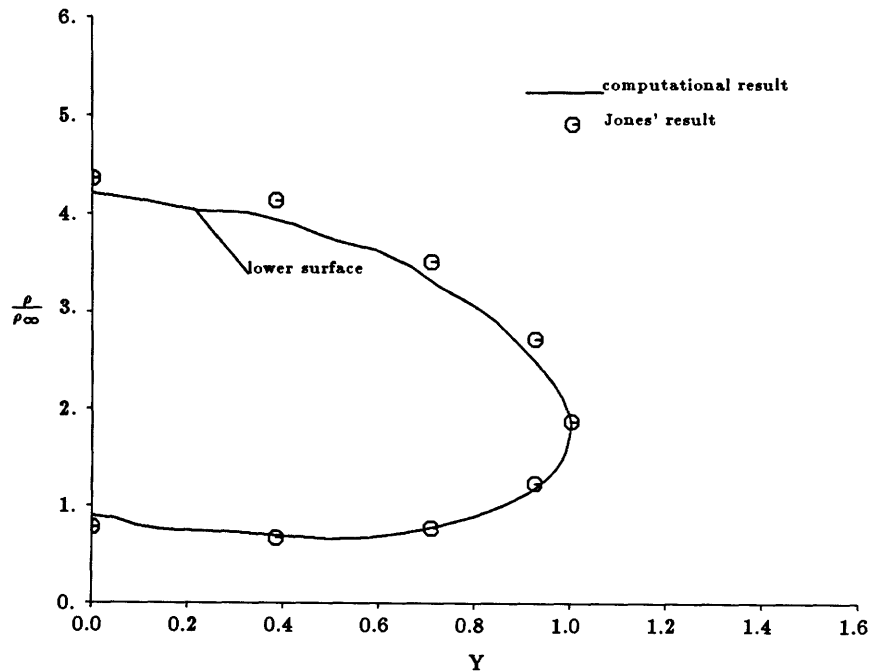DENSITY ON THE BODY

Figure 5.13: Density on the surface

59

$M = 7.00, Re = \infty, \alpha = 12.50°, Grid = 9 \times 25 \times 49, X/C = 0.80$
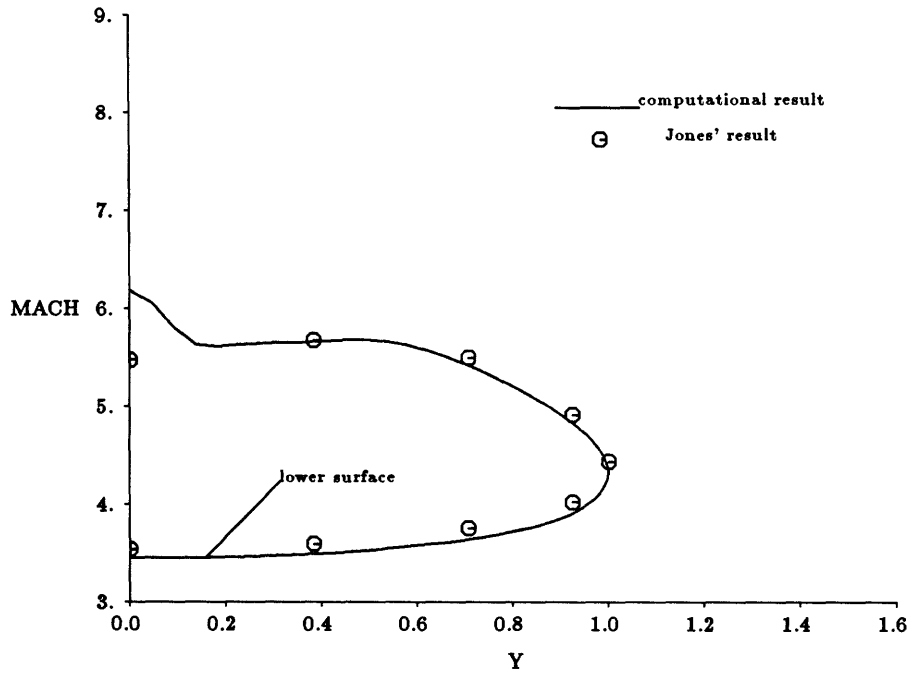*iterations* $= 4000, residual \approx 0.3$
MACH NUMBER ON THE BODY

Figure 5.14: Mach number on the surface

$M = 7.00, Re = \infty, \alpha = 12.5°, Grid = 9 \times 25 \times 49, X/C = 0.80$
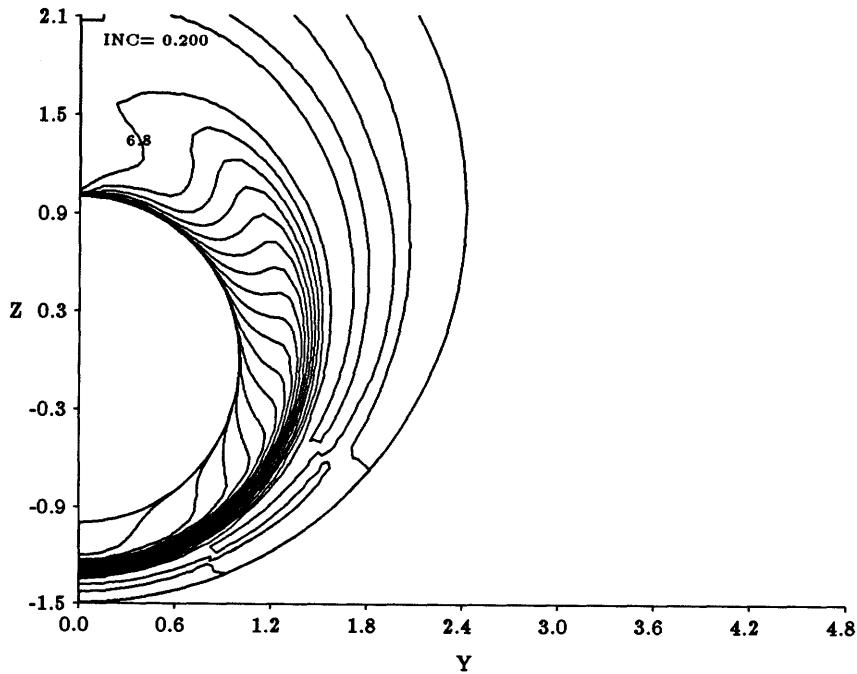*iterations* $= 4000, residual \approx 0.3$
MACH CONTOURS

Figure 5.15: Mach number contours

5.3.2 Flow Features on the Upper Surface

Density and pressure coefficient contours for the wing upper surface are shown in figures 5.16 and 5.17. Both plots appear similar, displaying very little variation over much of the wing. Only a thin strip of constant width near the leading edge show significant changes in values. A comparison with the grid will reveal that the limit of this region coincides with the start of the rounding at the leading edge. This observation highlights the importance of the rounding in determining the rate of expansion around the leading edge. The total pressure coefficient plot also shows no major variation on this surface, but this observation may be misleading because most of the total pressure of the flow is lost after passing through the primary shock. The changes in total pressure become masked and even strong shocks will not show up well. On the upper surface only about 1% of the freestream total pressure is left. A hypothetical shock with a normal Mach number of 1.9 (which looses about 25% of its total pressure) would bring the total pressure down to 0.75% of the freestream value, a change of only 0.25% in the total pressure loss coefficient.

Contrary to the nearly featureless surface plots of density, pressure and total pressure loss coefficients, the contour plot of Mach number in figure 5.18 shows significant variation. It is most useful to examine this with the surface streamlines and velocity vector diagrams in figures 5.19 and 5.20. All three plots indicate that something is happening at about midspan. In the streamlines plot, this is the region where streamlines converge. The observation indicates that this line is either a shock or a separation region. The difference in the nature of the flow across the this line is vividly illustrated by the Mach number contour plot in figure 5.18. Outboard of the line, the Mach number is mostly monotonically increasing, with the strongest variation occurring around the leading edge. Across the line, the Mach number drops precipitously and is accompanied by a significant change in the contour pattern inboard of the line. Contour lines now run in a more lengthwise manner from the apex to the trailing edge, indicating a more streamwise direction in

61

the nature of the flow. This feature is confirmed by plots of surface streamlines and velocity vectors. Velocity vector plots show that along the line, the flow is turned suddenly. This provides further evidence of a shock. The same plots also indicate that inboard of the line, reverse flow occurs. The above observations suggest that this could be a region of shock-induced separation. However the velocity vectors in the 'separated region' appears very regular. This lack of irregularity is unusual for separated flows and seems to indicate that something else may be happening here. However the present evidence is inadequate and further discussion of the flow in this region will be held over until the cross-flow plots have been examined.

Very little total temperature loss occurs over the surface of the wing. Since this is an inviscid calculation, there should be no total temperature loss, and the average value of 0.5% obtained in this calculation is clearly within acceptable limits. The plot of total pressure loss indicates a significant increase near the leading edge. Since this is an expansion region, this cannot be physically possible, and must come form a numerical source. Discussion of this anomaly will be held over until the later part of this chapter.

$M = 7.15, Re = \infty, \alpha = 30.0°, Grid = 33 \times 49 \times 97$, wing upper surface
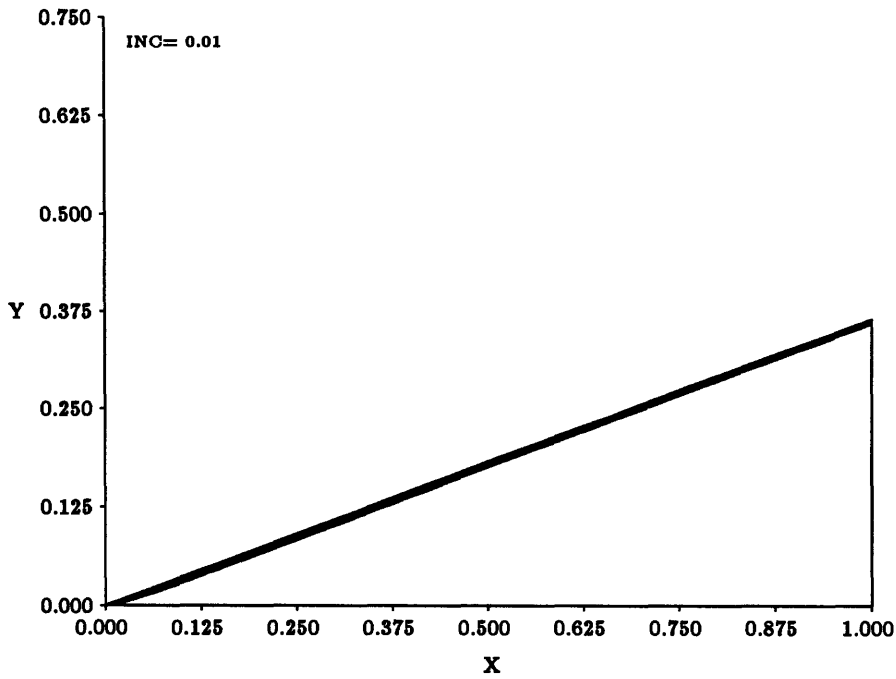DENSITY CONTOURS

Figure 5.16: Plot of surface density

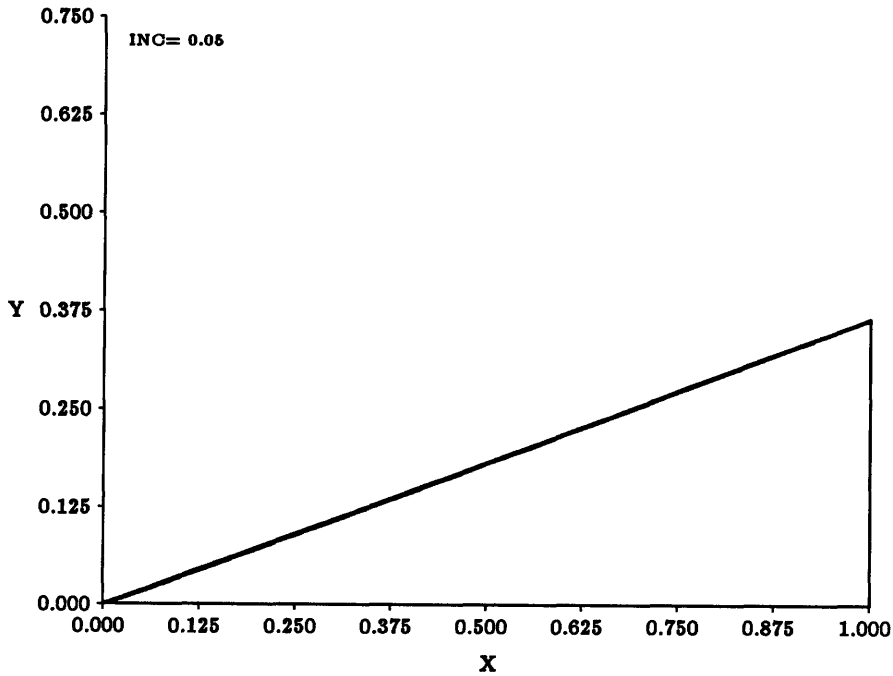$M = 7.15, Re = \infty, \alpha = 30.0°, Grid = 33 \times 49 \times 97$, wing upper surface
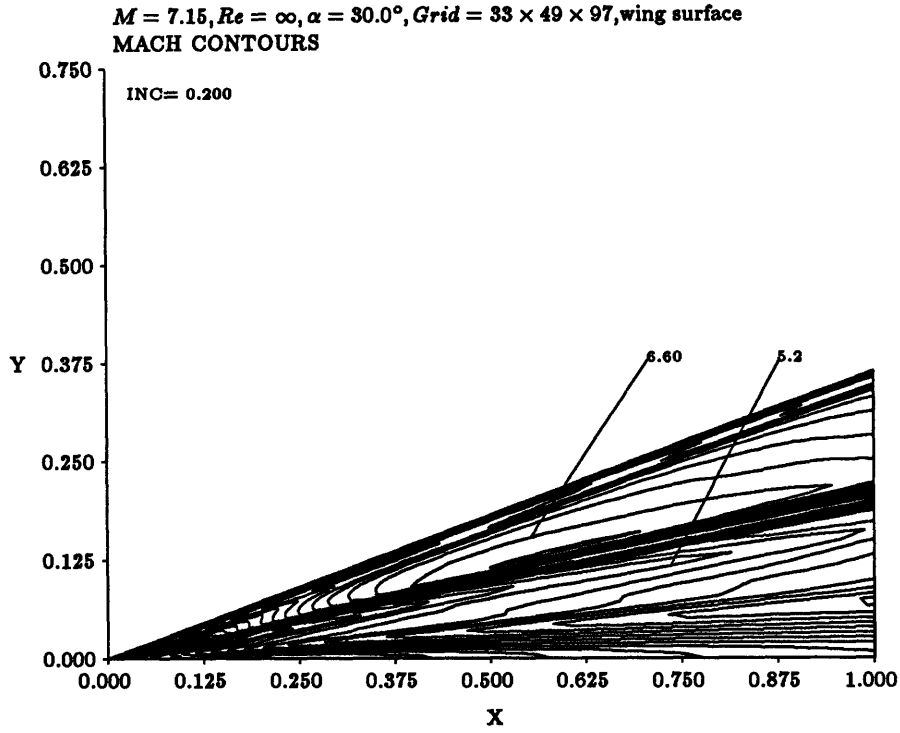C_p

Figure 5.17: Plot of surface pressure coefficient

$M = 7.15, Re = \infty, \alpha = 30.0^\circ, Grid = 33 \times 49 \times 97$, wing surface
MACH CONTOURS

Figure 5.18: Plot of surface Mach number

$M = 7.15, Re = \infty, \alpha = 30.0^\circ, Grid = 33 \times 49 \times 97$, Wing upper surface
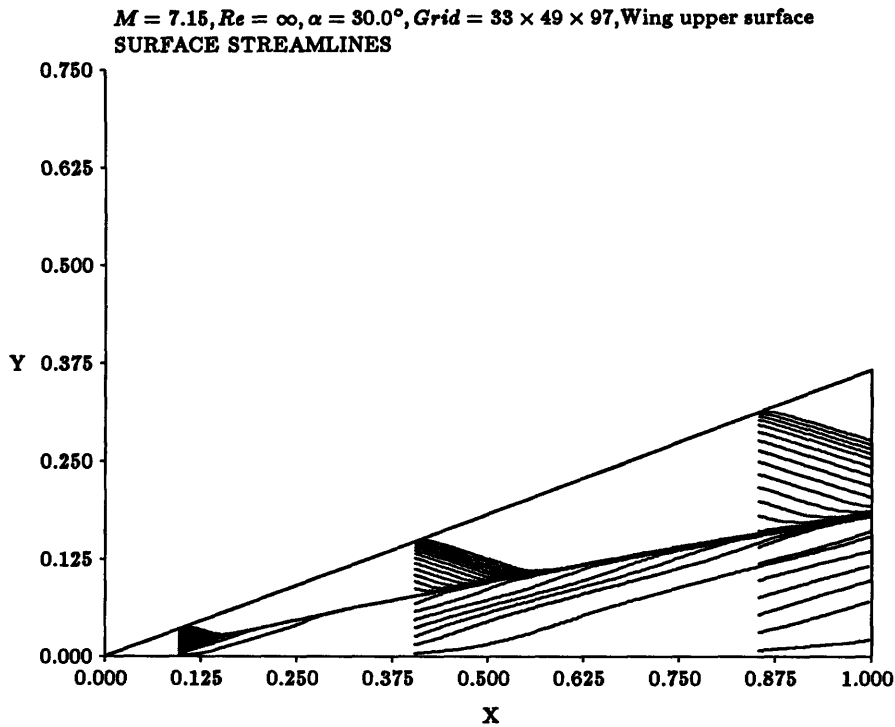SURFACE STREAMLINES

Figure 5.19: Plot of surface streamlines

64

$M = 7.15, Re = \infty, \alpha = 30.0°, Grid = 33 \times 49 \times 97$, wing upper surface
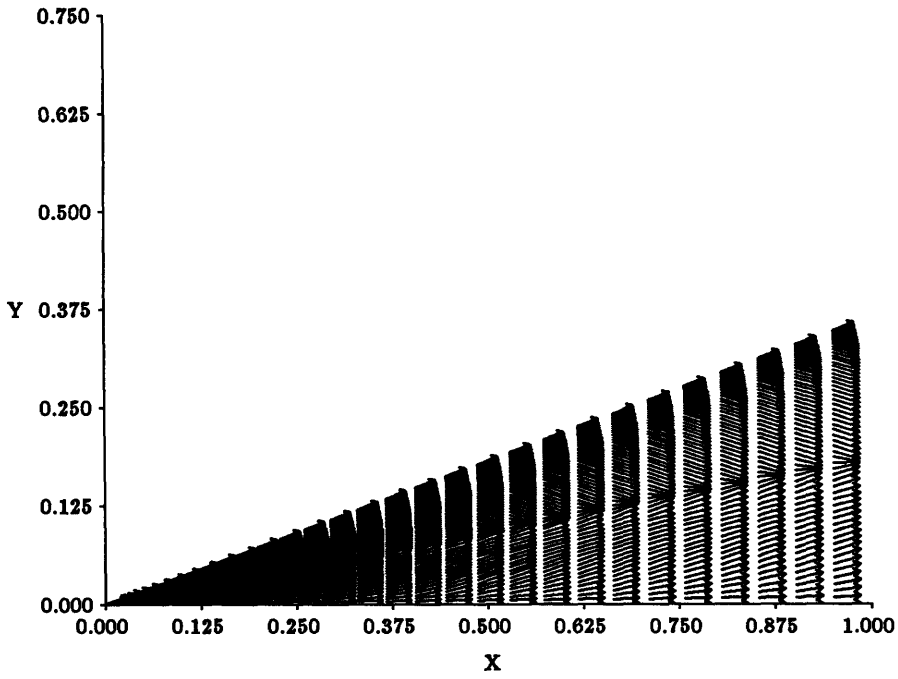
V-W VELOCITY VECTOR PLOT

Figure 5.20: Plot of surface velocity vectors

$M = 7.15, Re = \infty, \alpha = 30.0°, Grid = 33 \times 49 \times 97$, wing upper surface

TOTAL TEMPERATURE LOSS CONTOURS
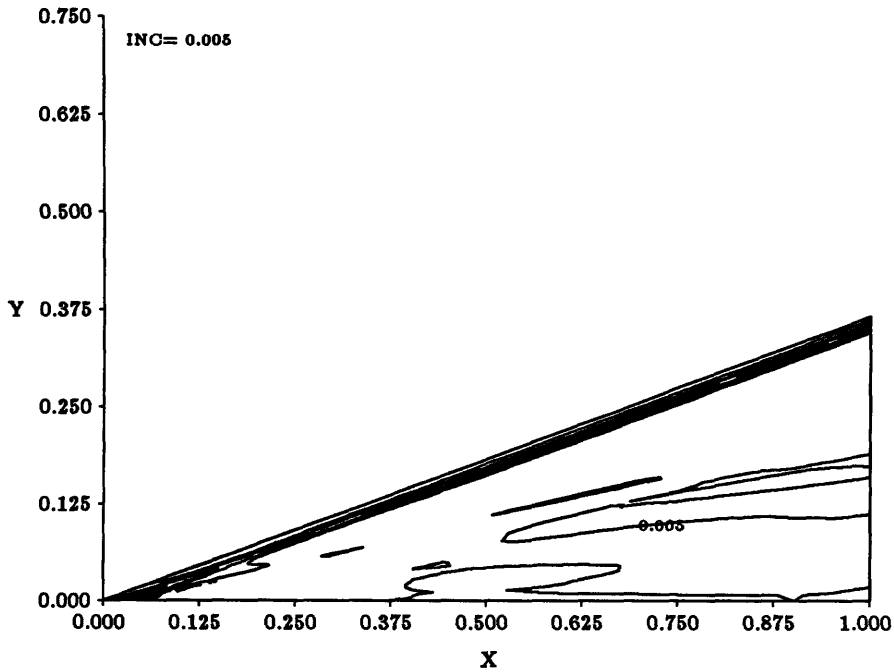

Figure 5.21: Plot of surface total temperature loss

$M = 7.15, Re = \infty, \alpha = 30.0^\circ, Grid = 33 \times 49 \times 97,$wing upper surface
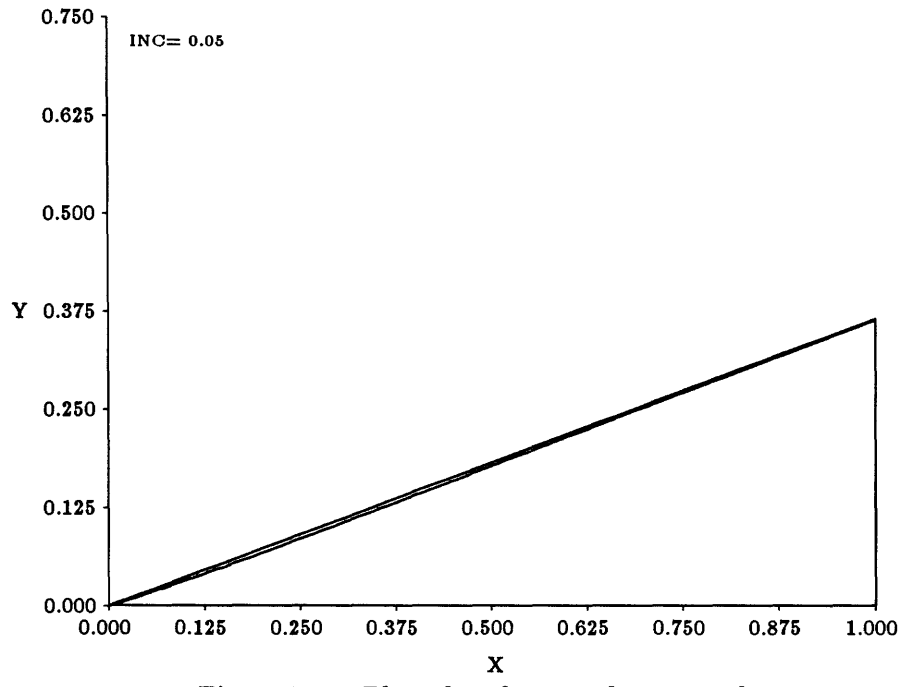
TOTAL PRESSURE LOSS CONTOURS

INC= 0.05

Figure 5.22: Plot of surface total pressure loss

5.3.3 Flow Features at 50% and 80% Chord

The plots of density and pressure coefficient bear close resemblance to each other. The values on most of the wing surface show very little variation with the exception of the leading edge where drastic changes occur within the small region that coincides with the tip rounding. Surface diagrams in figures 5.23 to 5.26 indicate that the changes at the leading edge are more abrupt on the leeward side of the wing, where significant variations start occurring at about 95% span. On the windward surface, both density and pressure coefficient start dropping at about 85% span. There are no major differences between the plots at the 50% and 80% chord positions. At both locations, the density changes from about 4.8 on the windward surface to almost 0 on the leeward side, while pressure coefficient changes from about 0.65 to -0.025.

It is possible to obtain theoretical estimates of the values of density and pressure coefficient on the windward surface of the wing. At the root, the lower surface of the wing is tilted at about $-4°$ from the wing centerline. Therefore at a 30° angle of attack, the windward surface is inclined at about 34° to the freestream. Using a 34° wedge as a model for the windward surface, the pressure coefficient can be calculated from Newtonian theory [Hayes & Probstein '59] [8]. The theory states that the pressure coefficient is,

$$C_p = 2sin^2(\sigma) \tag{5.7}$$

where σ is the inclination angle of the solid surface to the freestream. With a σ of 34°, the C_p comes out to be about 0.63. This figure matches well with the calculated results for the windward surface of the wing.

From the shock relations, it is possible to estimate the density on the windward surface of the wing. The angle that the shock makes with the lower surface is approximately $-5°$. Therefore the shock is inclined at an angle of 39° to the freestream. This gives a Mach number of about 4.5 normal to the shock. The density jump $\left(\frac{\rho_2}{\rho_1}\right)$

across a shock of this strength is about 4.8, and the ratio of the total pressures $\left(\frac{P_2^o}{P_1^o}\right)$ is 0.0917. This density change matches the value obtained form the simulations and the total pressure jump gives a total pressure loss of 91% across the shock. It will be shown later that this value also corresponds well with calculated results.

Contour plots of density and pressure coefficients presented in figures 5.27 to 5.30 indicate very clearly the location of the primary shock and expansion regions. Besides this they present very little information that cannot already be deduced from the plots of surface quantities. The wiggles that appear outside the shock result from noise of a numerical nature, but do not lead to any corruption of the solution.

Plots of surface Mach number are presented in figures 5.31 and 5.32. Unlike cross-sectional diagrams of density and pressure coefficients, these plots show considerable variations. The Mach number profile on the upper surface shows 3 distinct peaks, the most significant being located at approximately 60% span. Here the Mach number drops drastically from about 7.0 to 4.0. A change in Mach number of this magnitude is most likely the result of a shock. Cross-flow (v,w) velocity vector diagrams in figures 5.34 and 5.36 show that this point is the confluence of flows moving outwards and inwards. Crossflow Mach number plots in figures 5.37 and 5.38 indicate that the flows are converging onto this point at supersonic speeds thereby confirming the presence of a shock here. The blowups of velocity vector plots in figures 5.39 and 5.40 provide further confirmation of a shock on the leeward surface. At the shock location, only the normal of velocity going into shock the gets changed while the other components are preserved.

The contour plots of Mach number in figures 5.33 and 5.35 reveal alot of information about the flowfield. The structure and location of shocks and separation points are shown clearly. On the top surface, something is clearly happening at the 60% span position. Previous analysis showed that this corresponds to a shock on

the wing. A shock like structure can be seen leaving this point making an angle of about 20° with the wing surface. To determine if this is an oblique shock it is helpful to take a closer look at the crossflow Mach number plots in figures 5.37 and 5.38. Together with velocity vector plots in figures 5.34 and 5.36 it is possible the make an estimate of the normal Mach number going into the suspected shock . This analysis reveals that the normal Mach number going into the 'oblique shock' falls within the transonic range. The estimates range from 0.8 to 1.2 depending on the locations of the points where the crossflow Mach number is read and the estimate of the angle of the 'oblique shock'. This result casts doubts on the existence of a shock in this region. A careful examination of the velocity vector plots will reveal that the flow starts changing direction before it reaches the suspected 'oblique shock'. The rapid Mach number changes (which originally led us to suspect the possibility of a shock) occurs within a region of parallel flow providing evidence of a shear layer. It is not possible to conclude definitively the nature of the flow structure. Near the body the velocity vector plots seem to indicate an oblique shock, but as the layer leaves the body it gradually transitions into a more shear layer like structure. It appears that this structure is the result of the interaction between a shock and a shear layer.

Trapped between the shear/shock interaction layer and the body is a vortex. Figures 5.39 and 5.40 illustrates clearly the nature of the flow in this region. The vorticity probably originates from the curved primary shock on the windward surface. Flows passing through the shock at different points will encounter different shock strengths. The variation in shock strength generates vorticity which then convects towards the body surface. It is possible that the vortex observed on the leeward surface results from vorticity convected along the wall from the windward surface. The cross-flow shock causes the 'vorticity layer' to leave the body and form a vortex core. The presence of a vortex explains the regularity of the velocity vectors in the 'separated' region as observed in the surface plots earlier.

Further away from the body, a secondary shock can be observed running approximately parallel to the symmetry plane. At the lower end, this shock meets the shock/shear layer coming from the wing surface. Further evidence of a shock is provided by plots of thresholded total pressure loss in figures 5.49 and 5.51. These plots display only total pressure losses in excess of 90%. From these the location of the secondary shock running parallel to the symmetry plane is unmistakable. As a result of the shock orientation, the Mach number normal to the shock will not have any z component. Therefore x-y Mach numbers can be used to estimate the strength of this shock. Although this process can get rather tedious, it is worthwhile to see if the normal Mach number corresponds to the total pressure loss across the secondary shock.

Plots at station $J = 26$ are shown in figures 5.43 to 5.45. This station was picked because it corresponds to the location $\frac{Z}{Y_{le}} = 0.5$ in the Mach contour plot in figure 5.35. At this location, the secondary shock is well defined and readings can be taken with a minimum amount of ambiguity. Figure 5.43 indicates that the x-y component of Mach number at the 80% chord position is about 7.8. From this and the plot of u-v velocity vectors in figure 5.44, it was found that the angle between the shock and the local flow direction is about 21°. These results indicate a normal Mach number of 2.80 going into the shock. The total pressure loss readings in figure 5.45 gives a total pressure jump of 0.367 which corresponds to a normal Mach number of 2.86. The match between the two results is very good and both independently confirm the presence of a secondary shock.

Total pressure loss plots on the body show an 8% increase near the leading edge. Since there are no shocks in this region, the loss cannot be physical and must come form a numerical source. However the exact nature of this source of error is uncertain. Numerical dissipation is a possible culprit, but zeroing out the dissipation in the 2 cells closest to the body did not remedy the situation. Using the normal momentum equations to determine the wall pressure similarly did not

improve the situation. So far the problem has defied quick and simple solutions, and further study into this problem may be necesary.

Figures 5.52 to 5.55 show very low values of total temperature loss. In an inviscid calculation there should be no total temperature loss. The maximum magnitude of about 0.5%, is within acceptable error limits. Vorticity magnitude plots are shown in figures 5.56 and 5.57. They indicate that vorticity is being generated at the primary shock. On the leeward surface a high value is observed in the 'separated' region where the vortex resides.

$M = 7.15, Re = \infty, \alpha = 30.0°, Grid = 33 \times 49 \times 97, X/C = 0.50$
DENSITY ON THE BODY
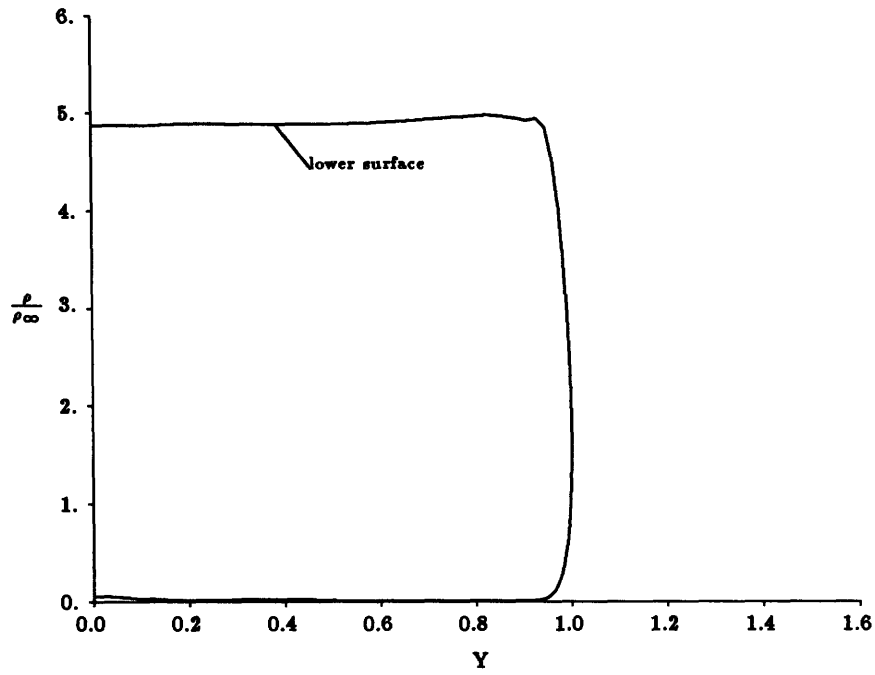
Figure 5.23: Density on the wing surface at 50% chord

$M = 7.15, Re = \infty, \alpha = 30.0°, Grid = 33 \times 49 \times 97, X/C = 0.80$
DENSITY ON THE BODY
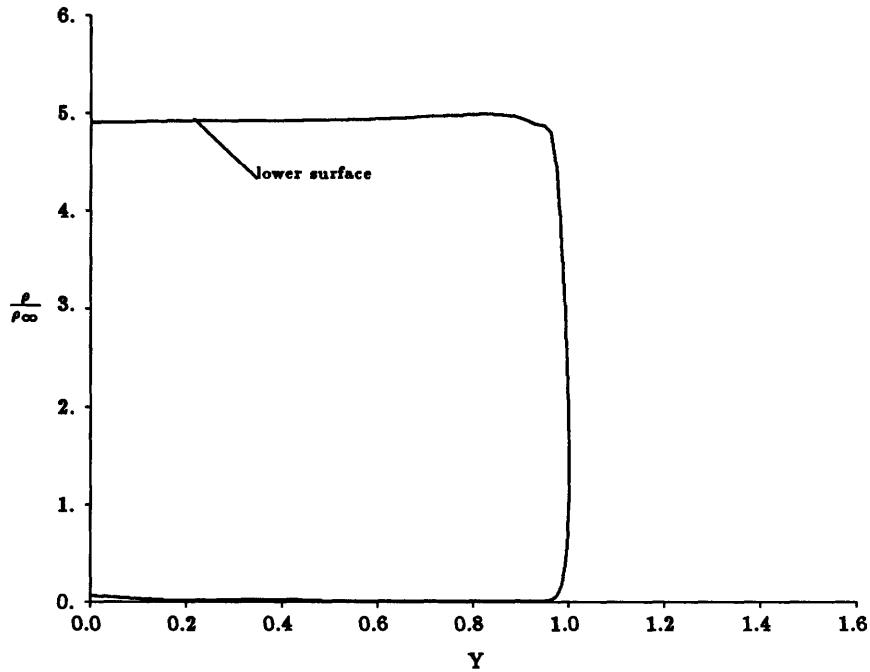
Figure 5.24: Density on the wing surface at 80% chord

$M = 7.15, Re = \infty, \alpha = 30.0°, Grid = 33 \times 49 \times 97, X/C = 0.50$
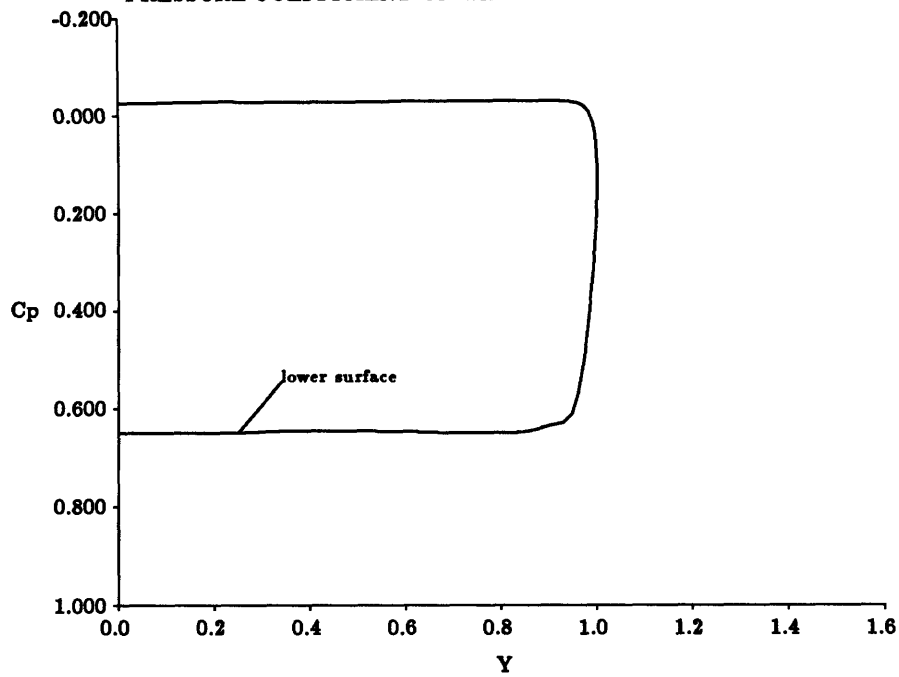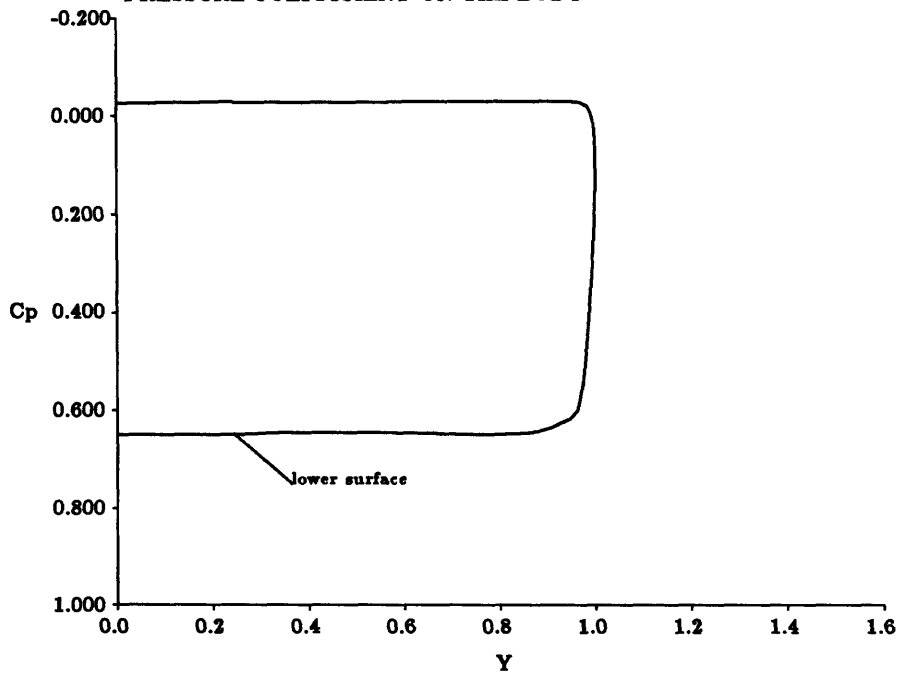PRESSURE COEFFICIENT ON THE BODY

Figure 5.25: C_p on the wing surface at 50% chord

$M = 7.15, Re = \infty, \alpha = 30.0°, Grid = 33 \times 49 \times 97, X/C = 0.80$
PRESSURE COEFFICIENT ON THE BODY

Figure 5.26: C_p on the wing surface at 80% chord

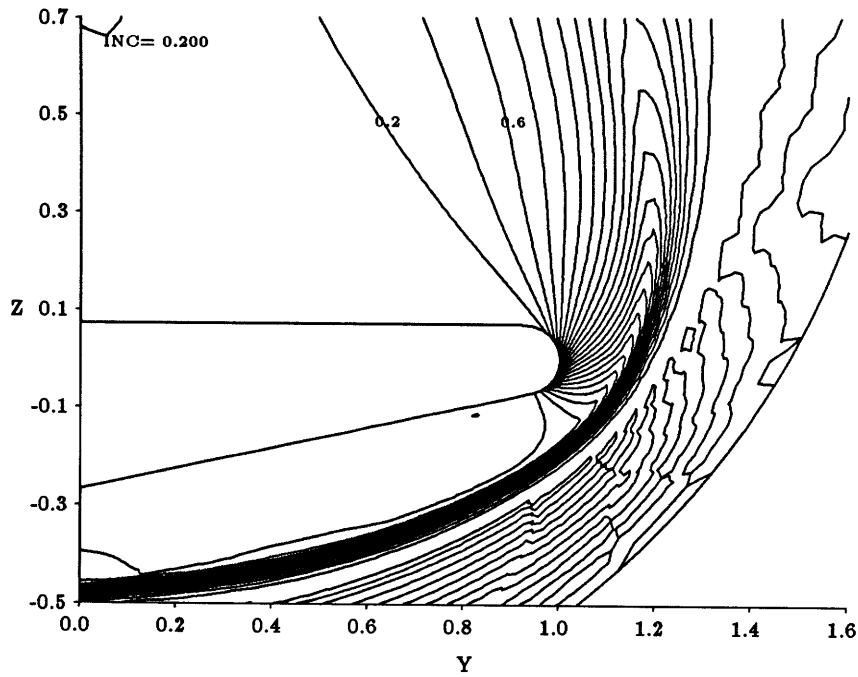$M = 7.15, Re = \infty, \alpha = 30.0°, Grid = 33 \times 49 \times 97, X/C = 0.50$
DENSITY CONTOURS

INC= 0.200

Figure 5.27: Contour plot of density at 50% chord

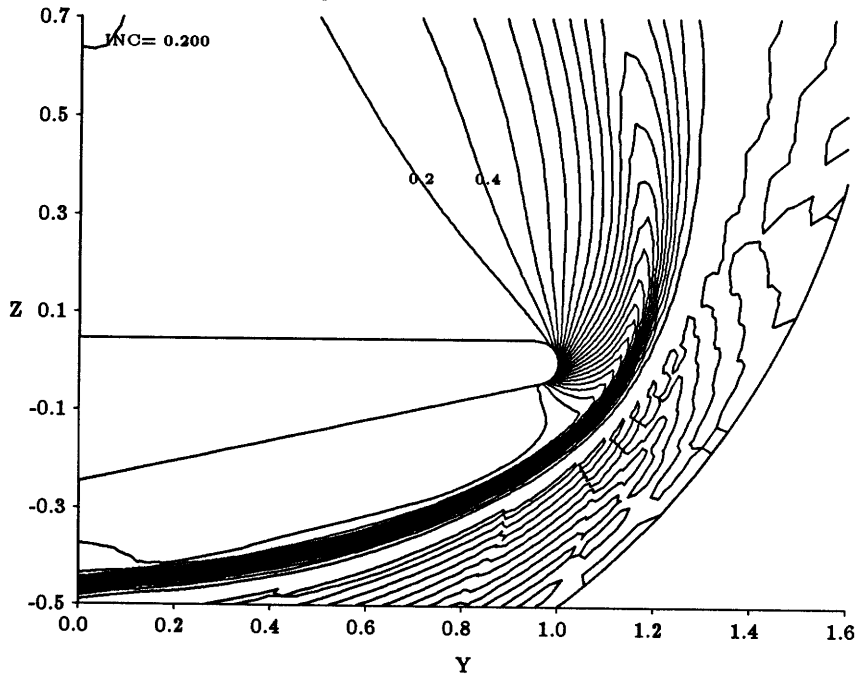$M = 7.15, Re = \infty, \alpha = 30.0°, Grid = 33 \times 49 \times 97, X/C = 0.80$
DENSITY CONTOURS

INC= 0.200

Figure 5.28: Contour plot of density at 80% chord

74

$M = 7.15, Re = \infty, \alpha = 30.0°, Grid = 33 \times 49 \times 97, X/C = 0.50$
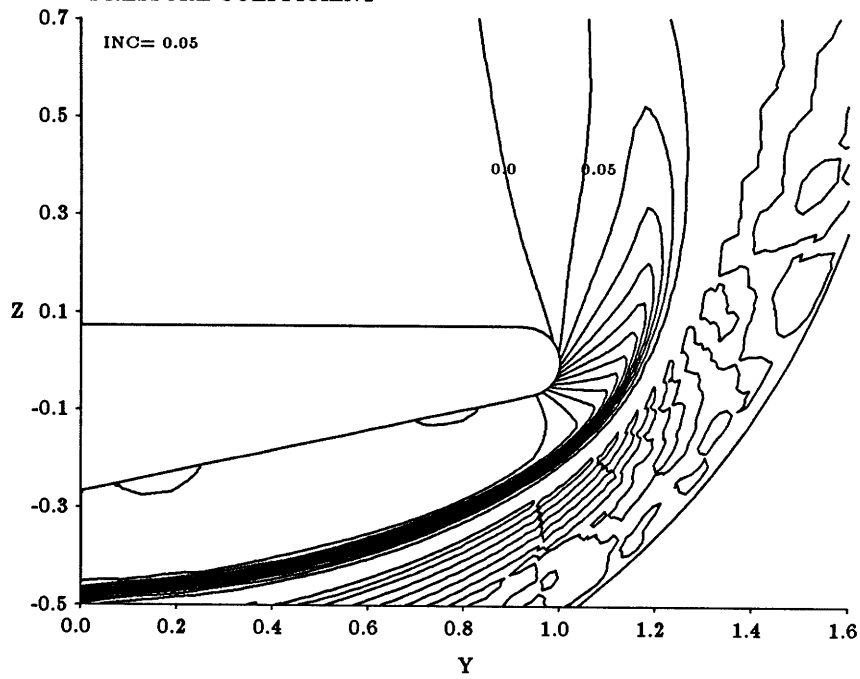PRESSURE COEFFICIENT

Figure 5.29: Contour plot of C_p at 50% chord

$M = 7.15, Re = \infty, \alpha = 30.0°, Grid = 33 \times 49 \times 97, X/C = 0.80$
PRESSURE COEFFICIENT

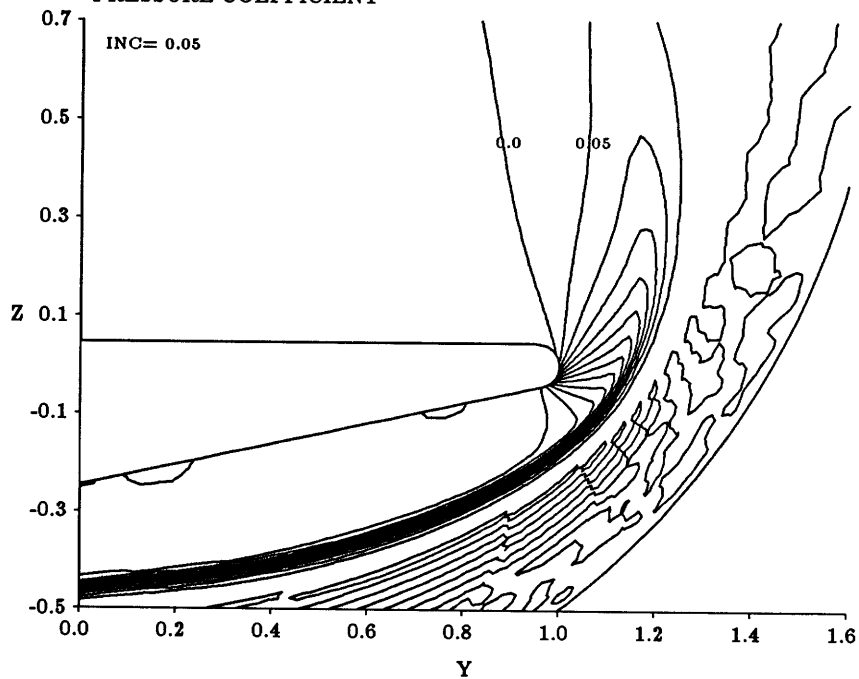Figure 5.30: Contour plot of C_p at 80% chord

75

$M = 7.15, Re = \infty, \alpha = 30.0°, Grid = 33 \times 49 \times 97, X/C = 0.50$
MACH NUMBER ON THE BODY

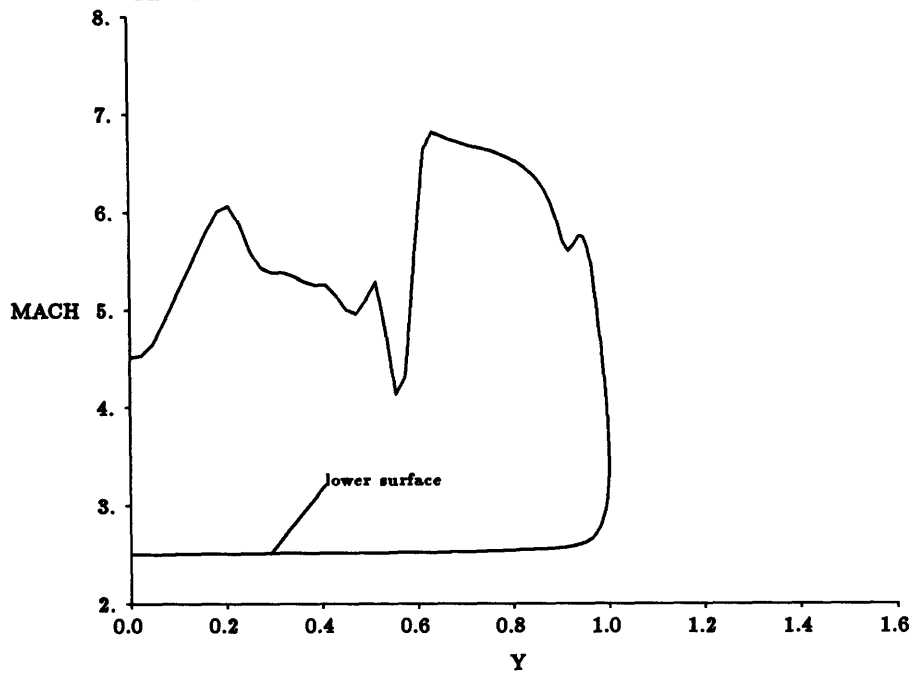Figure 5.31: Mach number on the wing surface at 50% chord

$M = 7.15, Re = \infty, \alpha = 30.0°, Grid = 33 \times 49 \times 97, X/C = 0.80$
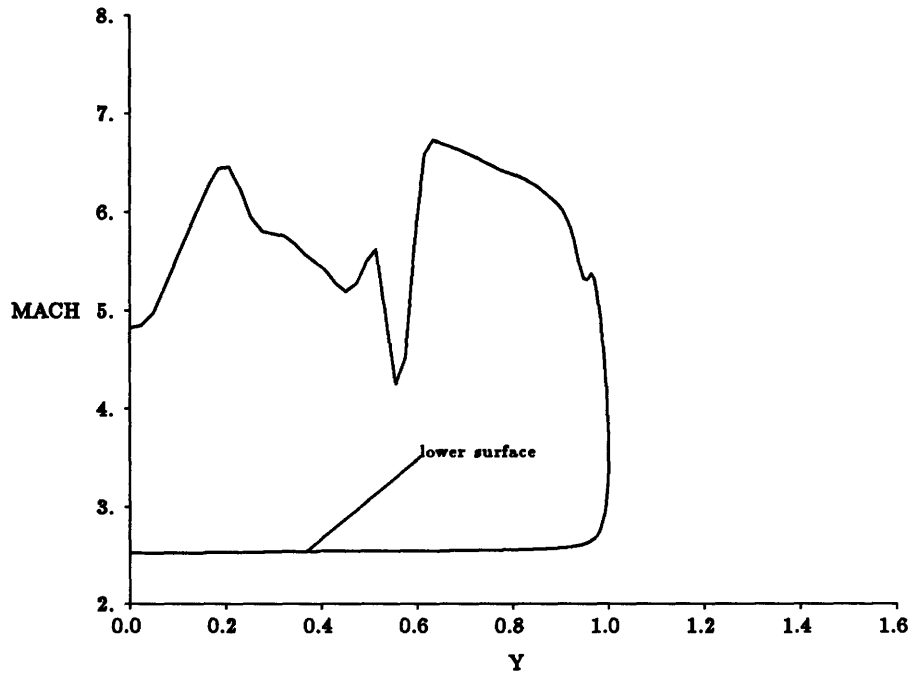MACH NUMBER ON THE BODY

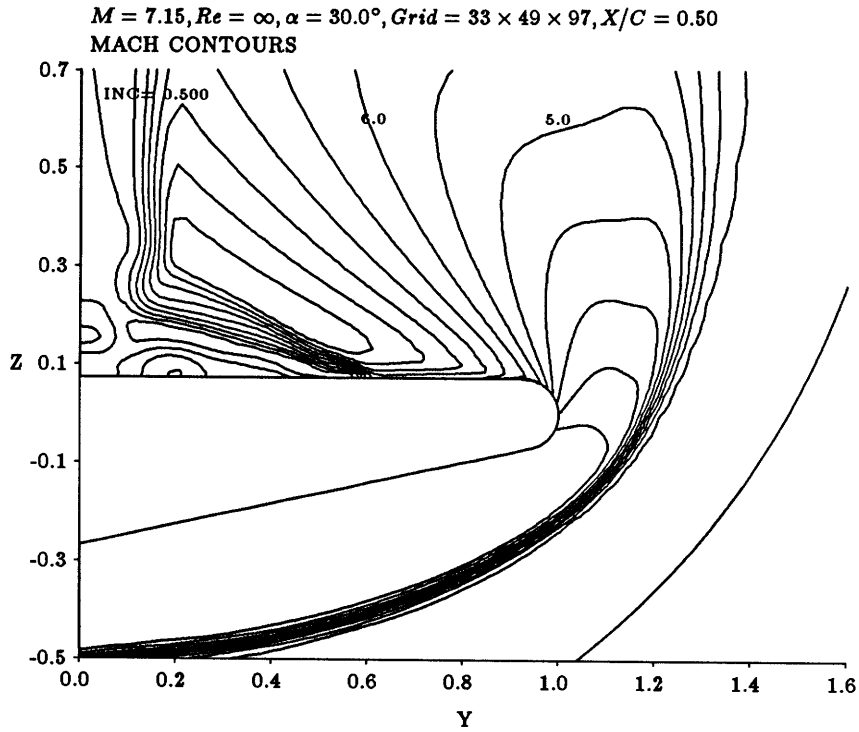

Figure 5.32: Mach number on the wing surface at 80% chord

$M = 7.15, Re = \infty, \alpha = 30.0°, Grid = 33 \times 49 \times 97, X/C = 0.50$
MACH CONTOURS

Figure 5.33: Contour plot of Mach number at 50% chord

$M = 7.15, Re = \infty, \alpha = 30.0°, Grid = 33 \times 49 \times 97, X/C = 0.50$
V-W VELOCITY VECTOR PLOT
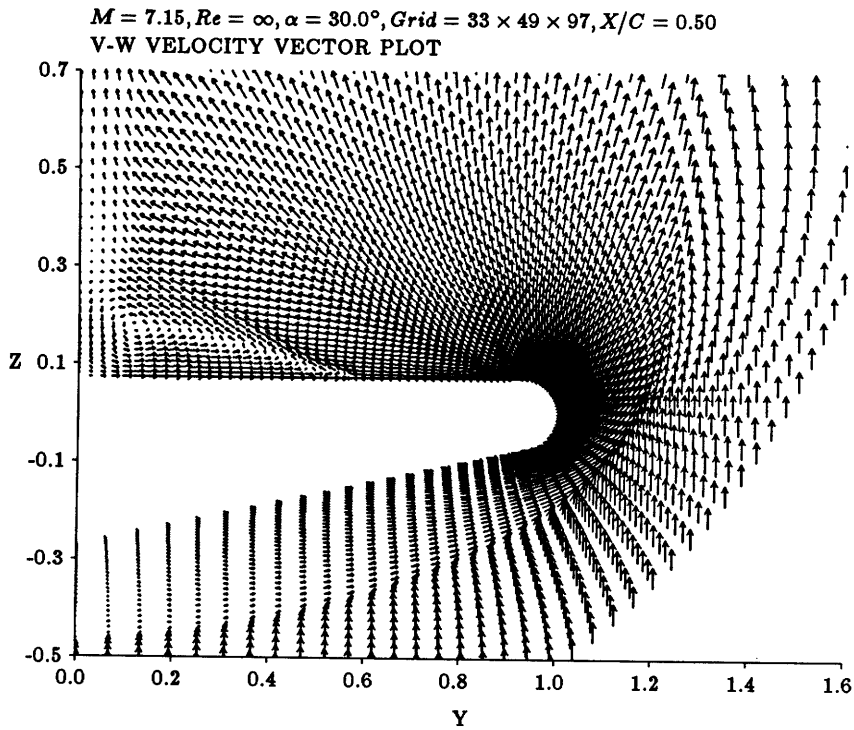
Figure 5.34: Velocity vector plot at 50% chord

77

$M = 7.15, Re = \infty, \alpha = 30.0°, Grid = 33 \times 49 \times 97, X/C = 0.80$
MACH CONTOURS
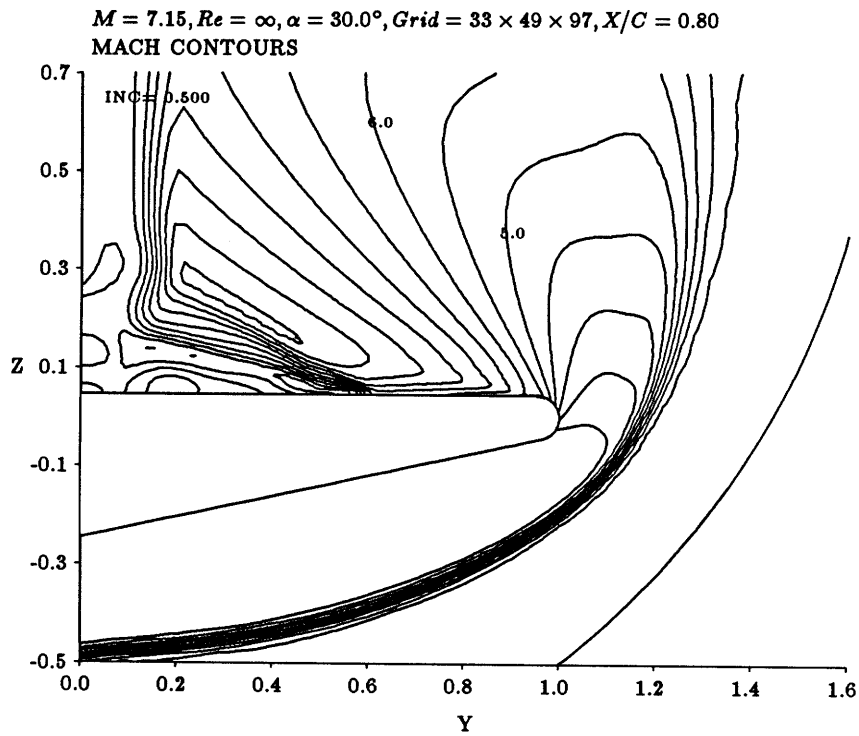
Figure 5.35: Contour plot of Mach number at 80% chord

$M = 7.15, Re = \infty, \alpha = 30.0°, Grid = 33 \times 49 \times 97, X/C = 0.80$
V-W VELOCITY VECTOR PLOT
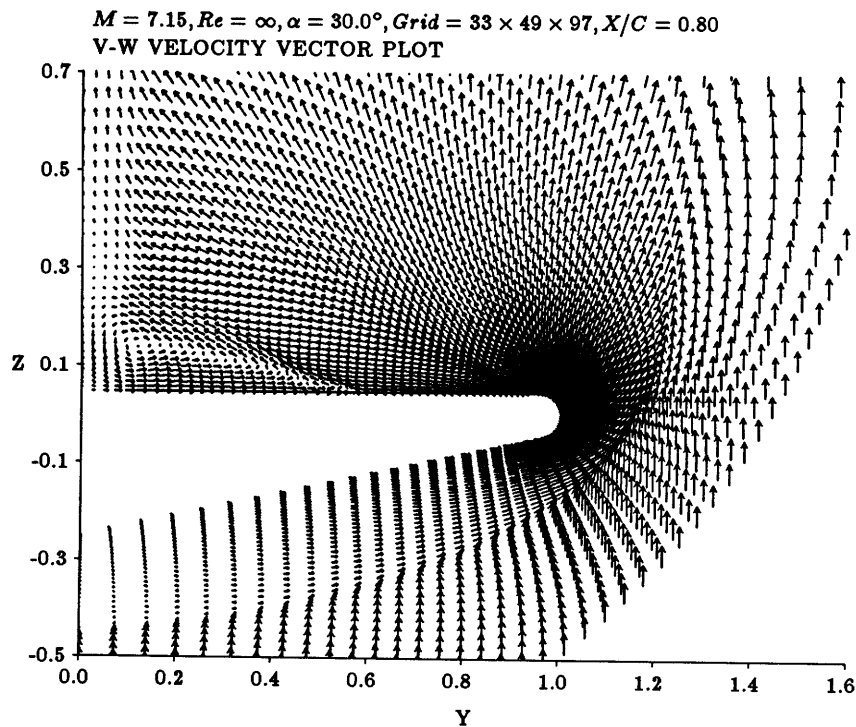
Figure 5.36: Velocity vector plot at 80% chord

$M = 7.15, Re = \infty, \alpha = 30.0^\circ, Grid = 33 \times 49 \times 97, X/C = 0.50$
CROSS-FLOW MACH CONTOURS

Figure 5.37: Cross-flow Mach number at 50% chord

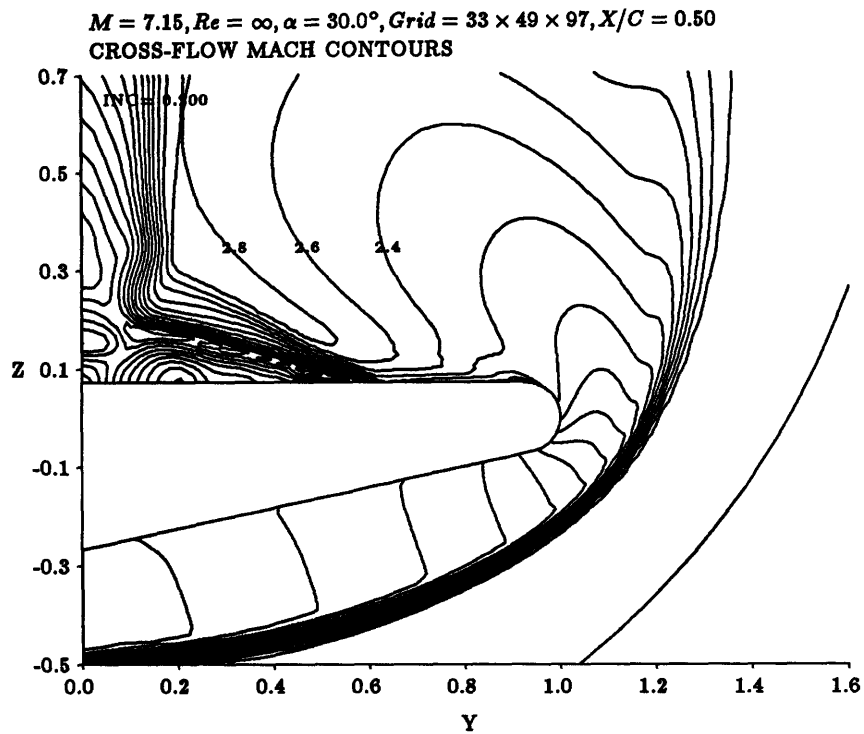$M = 7.15, Re = \infty, \alpha = 30.0^\circ, Grid = 33 \times 49 \times 97, X/C = 0.80$
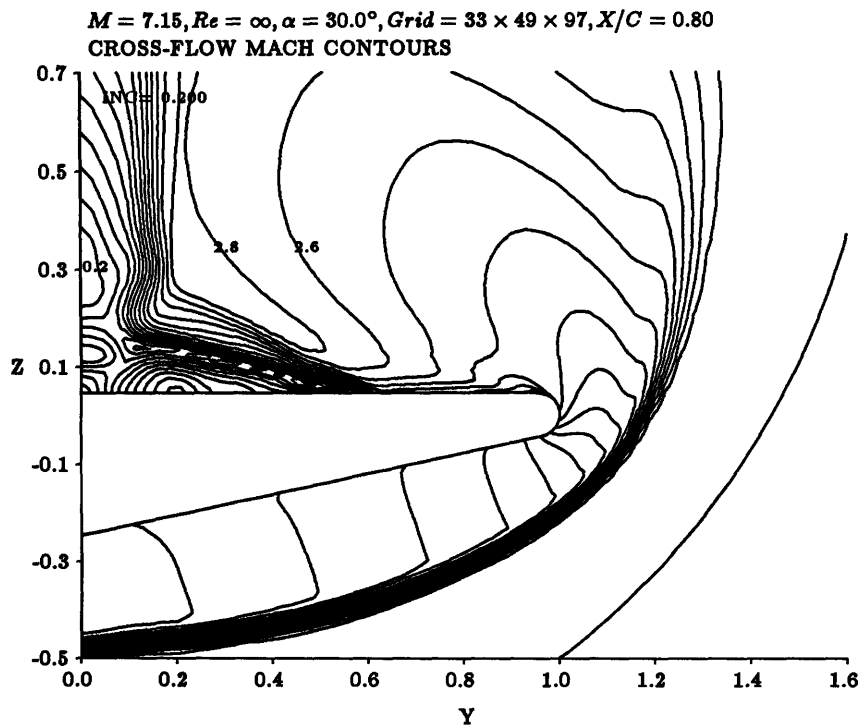CROSS-FLOW MACH CONTOURS

Figure 5.38: Cross-flow Mach number at 80% chord

79

$M = 7.15, Re = \infty, \alpha = 30.0°, Grid = 33 \times 49 \times 97, X/C = 0.50$
V-W VELOCITY VECTOR PLOT

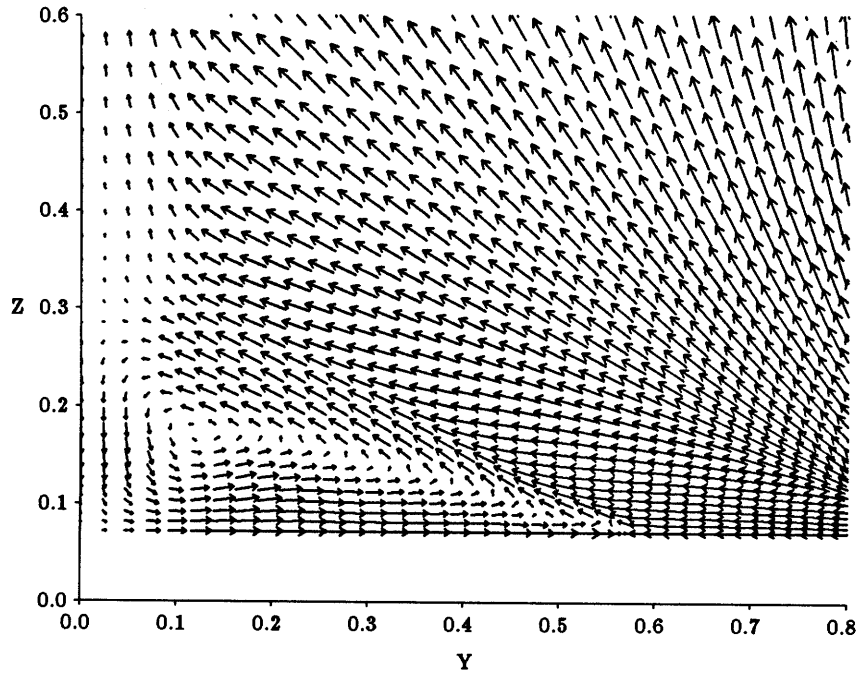Figure 5.39: Blowup of velocity vectors at 50% chord

$M = 7.15, Re = \infty, \alpha = 30.0°, Grid = 33 \times 49 \times 97, X/C = 0.80$
V-W VELOCITY VECTOR PLOT

Figure 5.40: Blowup of velocity vectors at 80% chord
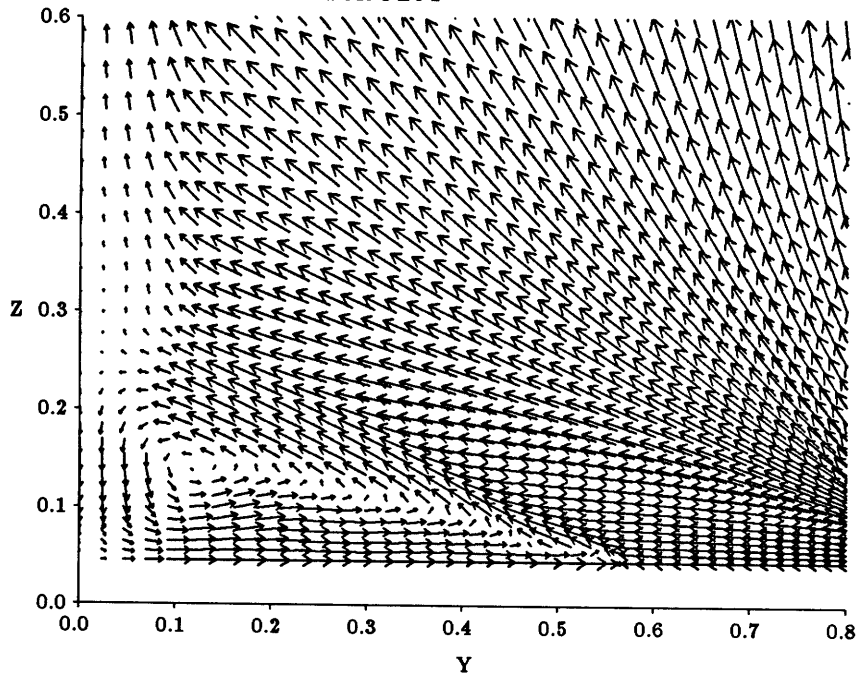
$M = 7.15, Re = \infty, \alpha = 30.0°, Grid = 33 \times 49 \times 97, X/C = 0.50$
BLOW UP OF Cp ON THE UPPER SURFACE

Figure 5.41: Blowup of C_p on the upper surface at 50% chord

$M = 7.15, Re = \infty, \alpha = 30.0°, Grid = 33 \times 49 \times 97, X/C = 0.80$
BLOW UP OF Cp ON THE UPPER SURFACE

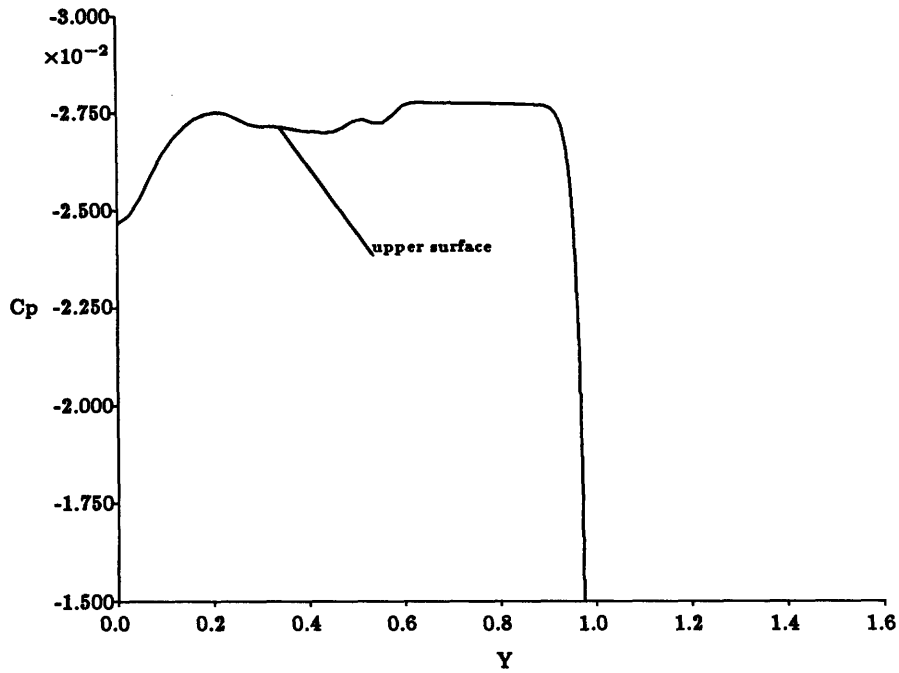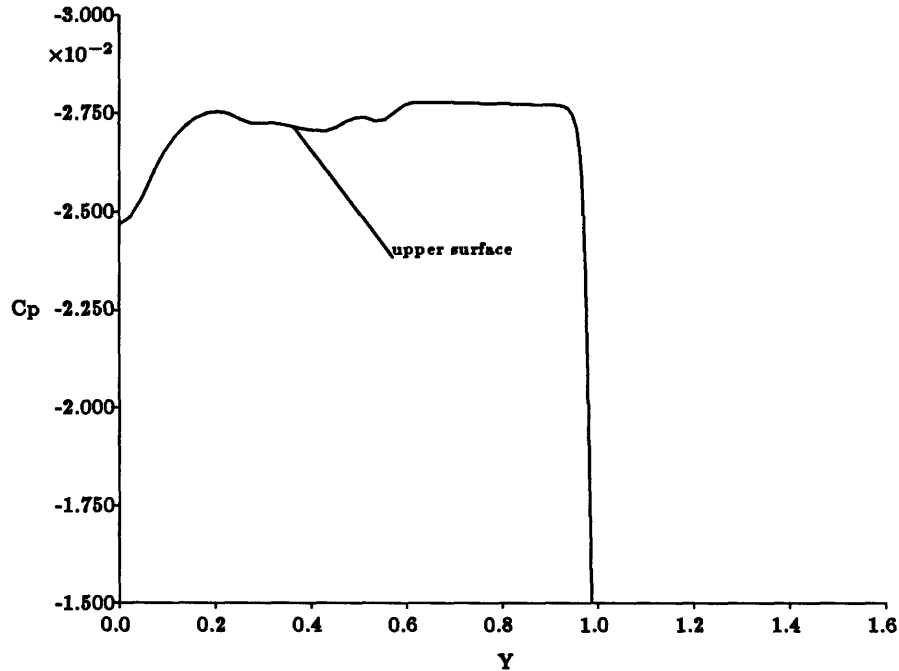Figure 5.42: Blowup of C_p on the upper surface at 80% chord

81

$M = 7.15, Re = \infty, \alpha = 30.0°, Grid = 33 \times 49 \times 97, J = 26$
XY-COMP OF MACH NUMBER CONTOURS
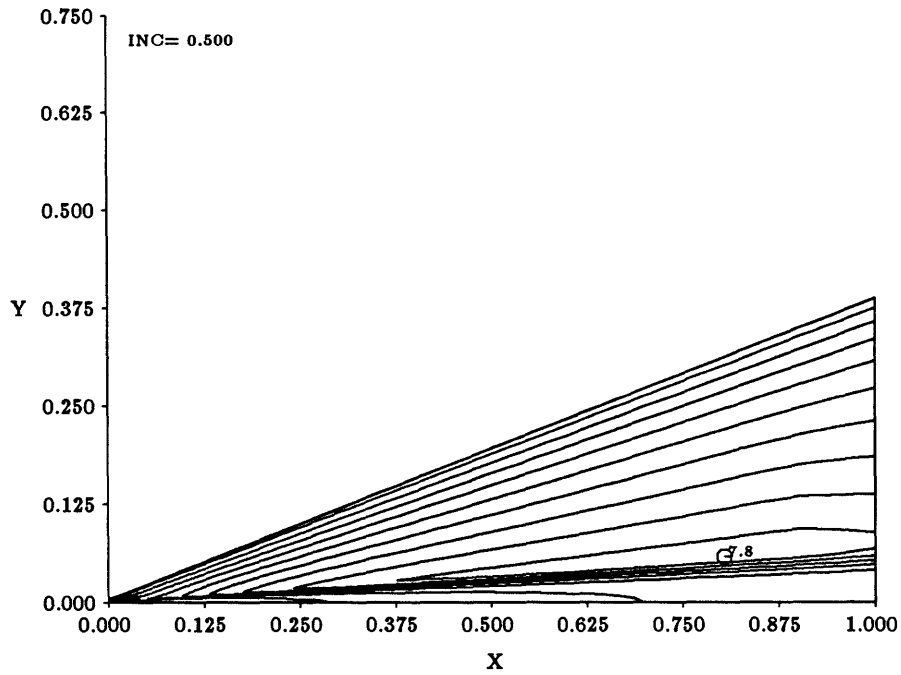
Figure 5.43: X-Y component of Mach number at station J=26

$M = 7.15, Re = \infty, \alpha = 30.0°, Grid = 33 \times 49 \times 97, J = 26$
U-V VELOCITY VECTOR PLOT
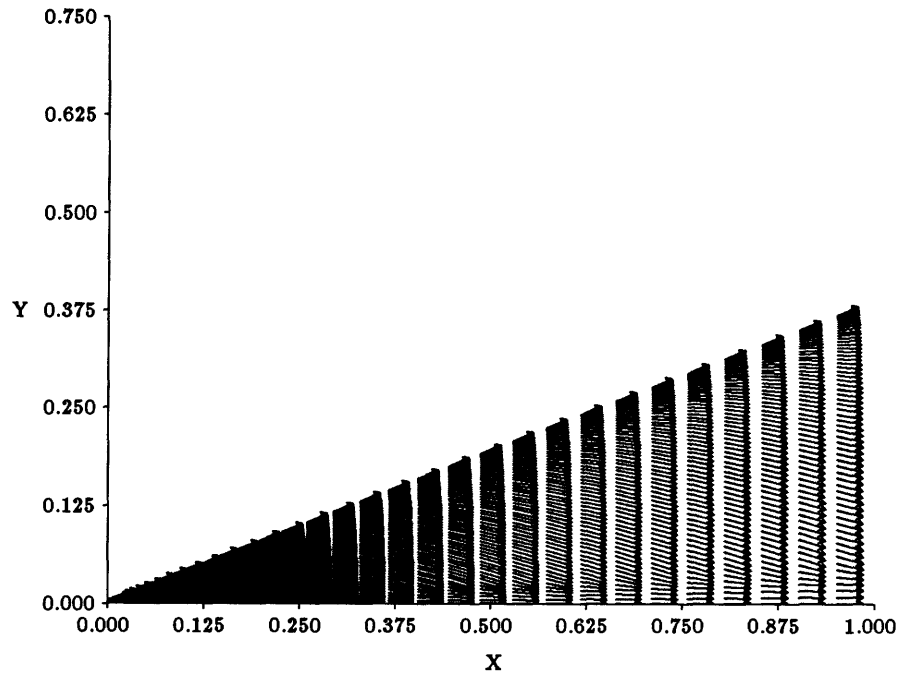
Figure 5.44: U-V component of velocity vector at station J=26

82

$M = 7.15, Re = \infty, \alpha = 30.0°, Grid = 33 \times 49 \times 97, J = 26$
TOTAL PRESSURE LOSS CONTOURS

INC= 0.500E-02
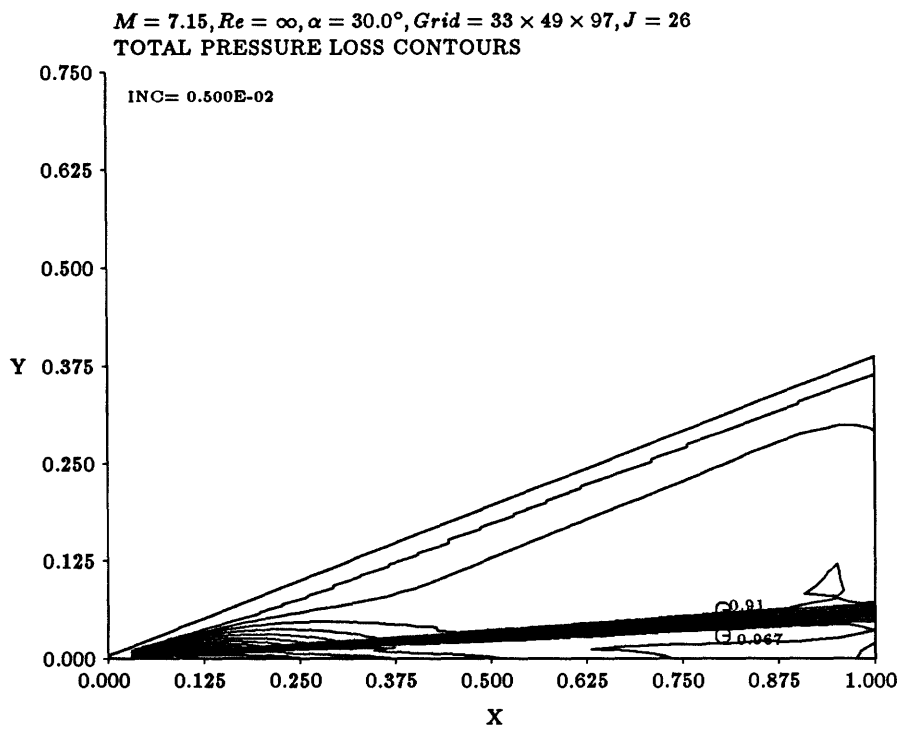
Figure 5.45: Thresholded total pressure loss at station J=26

$M = 7.15, Re = \infty, \alpha = 30.0°, Grid = 33 \times 49 \times 97, X/C = 0.50$

TOTAL PRESSURE LOSS ON THE BODY

Figure 5.46: Total pressure loss on the wing at 50% chord

$M = 7.15, Re = \infty, \alpha = 30.0°, Grid = 33 \times 49 \times 97, X/C = 0.80$

TOTAL PRESSURE LOSS ON THE BODY

Figure 5.47: Total pressure loss on wing at 80% chord

$M = 7.15, Re = \infty, \alpha = 30.0°, Grid = 33 \times 49 \times 97, X/C = 0.50$
TOTAL PRESSURE LOSS CONTOURS
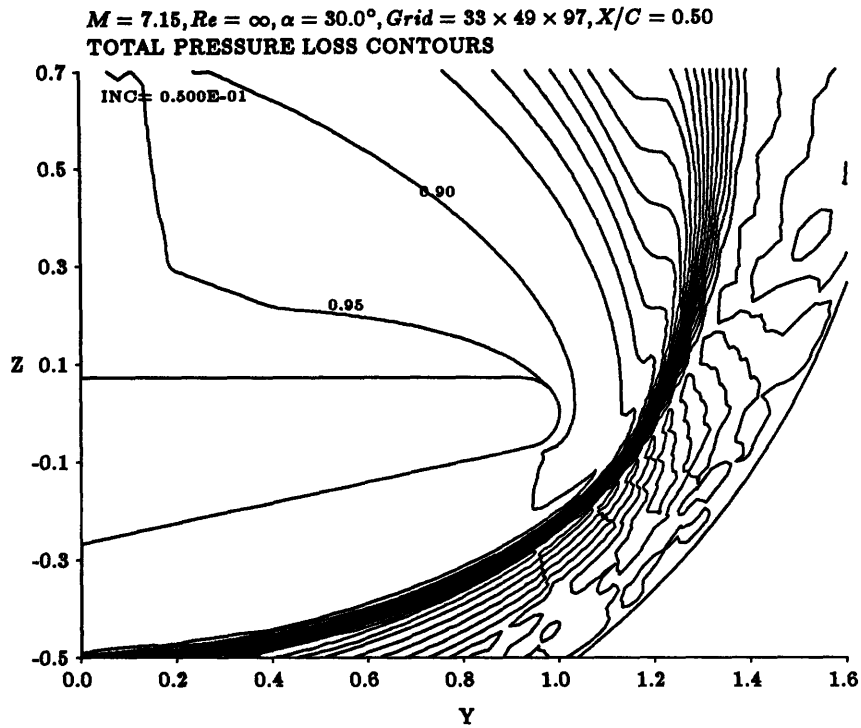
Figure 5.48: Contour plot of total pressure loss at 50% chord

$M = 7.15, Re = \infty, \alpha = 30.0°, Grid = 33 \times 49 \times 97, X/C = 0.50$
TOTAL PRESSURE LOSS ABOVE 90%
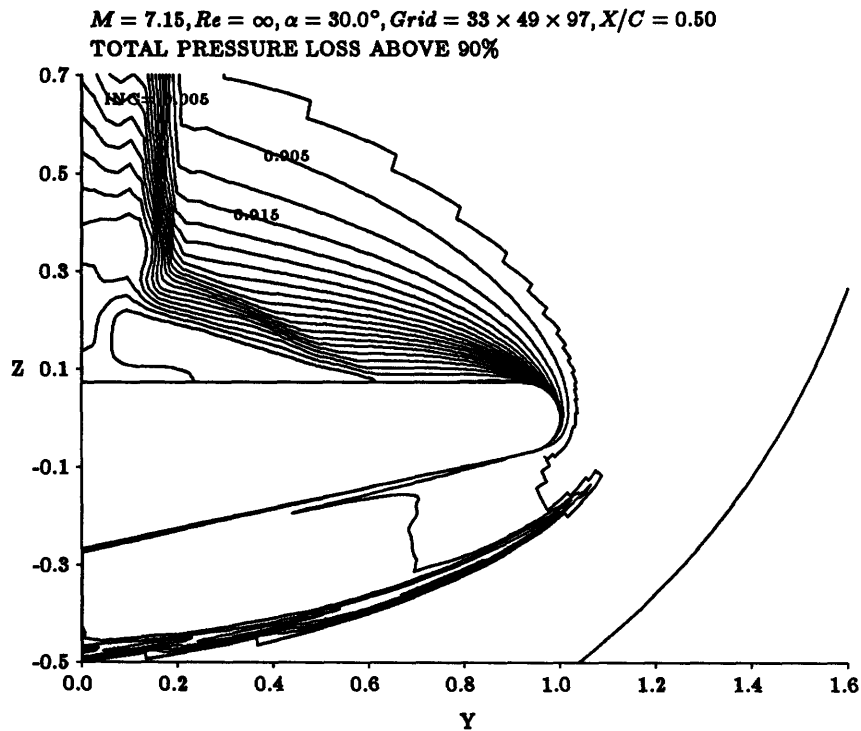
Figure 5.49: Thresholded contour plot of total pressure loss at 50% chord

85

$M = 7.15, Re = \infty, \alpha = 30.0°, Grid = 33 \times 49 \times 97, X/C = 0.80$
TOTAL PRESSURE LOSS CONTOURS
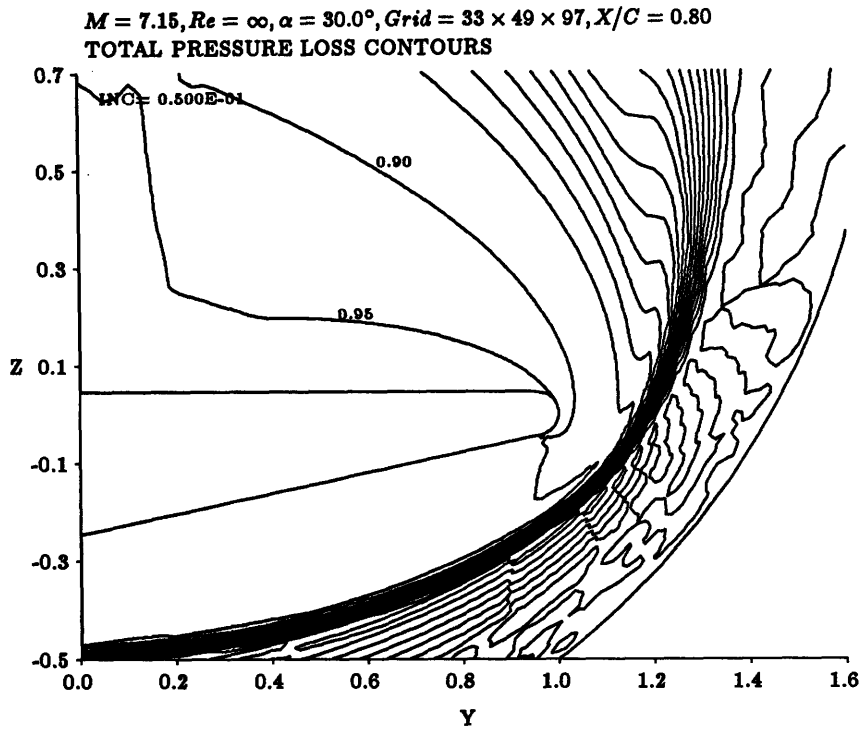
Figure 5.50: Contour plot of total pressure loss at 80% chord

$M = 7.15, Re = \infty, \alpha = 30.0°, Grid = 33 \times 49 \times 97, X/C = 0.80$
TOTAL PRESSURE LOSS ABOVE 90%
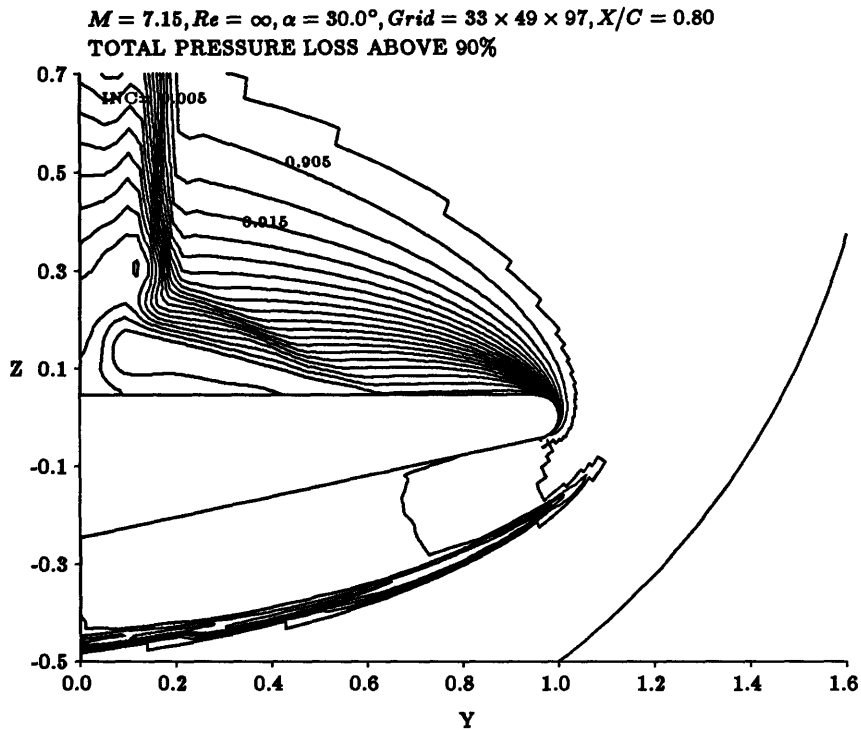
Figure 5.51: Thresholded contour plot of total pressure loss at 80% chord

$M = 7.15, Re = \infty, \alpha = 30.0°, Grid = 33 \times 49 \times 97, X/C = 0.50$
TOTAL TEMPERATURE LOSS ON BODY
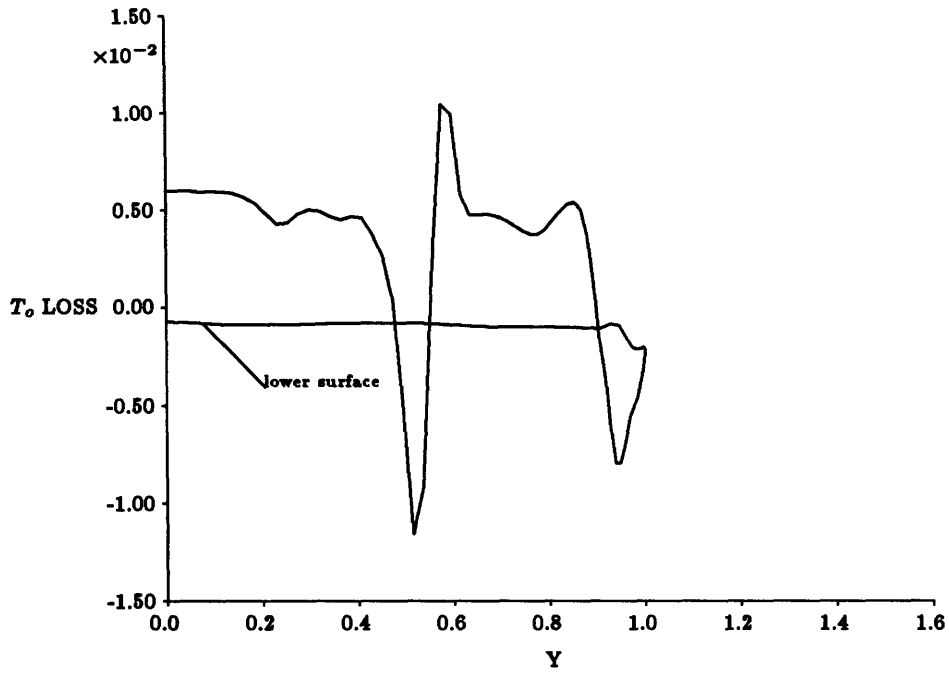
Figure 5.52: Total Temperature Loss on the Wing at 50% Chord

$M = 7.15, Re = \infty, \alpha = 30.0°, Grid = 33 \times 49 \times 97, X/C = 0.80$
TOTAL TEMPERATURE LOSS ON BODY
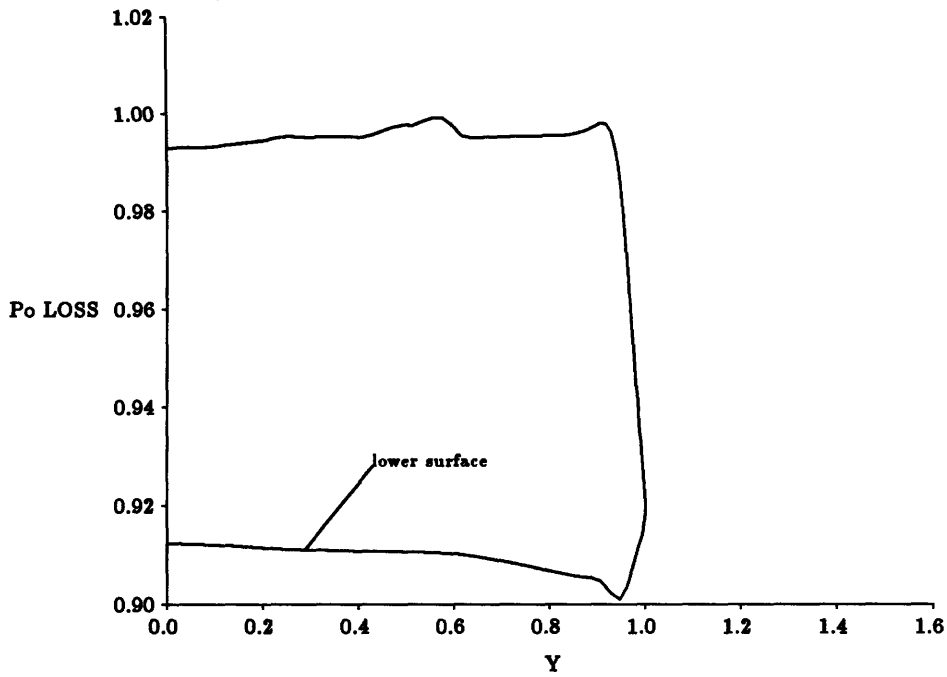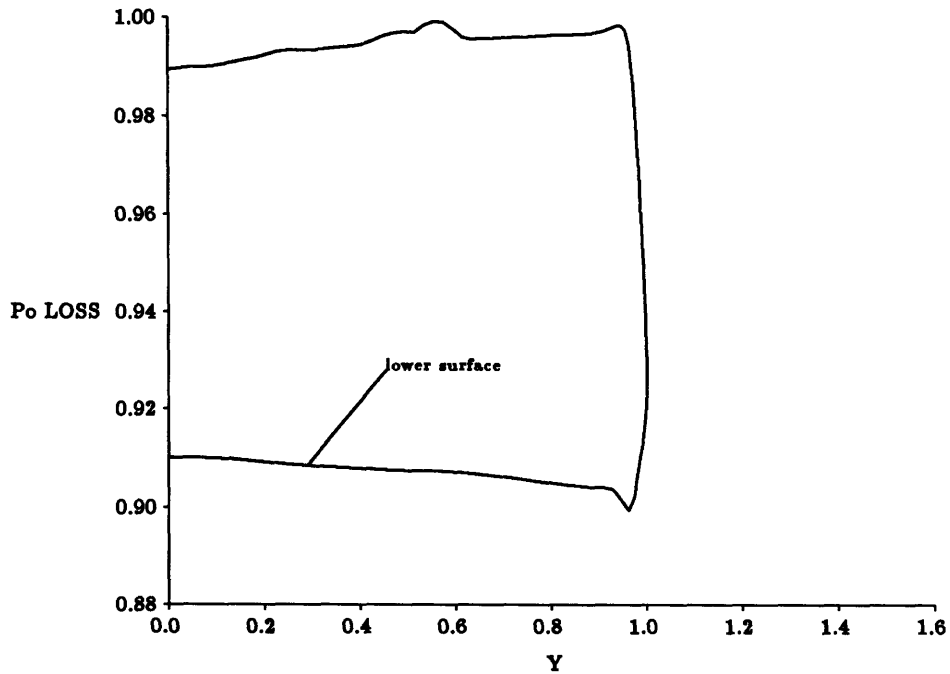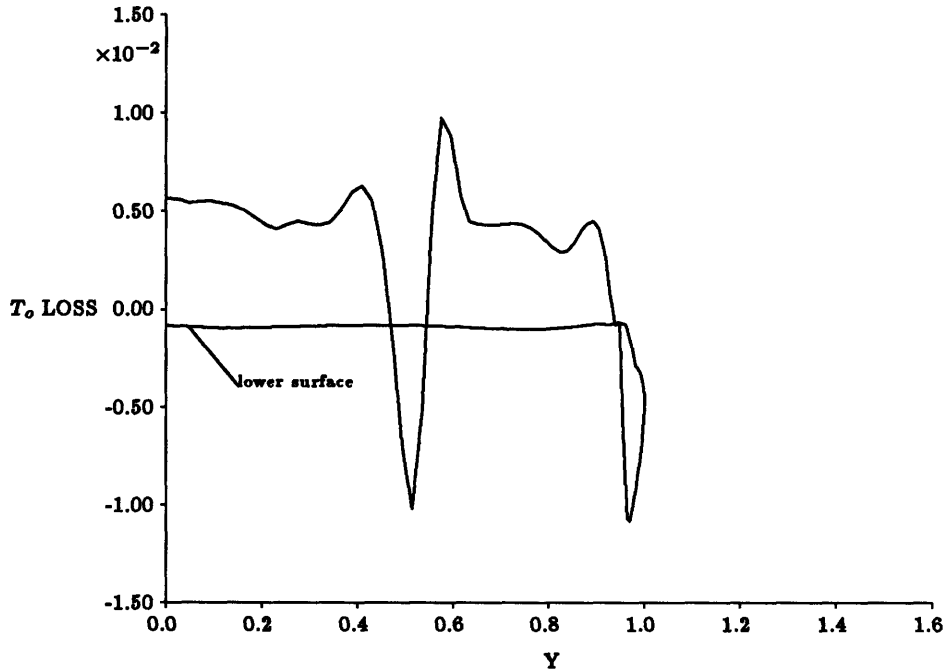
Figure 5.53: Total Temperature Loss on the Wing at 80% Chord

87

$M = 7.15, Re = \infty, \alpha = 30.0°, Grid = 33 \times 49 \times 97, X/C = 0.50$
TOTAL TEMPERATURE LOSS CONTOURS
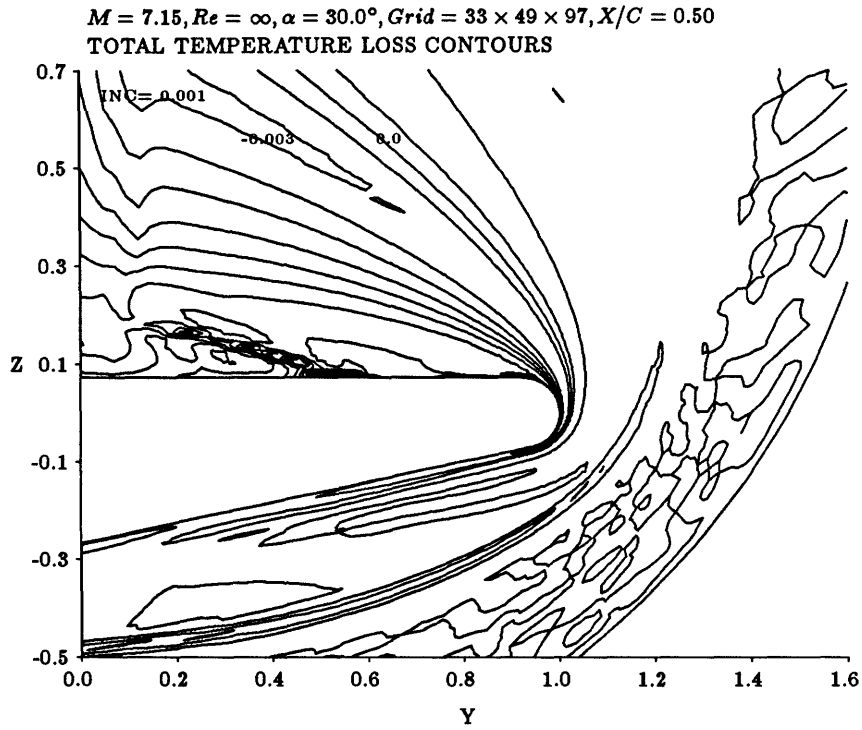
Figure 5.54: Contour Plot of Total Temperature Loss at 50% Chord

$M = 7.15, Re = \infty, \alpha = 30.0°, Grid = 33 \times 49 \times 97, X/C = 0.80$
TOTAL TEMPERATURE LOSS CONTOURS
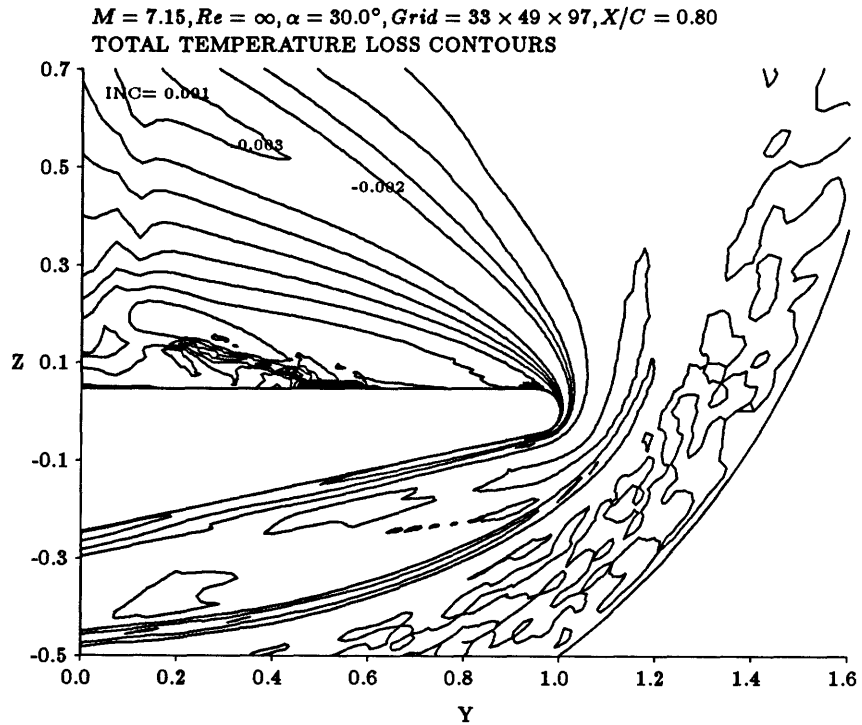
Figure 5.55: Contour Plot of Total Temperature Loss at 80% Chord

88

$M = 7.15, Re = \infty, \alpha = 30.0°, Grid = 33 \times 49 \times 97, X/C = 0.50$
VORTICITY MAGNITUDE CONTOURS
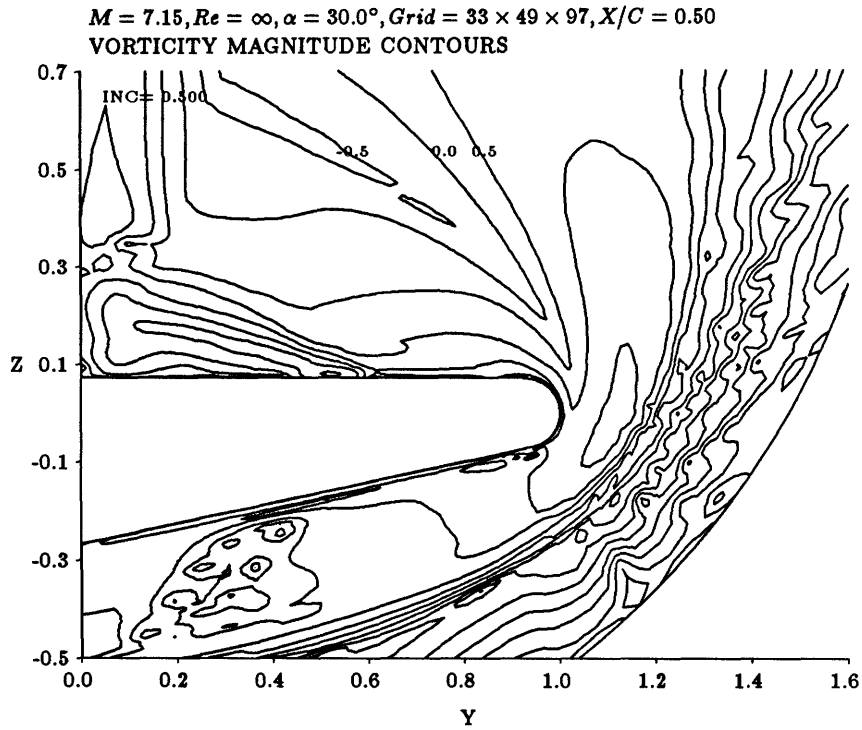
Figure 5.56: Contour Plot of Log Vorticity Magnitude at 50% Chord

$M = 7.15, Re = \infty, \alpha = 30.0°, Grid = 33 \times 49 \times 97, X/C = 0.80$
VORTICITY MAGNITUDE CONTOURS
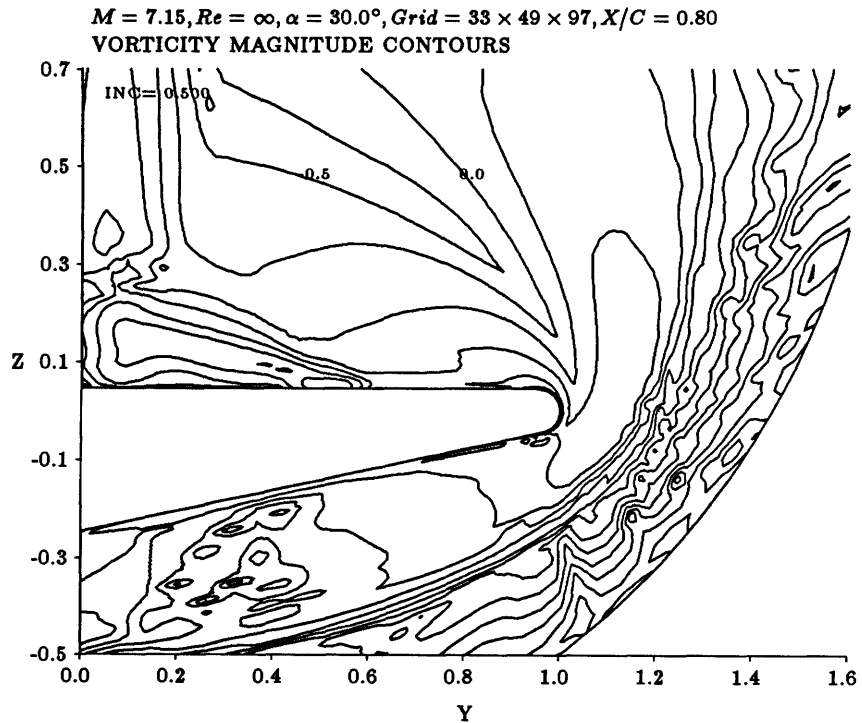
Figure 5.57: Contour Plot of Log Vorticity Magnitude at 80% Chord

89

Chapter 6

Viscous Calculations For Blunt Leading Edge

Delta Wing

This chapter presents viscous calculations at Mach 7.15, 30° angle of attack and Reynolds number of 5.85 × 10⁶. Freestream and wall temperatures are set to 74K and 288K respectively. These conditions were determined by the workshop on hypersonic flows for reentry problems co-organized by INRIA and GAMNI-SMAI. The procedure for obtaining the starting solution is spelled out in detail together with the CPU requirements. Important flow features on the top surface and in the cross-flow planes are discussed in the last section.

6.1   Solution Procedure

As in the inviscid case, initializing the flow to freestream and letting it run at the desired flight conditions will not result in a converged solution. Neither is the solution to the inviscid calculation a suitable starting point, because the no-slip condition on the wall in a viscous calculation deviates too drastically from the inviscid solution. Since the wing is not conical, a solution to the conical Navier-Stokes equation cannot be used as the starting solution as was done by [Loyd][17].

Through experiments, it was found that running in the explicit mode and using freestream conditions as a starting solution, convergence can be obtained for Mach 7.15, 0° angle of attack and Reynolds number of 5.85 × 10⁶. To obtain a solution

Figure 6.1: Coarse grid used to obtain starting solution

Figure 6.2: Starting solution rms residual history

at 30°, the angle of attack was gradually increased by intervals of 5° to 10°. The second order dissipation coefficient had to be set to a rather high value of 1.0, while the forth order dissipation coefficient can be left at 0.005. CFL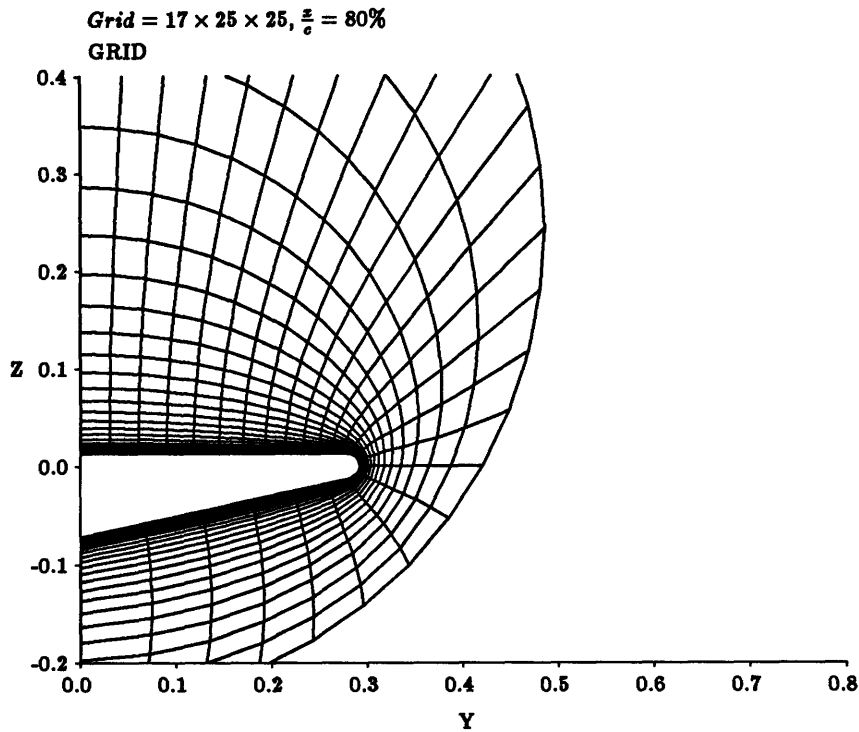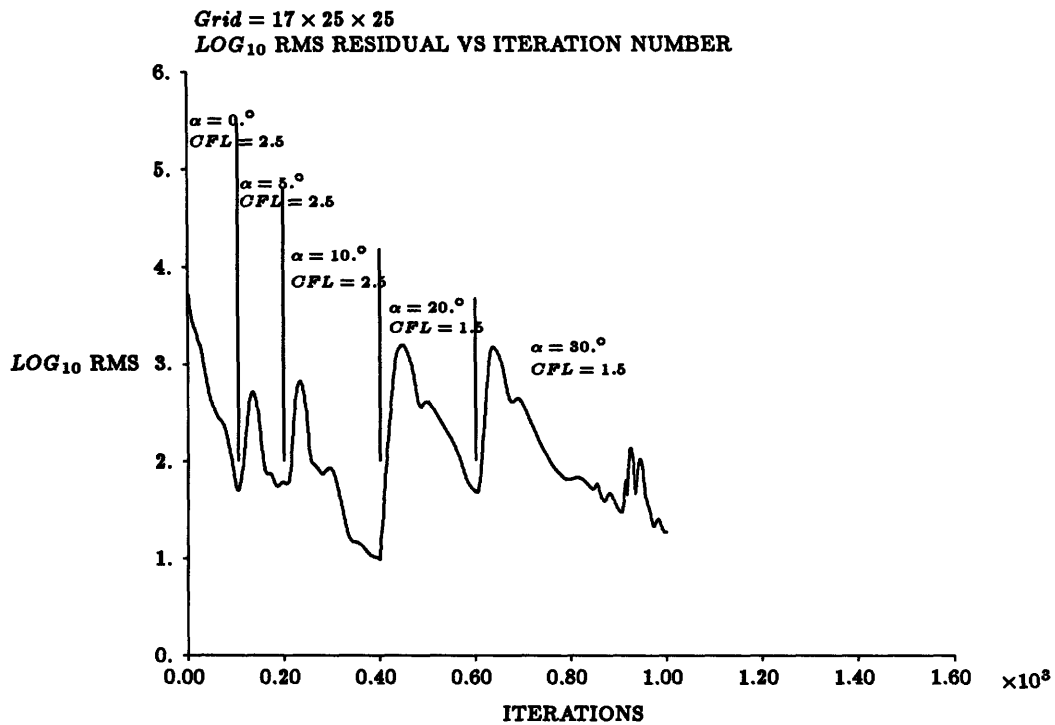 number was initially set to 2.5 but had to be decreased to 1.5 at 20° when the calculations showed signs of instability. Other parameters were set to the final desired values listed in Appendix B. The starting solution was obtained on the coarse grid shown in figure 6.1, which consists of 17 streamwise, 25 body-normal and 25 circumferential points. A plot showing the residual history for the starting solution can be found in figure 6.2. On the $AlliantFX - 3$ the calculations averaged slightly less than 10 CPU minutes per 100 iterations and the starting solution was obtained in about $1\frac{1}{2}$ hours. This starting solution was used as the input to semi-implicit calculations. The semi-implicit results were interpolated onto a finer grid consisting of 17 streamwise, 49 body-normal and 49 circumferential nodes. The solution to this medium grid was then be used to start the final calculations on the fine grid of 33 streamwise, 97 body-normal and 97 circumferential grid points shown in figures 6.3 and 6.4. A final grid of this resolution resulted in about 15 points within the boundary layer on both the upper and lower surfaces of the wing. On this grid, the semi-implicit solution takes about an hour per 100 iterations on the $Cray2$.

6.2 Convergence Criterion

The convergence criterion used is identical to that employed in the inviscid calculations. The solution was considered to be converged after the residual have dropped 3 orders of magnitude from 10^4 to 10. A plot of the residual for the final calculation on the fine grid is given in figure 6.5. The discontinuity results from changing some parameters after 1000 iterations.
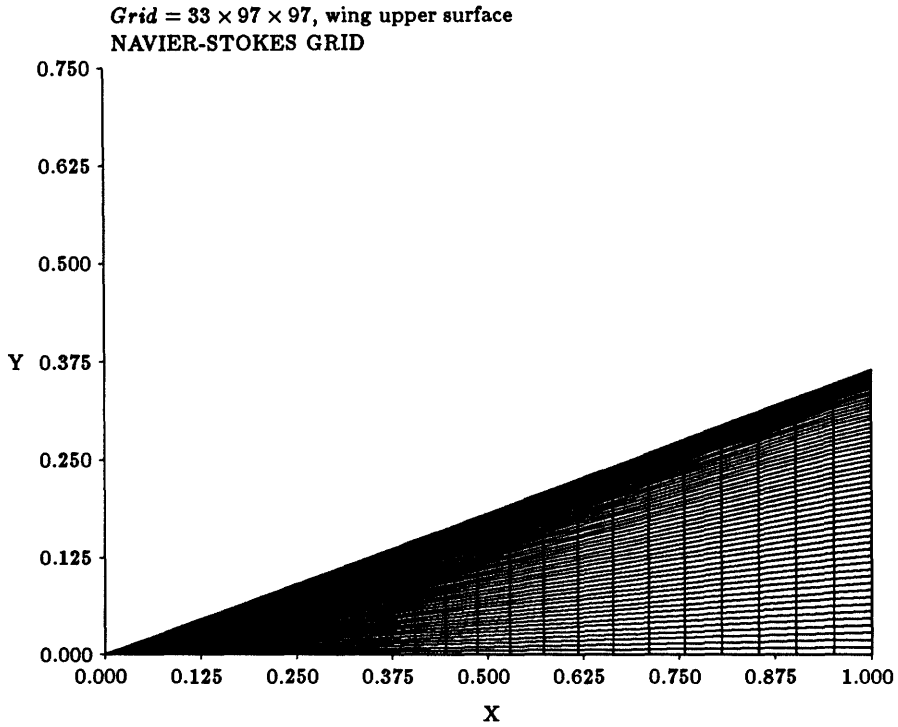
Figure 6.3: Grid used for final calculation (surface)
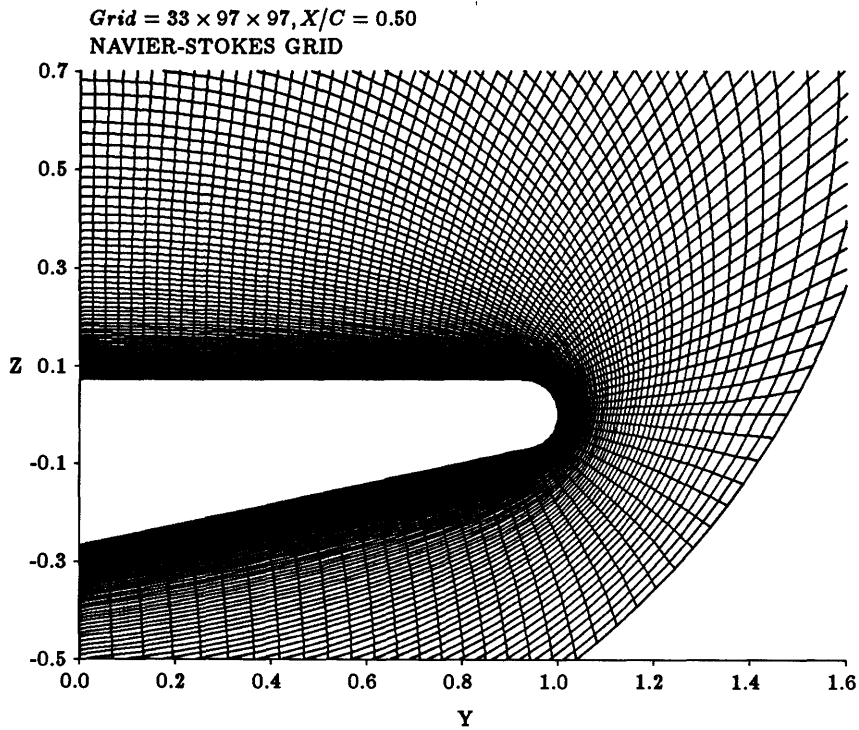
Figure 6.4: Grid used for final calculation(80% chord)

$M = 7.15, Re = 5.85 \times 10^6, \alpha = 30.0°, Grid = 33 \times 97 \times 97$

LOG RMS RESIDUAL VS ITERATION NUMBER
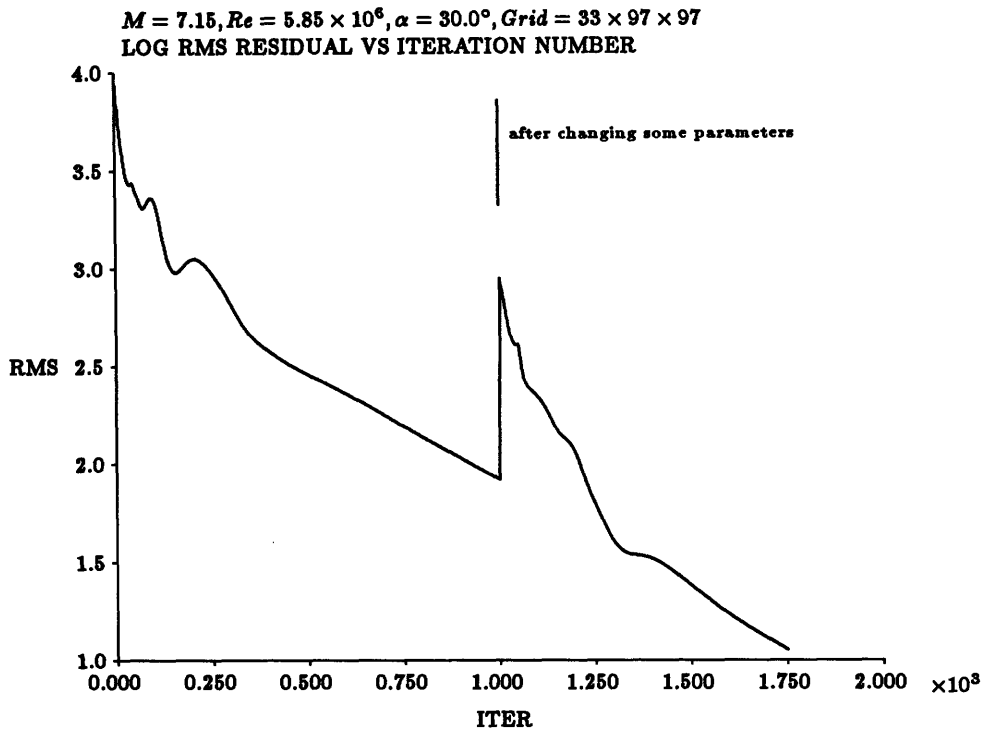
Figure 6.5: Rms residual for final calculation

6.3 Results

For the above calculation, the computed normal force coefficient is 0.6658. The streamwise tangential force coefficient has two contributions; pressure and skin friction. Pressure contributed 6.027×10^{-2} and skin friction resulted in an additional $2.705 \times 10-3$. After accounting for the 30° tilt that caused by the angle of attack, the lift and drag coefficients are 0.545 and 0.387 respectively.

Hypersonic flows are normally dominated by strong shocks and this case is no exception. At the root chord, a strong attached shock is positioned approximately 5° below the windward surface. Across the shock the values of density, Mach number and pressure change dramatically. As the flow traverses the leading, it moves into an expansion region where rapid changes occur in the circumferential direction. On the leeward surface massive separation of the flow takes place resulting in a detached shear layer pealing off at about 85% span. A vortex is trapped between this free

94

shear layer and the boundary layer on the leeward side of the wing.

In addition to inviscid non-dimensional quantities presented in the previous chapter, viscous quantities also have to be non-dimensionalized to facilitate the analysis process. These non-dimensional parameters are:

$$\vec{C_f} = \frac{\vec{\tau_w}}{\frac{1}{2}\rho_\infty u_\infty^2} \tag{6.1}$$

$$C_{f_y} = \vec{C_f} \cdot \vec{j} \tag{6.2}$$

$$St = \frac{\dot{q_w}}{\rho_\infty u_\infty C p_\infty (T_{0_\infty} - T_w)} \tag{6.3}$$

where $\vec{\tau_w}$ is the wall shear per unit area and $\dot{q_w}$ is the heat flux out of the wall per unit area and time.

6.3.1 Code Accuracy

The inviscid cone calculations in the previous chapter showed that the high second-order dissipation coefficient did not lead to substantial corruption of the inviscid result. Similarly, we can be fairly confident that the results in the regions of the flow not dominated by physical viscosity are equally well predicted. However in viscous regions, especially in the boundary layers, there is cause for concern. If the high second-order dissipation coefficient results in excessive levels of artificial viscosity in the boundary layers, then numerical dissipation may dominate physical dissipation. Physical viscous effects become overshadowed and the validity of this calculation is questionable.

To get an idea of the relative importance of the numerical and physical dissipation, it is helpful to examine the flux contributions of the artificial and numerical viscosity components going in and out of a cell. The contribution of the artificial viscosity component is given by the dissipation operator **D** in equation 3.2, and the

physical viscosity component can be calculated from the viscous component of the flux residual R in equation 3.10.

Figures 6.6 to 6.11 show plots of the ratio $Log_{10} \frac{D}{R_{vis}}$ and the grid structure at three closeup locations near the wing surface. Approximately 15 grid points are embedded within the boundary layer, so the 15th station away from the body will be used as an estimate of the limit of the boundary layer. For convenience, it is sufficient to examine only the dissipation ratio of the streamwise x-momentum equation. Since the ratio changes exponentially, a logarithmic scale is used.

On the windward surface (figures 6.6 and 6.7), the ratio is small but rises rapidly. Within the first 10 cells, the dissipation ratio is less than 0.1, but by the 15th cell, the numerical and physical dissipation are of comparable magnitude. This result is acceptable since viscous effects start to become less important at the edge of the boundary layer, and convection effects begin to dominate. At the leading edge (figures 6.8 and 6.9), the dissipation ratio is small even at the edge of the boundary layer. By the 15th cell away from the body, the numerical dissipation is still less that one tenth the value of the physical dissipation. This result is encouraging and indicates that the high second-order dissipation coefficient has not resulted in excessively high artificial viscosity within the boundary layer. On the leeward surface the results are even better. At the edge of the 'boundary layer', the dissipation ratio is less than 10^{-2}, and drops exponentially nearer the body.

While the above observations do not confirm the validity of this numerical simulation, they do clear up doubts about the magnitude of the numerical dissipation near the wing surface, and the possibility of corruption resulting from excessive dissipation. We can conclude that high second-order dissipation coefficient while not ideal, is acceptable for this calculation.

$M = 7.15, Re = 5.85 \times 10^6, \alpha = 30.0°, Grid = 33 \times 97 \times 97, X/C = 0.80$
X-DISSIPATION CONTOURS ON WINDWARD SURFACE
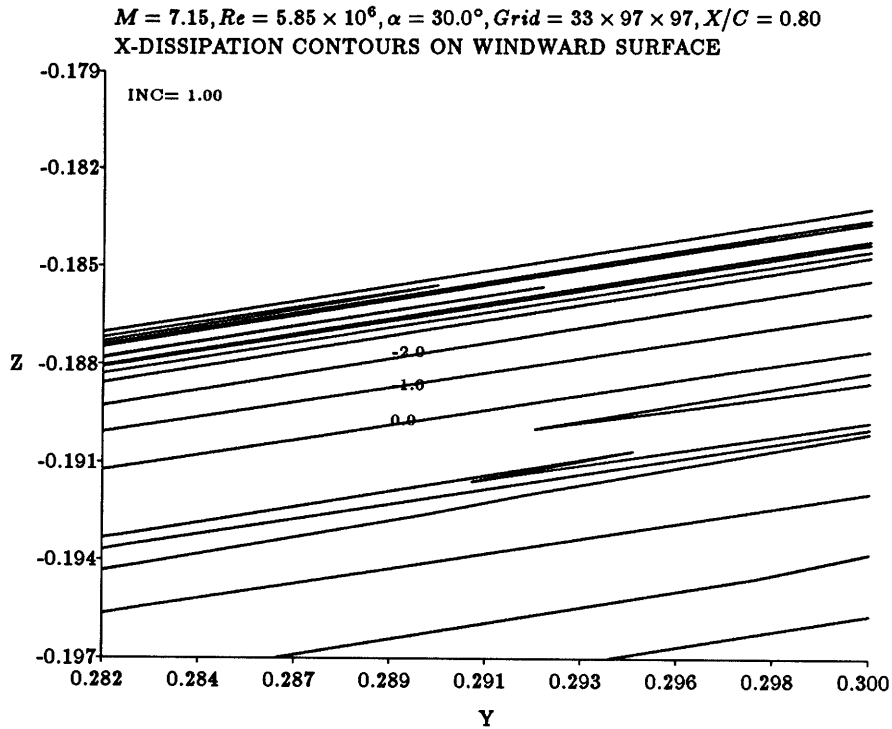
Figure 6.6: $Log_{10} \dfrac{D}{R_{vis}}$ on the windward surface

$M = 7.15, Re = 5.85 \times 10^6, \alpha = 30.0°, Grid = 33 \times 97 \times 97, X/C = 0.80$
GRID
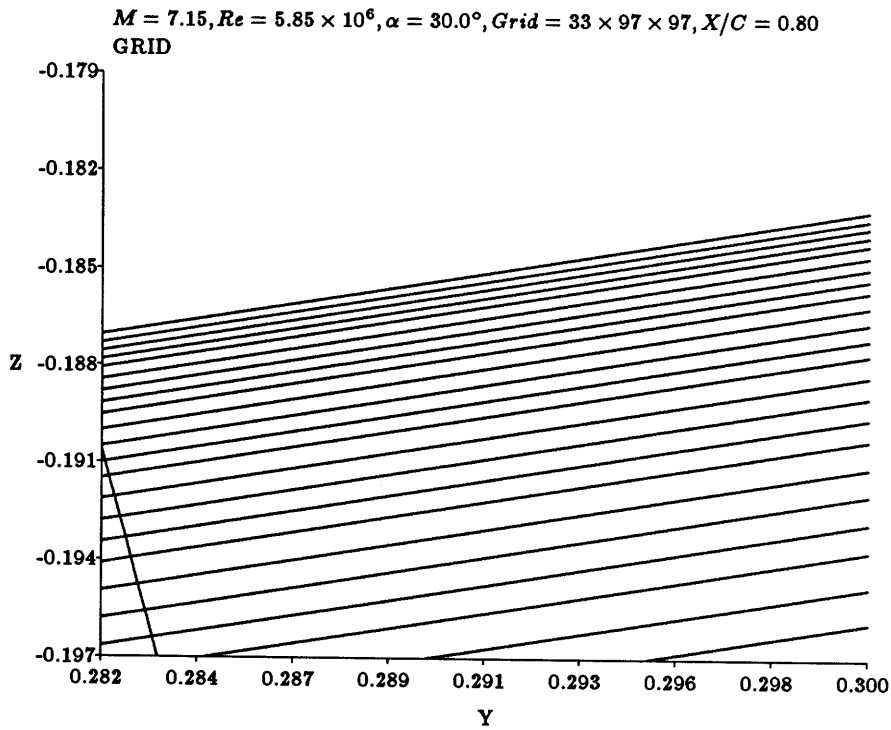
Figure 6.7: Close-up of grid on the windward surface

$M = 7.15, Re = 5.85 \times 10^6, \alpha = 30.0°, Grid = 33 \times 97 \times 97, X/C = 0.80$
X-DISSIP CONTOURS AT THE LEADING EDGE

Figure 6.8: $Log_{10} \dfrac{D}{R_{vis}}$ at the leading edge

$M = 7.15, Re = 5.85 \times 10^6, \alpha = 30.0°, Grid = 33 \times 97 \times 97, X/C = 0.80$
GRID

Figure 6.9: Close-up of grid at the leading edge

98

$M = 7.15, Re = 5.85 \times 10^6, \alpha = 30.0°, Grid = 33 \times 97 \times 97, X/C = 0.80$
X-DISSIP CONTOURS ON THE LEEWARD SURFACE

Figure 6.10: $Log_{10} \dfrac{D}{R_{vis}}$ on the leeward surface
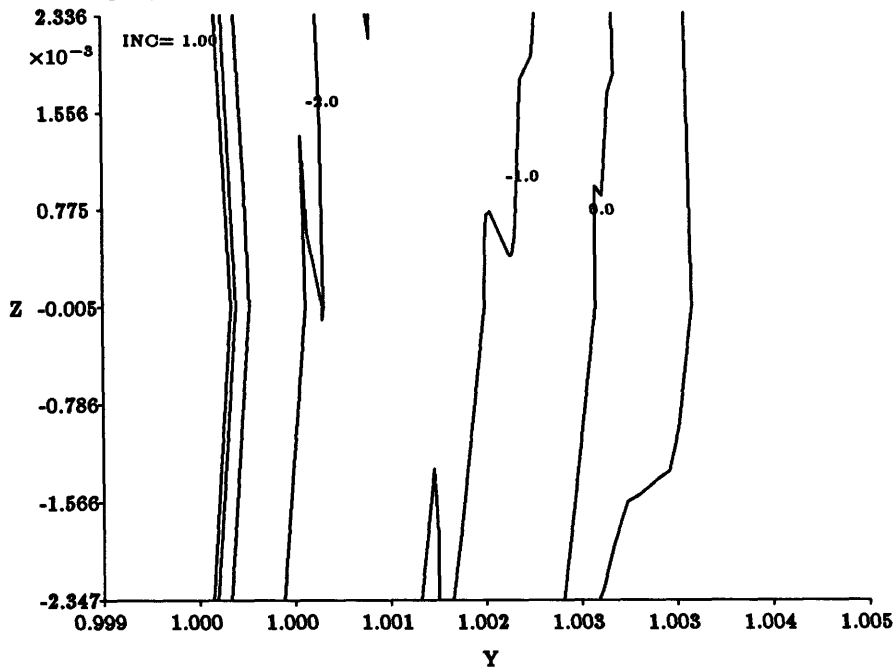
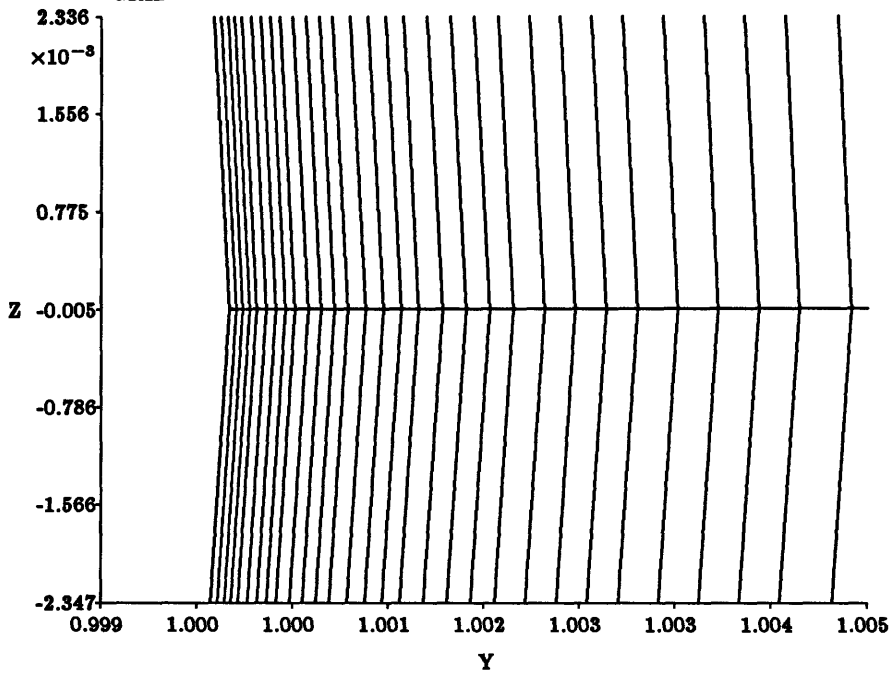$M = 7.15, Re = 5.85 \times 10^6, \alpha = 30.0°, Grid = 33 \times 97 \times 97, X/C = 0.80$
GRID

Figure 6.11: Close-up of grid on the leeward surface
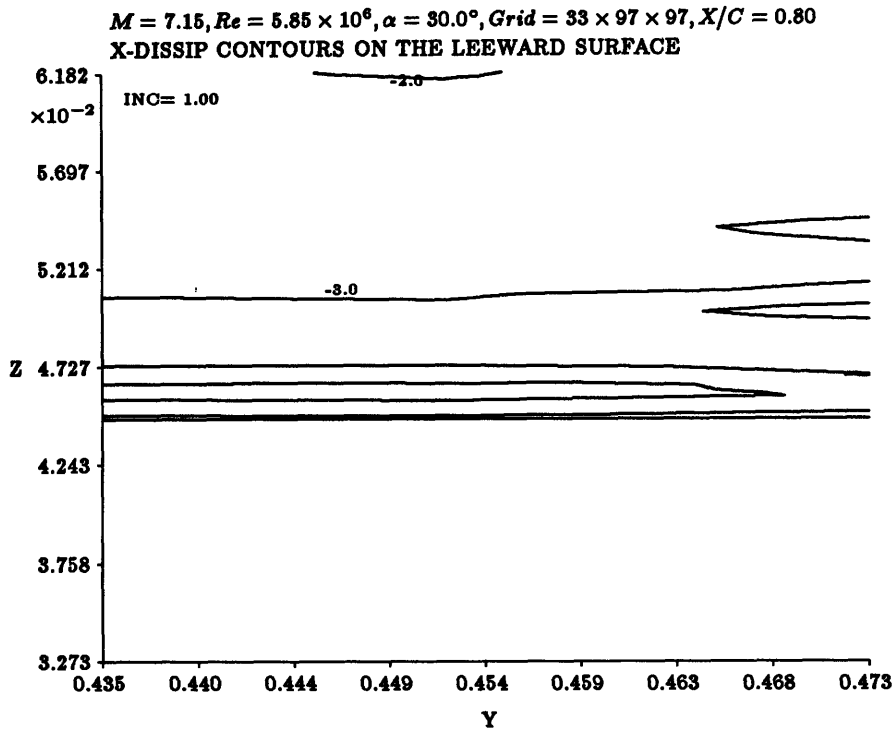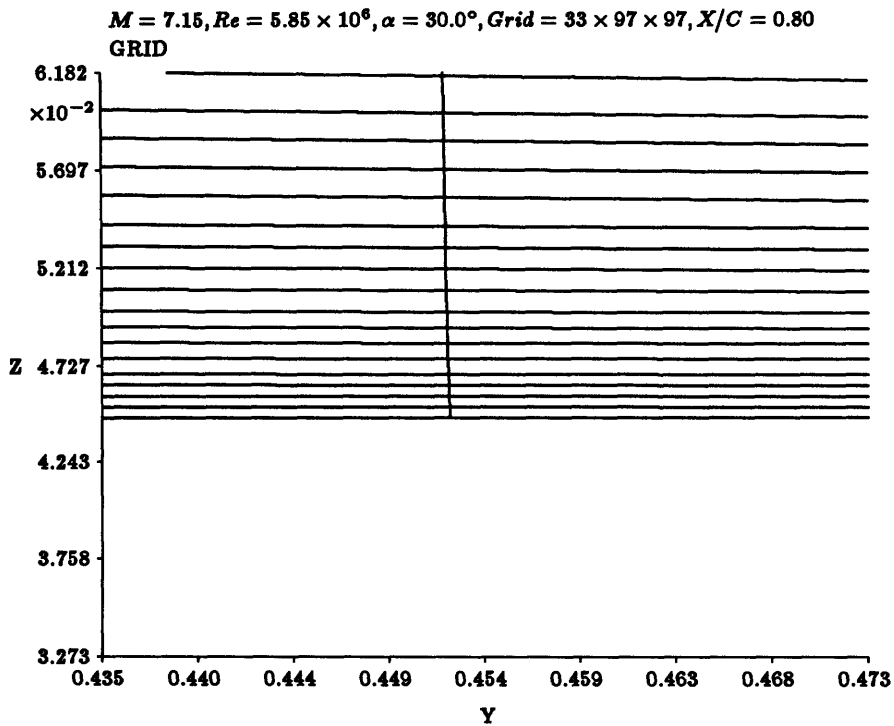
99

6.3.2 Flow Features on the Upper Surface

The apparently featureless profiles of density and pressure on the upper surface (figures 6.12 and 6.13) are deceiving in their simplicity. The most prominent feature is a thin region of rapid change near the leading edge. The width of this region remains roughly constant throughout the chord and a close comparison with the grid reveals that the start of this region coincides with the rounding at the leading edge. Density on the upper surface is fairly constant, averaging about 0.012 of the freestream value. The pressure coefficient displays a similar behavior with an average value of about -0.02. As before, it would be unwise to jump to any conclusions about the presence or absence of shocks. The pressure on the leeward surface is such a small percentage of the freestream value that a significant change in static pressure across the shock will only appear as a small change in the pressure coefficient.

Skin friction lines on the upper surface are shown in figure 6.14. Lines tend to converge in regions of flow separation and the plot indicates one primary and at least one secondary separation zone. The primary separation region is located near the leading edge and the secondary separation line is located further inboard.

Stanton number contours are presented in figure 6.15. The large variation over the surface makes it necessary to present this plot in a logarithmic scale. Results show that the highest heat transfer occurs at the apex and the leading edge whereas very small values are observed over most of the leeward surface.

Mach = 7.15, α = 30°, *Re* = 5.85 × 10^6, *Grid* = 33 × 97 × 97, wing upper surface
DENSITY CONTOURS

INC= 0.100E+00
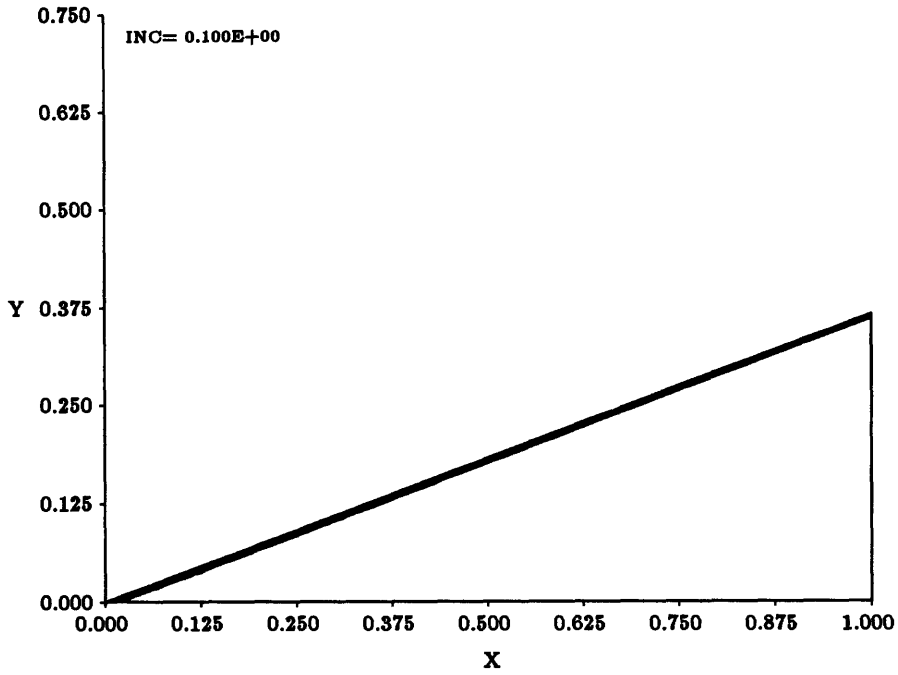
Figure 6.12: Contour plot of density on wing upper surface

M = 7.15, α = 30°, *Re* = 5.85 × 10^6, *Grid* = 33 × 97 × 97, wing upper surface
C_p

INC= 0.200E-01
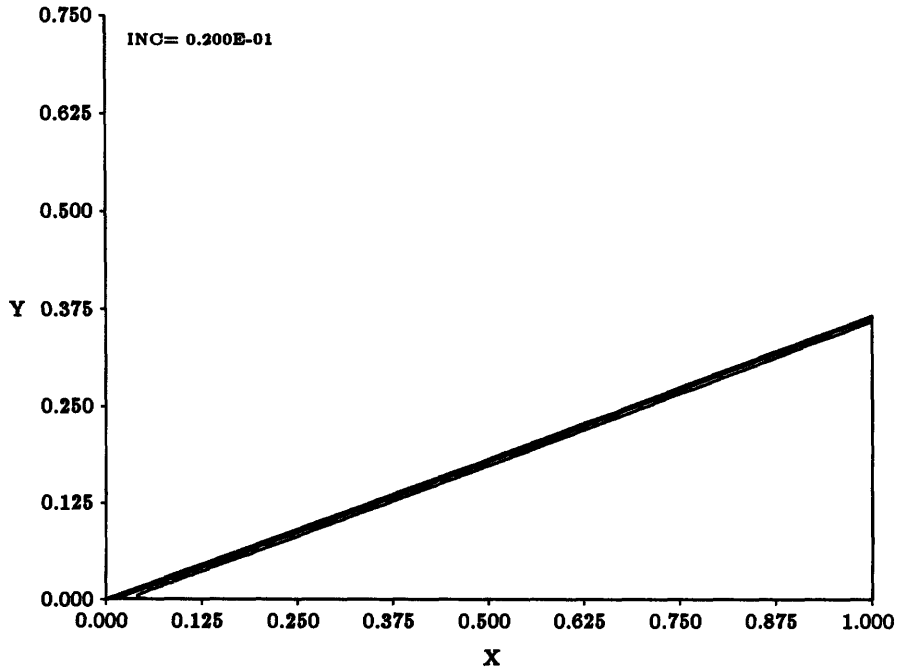
Figure 6.13: Contour plot of C_p on wing upper surface

101

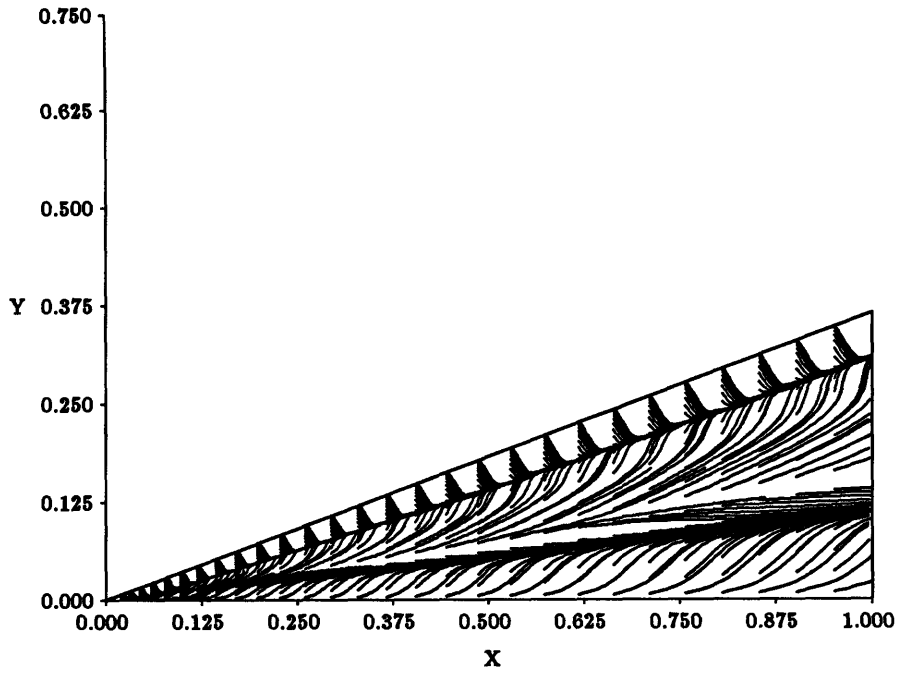$M = 7.15, Re = 5.85 \times 10^6, \alpha = 30.0°, Grid = 33 \times 97 \times 97,$Wing Surface
C_f LINES

Figure 6.14: Skin friction lines on wing upper surface

$M = 7.15, Re = 5.85 \times 10^6, \alpha = 30.0°, Grid = 33 \times 97 \times 97,$wing upper surface
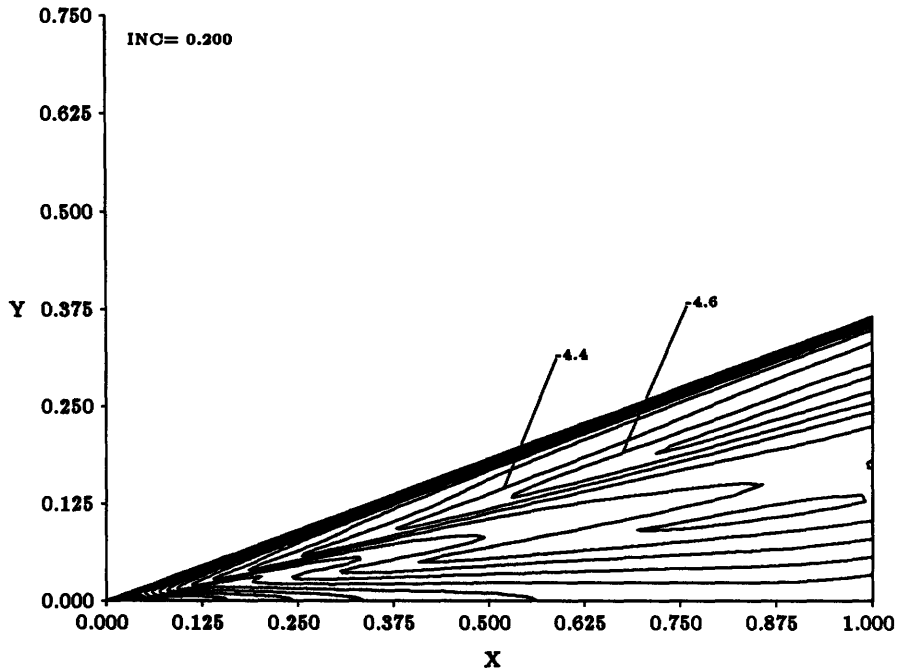Log St Number

INC= 0.200

Figure 6.15: Log of the Stanton number magnitude on wing upper surface

6.3.3 Flow Features at 50% and 80% Chord

To get a better insight into the structure of the flowfield it is imperative that we examine cross-flow plots. Plots of surface values in the cross-flow plane can give detailed information on the distribution, while contour and vector plots highlight features of the flow imperceptible from surface quantities. Close examination of these plots will reveal evidence of the dominant flow mechanisms and the primary causes of the flow separation seen earlier.

From a cursory examination of plots at the 50% and 80% chord locations, the flow appears conical, but we know from previous observation of the upper surface plots that this is not so. The expansion region near the leading edge remains the same size even though the wing is changing in dimensions. The skin friction lines in figure 6.14 demonstrates conclusively the non-conical nature of the flow over this wing.

The position of the shock is unmistakable all contour plots. As the shock rounds the leading edge into the expansion region it weakens and eventually diffuses into an expansion fan. The structure of this shock can be seen in the density contour plots in figures 6.18 and 6.19. The plots of surface and contour values of density at 50% and 80% chord are presented in figures 6.16 to 6.19. They show no significant differences in the flow structure between the 50% and 80% chord locations. Across the shock, the normalized density jumps from 1.0 to about 4.7 where it stays fairly constant. This constant density region fills most of the space between the shock and the lower surface of the body, but excludes the boundary layer where normalized density increases to about 5.8. This rise in density is the result of cooling on the wall. Plots of Stanton number of the wing surface in figures 6.41 and 6.42 will reveal that substantial cooling takes place here. Moving in the circumferential direction, the most significant change occurs at the leading edge where a strong expansion takes place. The diffusion is rapid and drastic, occurring within the outer 15% of

the span, with density dropping from about 5.8 to 0.01.

Since flow separation is strongly influenced by pressure gradients, it is informative to examine pressure coefficient and velocity vector plots simultaneously. Crossflow velocity vector and surface pressure coefficient plots are shown in figures 6.20 to 6.29. The pressure coefficient is calculated by taking the difference between the local and freestream pressures. In regions of low pressure, this difference approaches the negative of the freestream pressure and local pressure gradients are deemphasized. Such a situation is encountered on the leeward surface of the wing. To observe the changes in pressure the C_p plots on the surface are blown up in figures 6.27 and 6.29. These plots demonstrate clearly the dependence of boundary layer flow on the tangential pressure gradients. In the expansion region at the leading edge, the velocity profile gets fuller as it is accelerated by the negative pressure gradient. The effect of this is so strong that velocity overshoots occur within the boundary layer velocity profile. Figures 6.21 and 6.24 show this effect very clearly. Near the symmetry plane on the upper surface the direction of flow also coincides with a negative pressure gradient and full velocity profiles are clearly visible from figures 6.22 and 6.25. Inflected velocity profiles near separation points are observed in regions of positive pressure gradients. As the flow passes the leading edge, it encounters an unfavorable pressure gradient on the leeward surface. The velocity profile quickly becomes inflected and eventually separates at about 80% span. The secondary separation point at about 35% span on this surface also coincides with an unfavorable pressure gradient.

Besides indicating the location of the primary shock and expansion, the pressure coefficient and total pressure loss contour plots do not yield very much additional information. The surface cross-sectional plots of C_p in figures 6.26 and 6.28 bear close resemblance to the corresponding density plots, featuring very strong and rapid changes near the leading edge and nearly constant profiles elsewhere. The pressure plots do not reveal the existence of a secondary shock running parallel to

the symmetry plane. Nevertheless a secondary shock is present and its structure is most clearly illustrated by the Mach number contour and velocity vector plots in figures 6.20,6.23,6.39 and 6.40.

The contour plots of Mach number shows the secondary shock in an almost vertical position. Therefore the x-y component of the Mach number can be used to approximate the normal Mach number at the shock. Plots at station $J = 66$ are presented in figures 6.36 to 6.38. This station corresponds to the constant η line that meets the symmetry plane at $\frac{Z}{Y_{le}} = 0.5$. At this location the position of the secondary shock is fairly well defined and values can be read with a minimum of error. The xy-Mach contour plot in figure 6.36 indicates that the Mach number at 80% chord adjacent to the shock is about 7.7. From the veolcity vector plot in figure 6.37 the angle between the shock and the velocity direction was found to be about 20°. This result gives a normal Mach number of about 2.63 going into the shock. The total pressure loss in figure 6.38 gives a total pressure ratio of 0.37 which corresponds to a normal Mach number of 2.86. The normal Mach number derived from the two methods match fairly well and both serve to confirm the existence of the secondary shock.

The position of the secondary shock cannot be seen in the total pressure loss plots in figures 6.32 and 6.33. However if the values were thresholded so that only total pressure losses above 90% was displayed, then the locations of flow separation and the secondary shock become clear. These thresholded plots are shown in figures 6.34 and 6.35.

The vector plots indicate the position of the primary separation and the subsequent peeling off of the boundary layer from the body to form a free shear layer which leaves the surface at about 15°. As this shear layer approaches the symmetry plane, it eventually meets the secondary shock. Captured between the free shear layer and the leeward surface is a recirculation zone where a vortex is clearly distin-

guishable. Outboard of this location the boundary layer profile becomes inflected and eventually separates at about $\frac{Y}{Y_{le}}$ of 0.35. Here the external flow appears to pass over a bump indicating the possibility of a separation bubble. Further evidence of this phenomena is provided by C_f lines on the upper surface. Outboard of the secondary separation a reattachment region is observed. However the cross-flow velocity vector plots give no indication of a recirculation zone adjacent to the body, though the velocity profiles are extremely inflected here. The evidence point to an incipient separation bubble. Contour plots of Mach number gives essentially the same information as above. The location of the separated free shear layer as well as the structure of the boundary layer inboard of this location are clearly indicated. However inboard of the secondary separation, the contour lines indicate some sort of bifurcation in the flow. Something appears to be happening but the present plots do not offer enough information for a substantial analysis.

Skin friction coefficient and Stanton number will be examined here. Although presently there is no way to verify the accuracy of the skin friction, it is possible to check the values qualitatively by comparing the y-component of the skin friction to the cross-flow velocity vector plots. The y-component of C_f is defined as;

$$C_{f_y} = \vec{C}_f \cdot \vec{j} \tag{6.4}$$

The values of C_{f_y} in figures 6.45 and 6.46 show trends that agree with the velocity vector plots. As the flow accelerates pass the leading edge, the velocity gradient normal to the wall increases. This effect is clearly displayed in blowups of the velocity vector plots in figures 6.21 and 6.24. These plots show that the acceleration is so great that velocity overshoots occur within the boundary layer. Naturally the higher velocity gradient results in increased shear and C_{f_y} increases rapidly near the leading edge. However as this is occurring, the wing surface is also changing its orientation and decreasing its y-component of the area. Near the wing tip the decrease in the area outweighs the increase in total wall shear and C_{f_y} drops precipitously, becoming negative as the flow moves inboard on the leeward surface. The y-component of wall

shear then goes to zero as the flow passes over the separated region and then to a positive value in the vicinity of reverse flow. These trends are consistent with the flowfield shown in the velocity vector plots in figures 6.20 and 6.23, and leads to the conclusion that the results are at least qualitatively correct.

Figures 6.41 and 6.42 show plots of Stanton numbers on the wing at the 50% and 80% chord positions. The values indicate that on both surfaces, heat is being transfered from the surroundings to the wing. The laminar equivalent of the Reynolds analogy states that under certain conditions, the Stanton number can be related to the skin friction. For flows where ρ, μ, k and pressure in the flow direction are constant and the term $\mu(\frac{du}{dy})^2$ is small enough so that is can be neglected in the energy equation, it is possible to show that the Stanton number is equal to half the skin friction coefficient [Kuethe & Chow] [15]. This result has been shown to hold for flows up to Mach 5. For this wing, although the density and pressure at the leading edge varies drastically, the values on the upper and lower surfaces are approximately constant, and so the conditions are partially satisfied over most of the wing. Figures 6.43 and 6.44 present C_f magnitude plots in a manner that makes it easy to compare with the plots of Stanton number. The plots show that the relationship between Stanton number and C_f holds up reasonably well over much of the surface. The main points of departure occur at the leading edge and on the leeward surface near the symmetry plane. Since density and pressure are varying rapidly near the leading edge, the relationship cannot be expected to hold well. On the leeward surface, the flow near the symmetry plane is strongly accelerated outboard by a pressure gradient. Furthermore density plots indicate a significant variation of density in this region. Therefore the agreement between C_f and Stanton number must be weak. Since the Stanton number and C_f are derived independently in this simulation, the agreement to the theoretical relationship gives an indication of the accuracy of these viscous quantities.

On all surfaces the Stanton numbers are negative indicating that air in the

boundary layer is being cooled. On the windward surface, the Stanton number is about 1×10^3 at the symmetry plane and increases slowly further outboard. Near the leading edge, the value rises rapidly and then drops to almost 0 as the flow separates on the leeward surface. The Stanton numbers stays at a very low value over much of this surface, with the exception of the region near the symmetry plane where a stagnation point is located and a strongly accelerated reverse flow occurs. The plots of C_f magnitude shows the same trends but the changes near the leading edge and the leeward surface stagnation point are less pronounced.

Plots of total temperature loss and vorticity are shown in figures 6.47 to 6.50. In the separated region the total temperature loss reflects the structure observed in the Mach number plots. Rapid changes coincide with regions of shear flow. The plots of vorticity in figures 6.49 and 6.50 show an increase in the amount of vorticity across the shock. The boundary layer and the most of the leeward surface also exhibit a high levels of vorticity.

$M = 7.15, Re = 5.85 \times 10^6, \alpha = 30.0°, Grid = 33 \times 97 \times 97, X/C = 0.50$
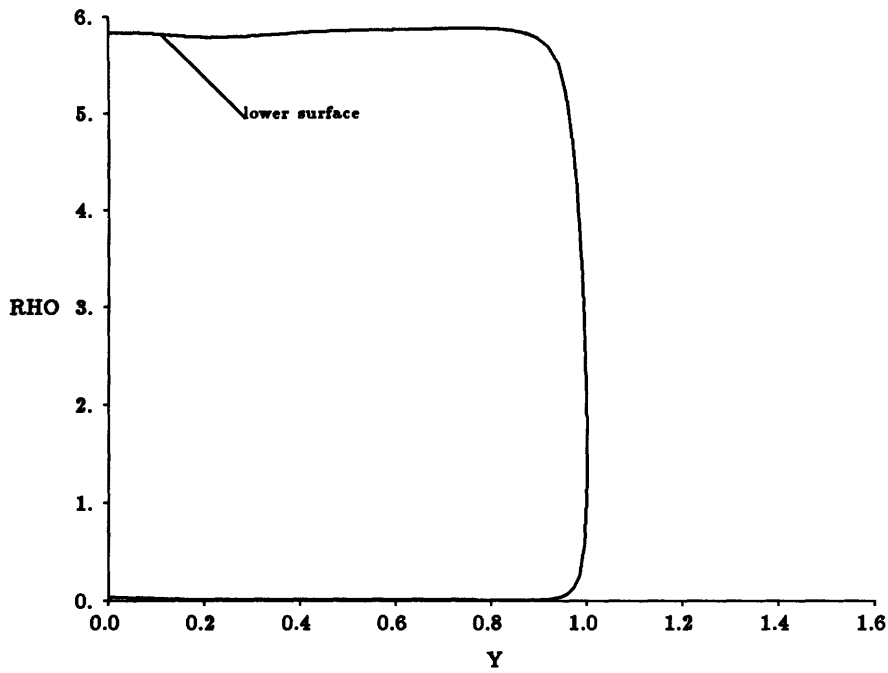DENSITY ON BODY

Figure 6.16: Density on the wing at 50% chord

$M = 7.15, Re = 5.85 \times 10^6, \alpha = 30.0°, Grid = 33 \times 97 \times 97, X/C = 0.80$
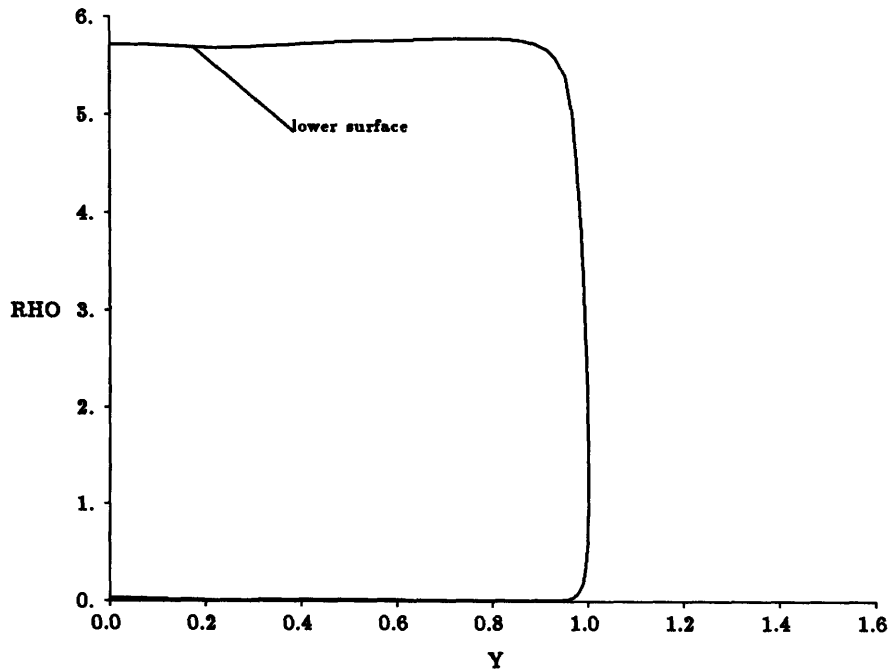DENSITY ON BODY

Figure 6.17: Density on the wing at 80% chord

$M = 7.15, Re = 5.85 \times 10^6, \alpha = 30.0°, Grid = 33 \times 97 \times 97, X/C = 0.50$
DENSITY CONTOURS

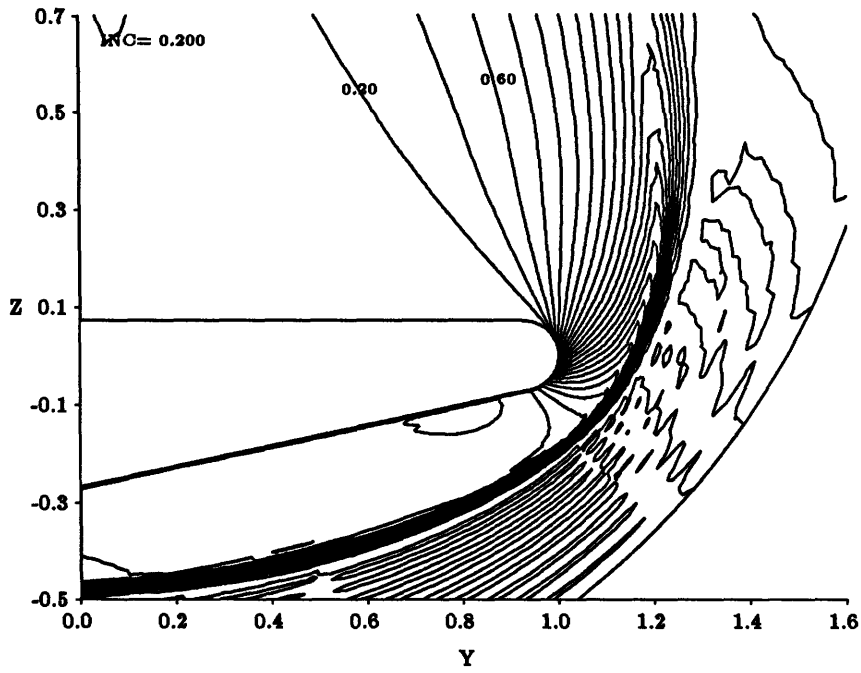Figure 6.18: Contour plot of density at 50% chord

$M = 7.15, Re = 5.85 \times 10^6, \alpha = 30.0°, Grid = 33 \times 97 \times 97, X/C = 0.80$
DENSITY CONTOURS

Figure 6.19: Contour plot of density at 80% chord

110

$M = 7.15, Re = 5.85 \times 10^6, \alpha = 30.0^\circ, Grid = 33 \times 97 \times 97, X/C = 0.50$
V-W VELOCITY VECTOR PLOT
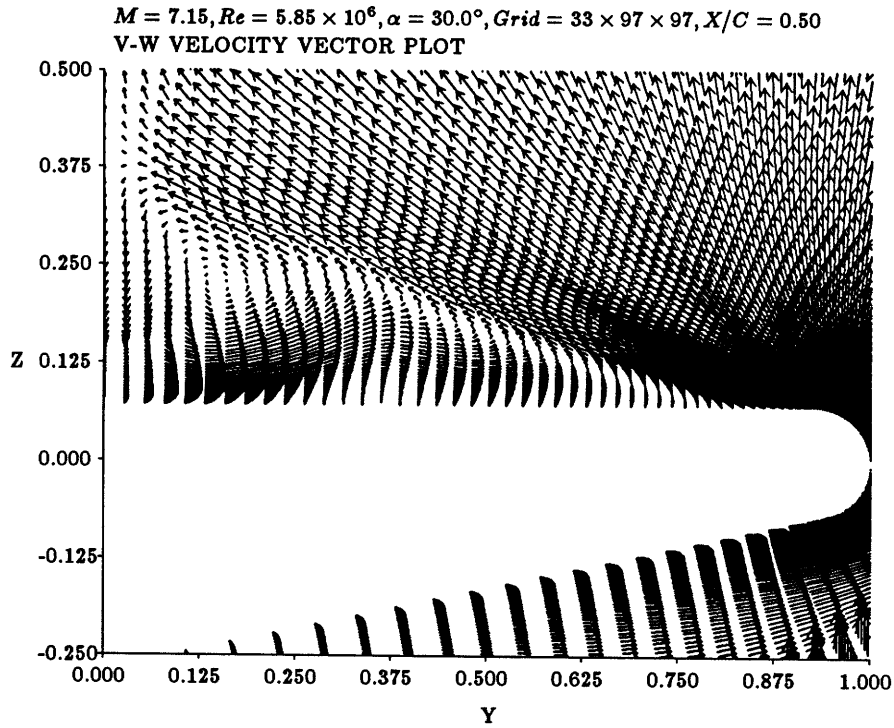
Figure 6.20: Vector plot of velocity at 50% chord

$M = 7.15, Re = 5.85 \times 10^6, \alpha = 30.0^\circ, Grid = 33 \times 97 \times 97, X/C = 0.50$
V-W VELOCITY VECTOR PLOT
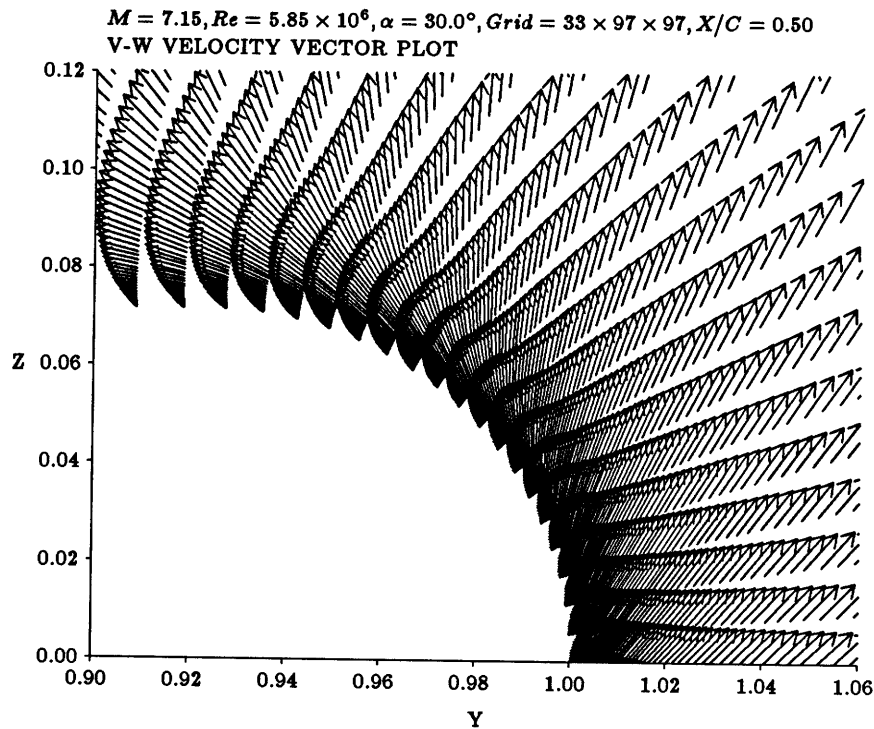
Figure 6.21: Closeup of velocity vector plot at 50% chord

111

$M = 7.15, Re = 5.85 \times 10^6, \alpha = 30.0°, Grid = 33 \times 97 \times 97, X/C = 0.50$
V-W VELOCITY VECTOR PLOT
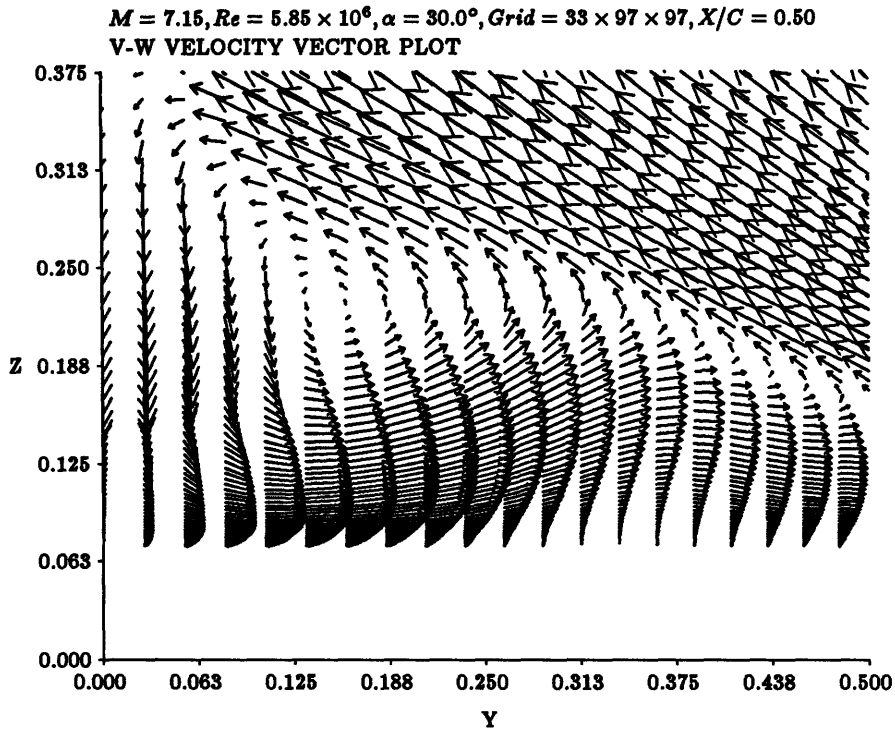
Figure 6.22: Closeup of velocity vector plot at 50% chord

$M = 7.15, Re = 5.85 \times 10^6, \alpha = 30.0°, Grid = 33 \times 97 \times 97, X/C = 0.80$
V-W VELOCITY VECTOR PLOT

Figure 6.23: Vector plot of velocity at 80% chord

112

$M = 7.15, Re = 5.85 \times 10^6, \alpha = 30.0°, Grid = 33 \times 97 \times 97, X/C = 0.80$
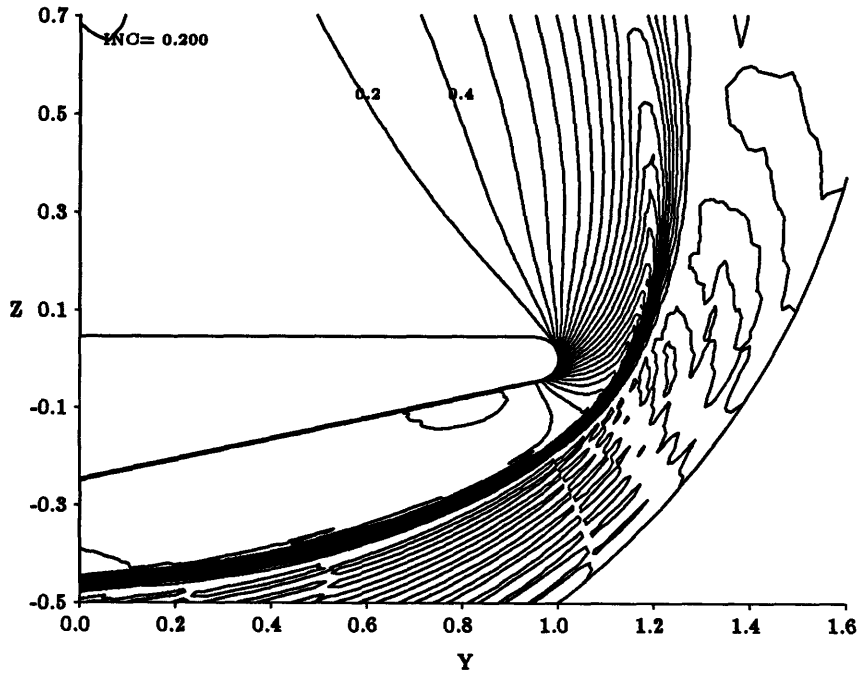V-W VELOCITY VECTOR PLOT
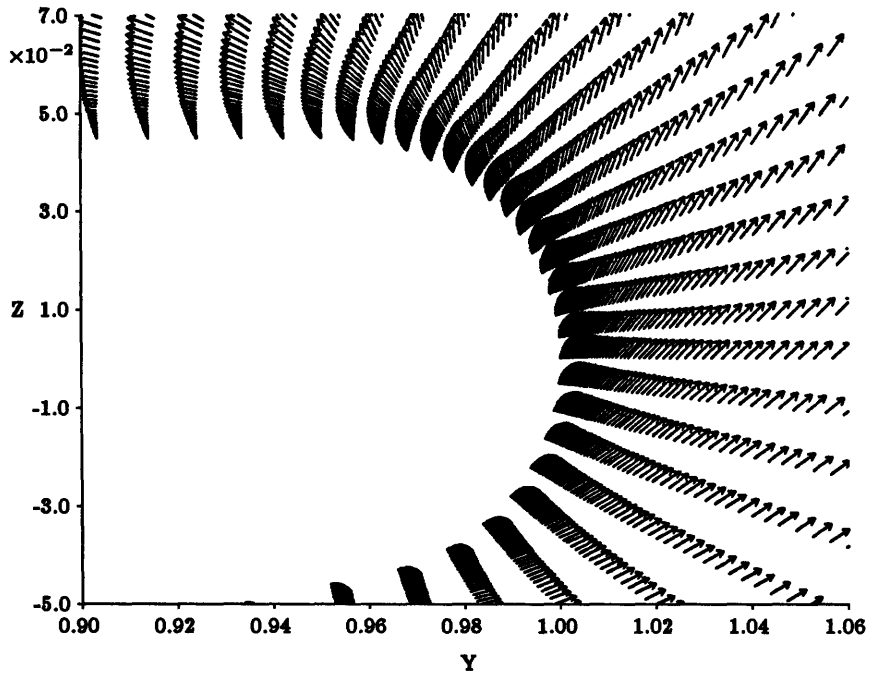
Figure 6.24: Closeup of velocity vector plot at 80% chord

$M = 7.15, Re = 5.85 \times 10^6, \alpha = 30.0°, Grid = 33 \times 97 \times 97, X/C = 0.80$
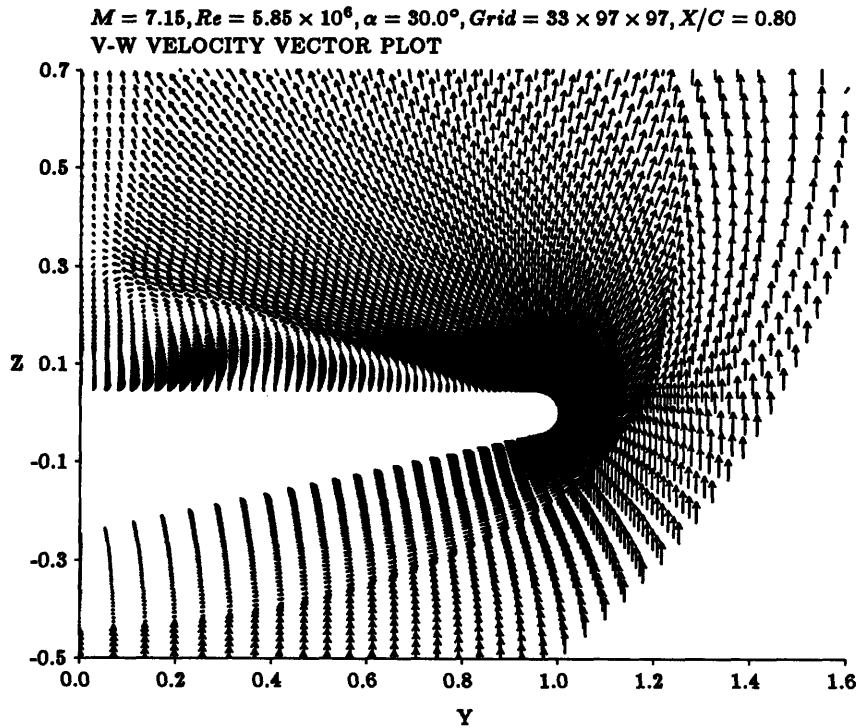V-W VELOCITY VECTOR PLOT

Figure 6.25: Closeup of velocity vector plot at 80% chord

113

$M = 7.15, Re = 5.85 \times 10^6, \alpha = 30.0°, Grid = 33 \times 97 \times 97, X/C = 0.50$
PRESSURE COEFFICIENT ON THE BODY
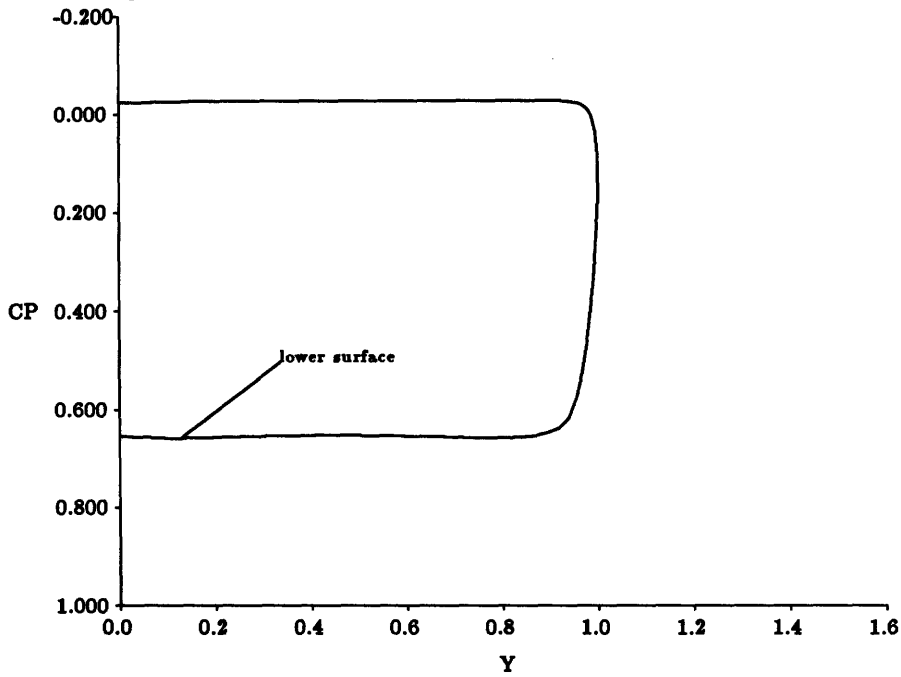
Figure 6.26: C_p on the wing at 50% chord

$M = 7.15, Re = 5.85 \times 10^6, \alpha = 30.0°, Grid = 33 \times 97 \times 97, X/C = 0.50$
PRESSURE COEFFICIENT ON THE BODY
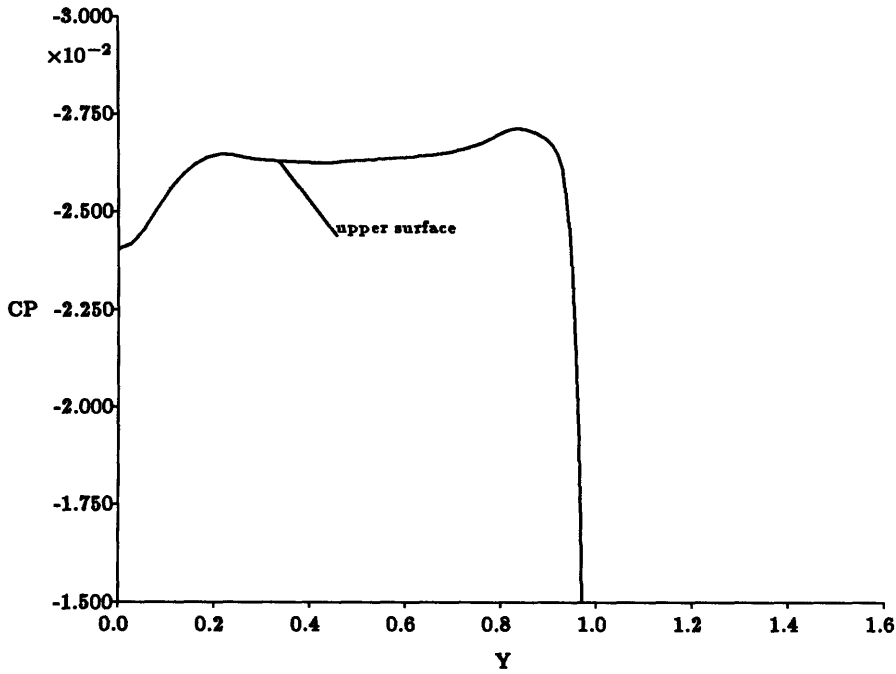
Figure 6.27: Blowup of C_p on the wing at 50% chord

114

$M = 7.15, Re = 5.85 \times 10^6, \alpha = 30.0°, Grid = 33 \times 97 \times 97, X/C = 0.80$
PRESSURE COEFFICIENT ON THE BODY
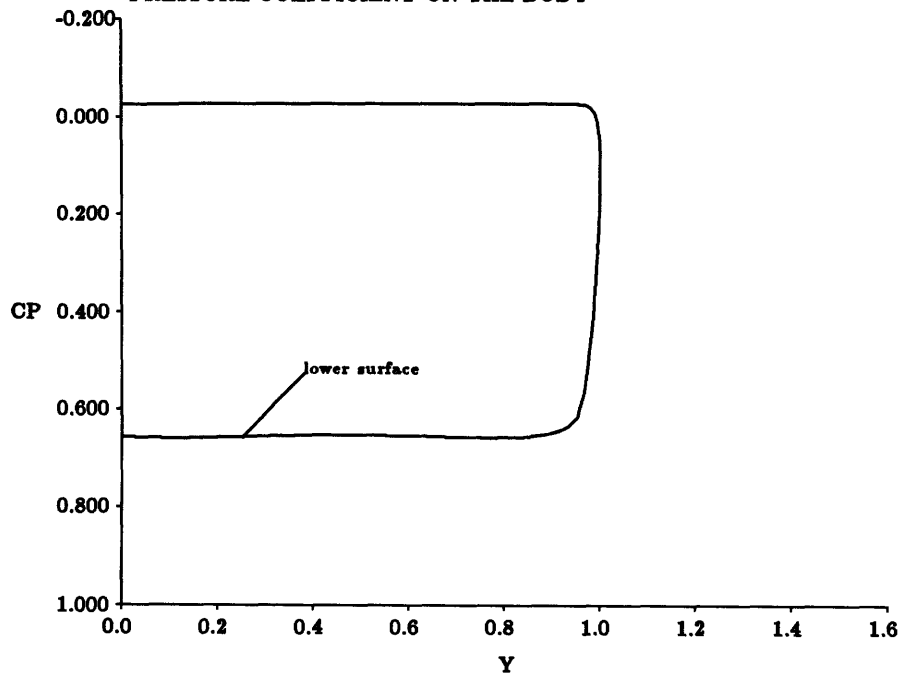
Figure 6.28: C_p on the wing at 80% chord

$M = 7.15, Re = 5.85 \times 10^6, \alpha = 30.0°, Grid = 33 \times 97 \times 97, X/C = 0.80$
PRESSURE COEFFICIENT ON THE BODY
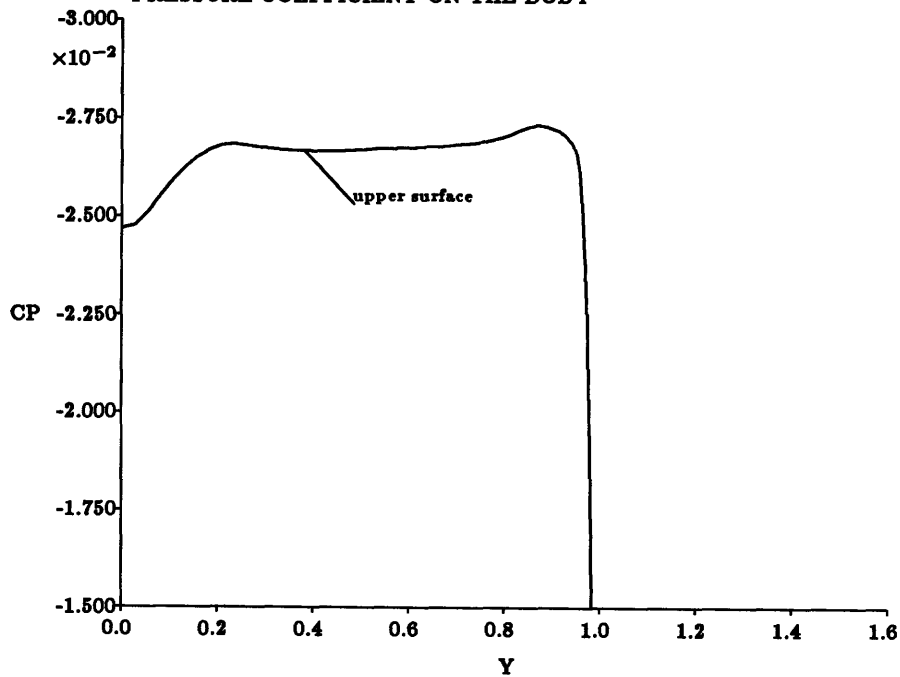
Figure 6.29: Blowup of C_p on the wing at 80% chord

115

$M = 7.15, Re = 5.85 \times 10^6, \alpha = 30.0°, Grid = 33 \times 97 \times 97, X/C = 0.50$
CP
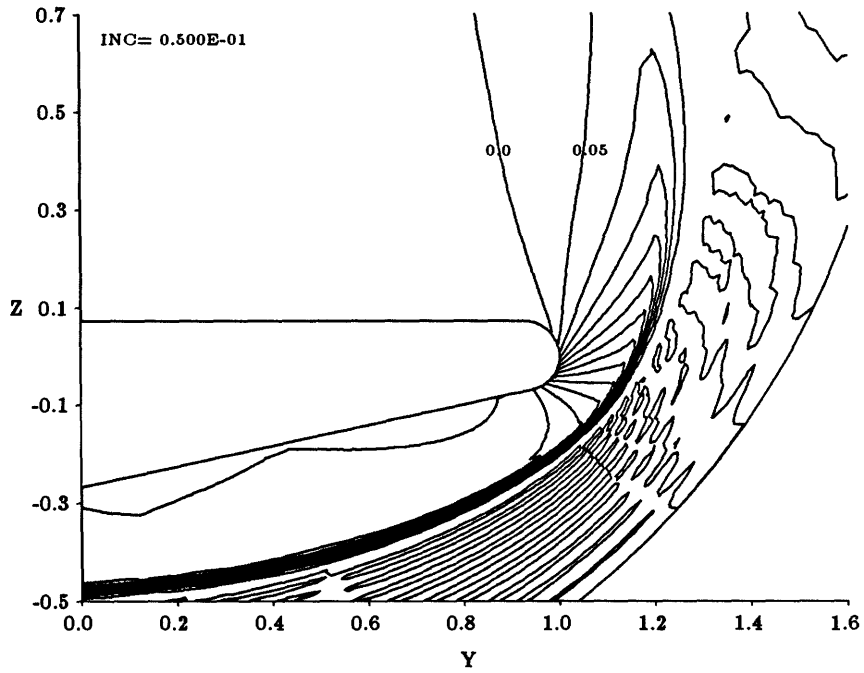
Figure 6.30: Contour plot of C_p at 50% chord

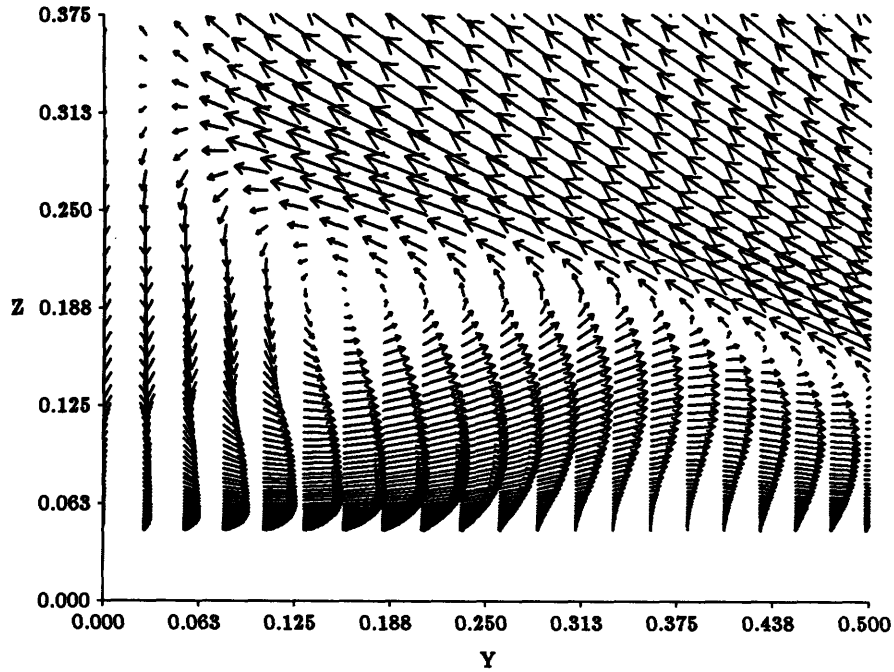$M = 7.15, Re = 5.85 \times 10^6, \alpha = 30.0°, Grid = 33 \times 97 \times 97, X/C = 0.80$
CP
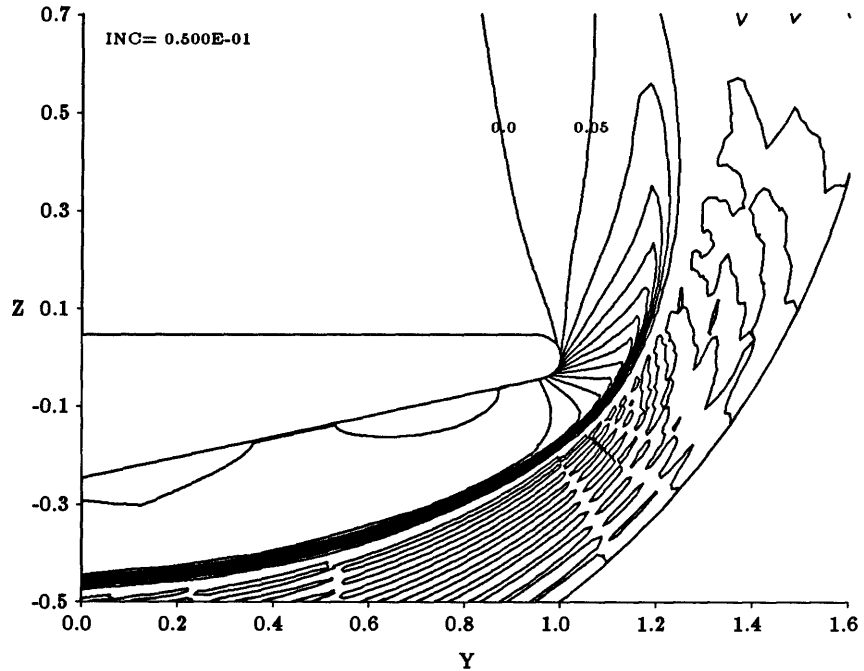
Figure 6.31: Contour plot of C_p at 80% chord

$M = 7.15, Re = 5.85 \times 10^6, \alpha = 30.0°, Grid = 33 \times 97 \times 97, X/C = 0.50$
TOTAL PRESSURE LOSS CONTOURS
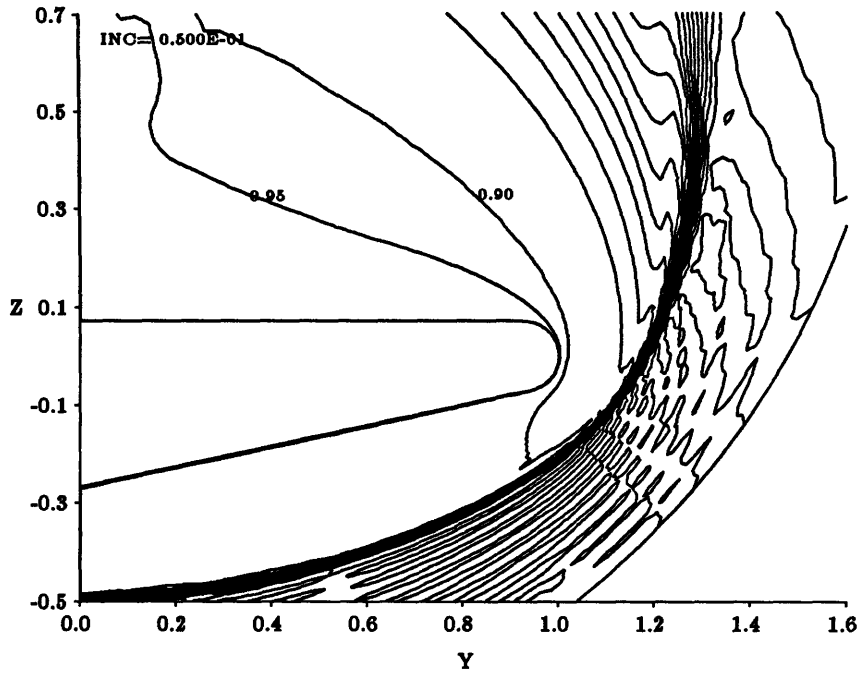
Figure 6.32: Contour plot of total pressure loss at 50% chord

$M = 7.15, Re = 5.85 \times 10^6, \alpha = 30.0°, Grid = 33 \times 97 \times 97, X/C = 0.80$
TOTAL PRESSURE LOSS CONTOURS

Figure 6.33: Contour plot of total pressure loss at 80% chord

$M = 7.15, Re = 5.85 \times 10^6, \alpha = 30.0°, Grid = 33 \times 97 \times 97, X/C = 0.50$
TOTAL PRESSURE LOSS CONTOURS

Figure 6.34: Thresholded contour plot of total pressure loss at 50% chord

$M = 7.15, Re = 5.85 \times 10^6, \alpha = 30.0°, Grid = 33 \times 97 \times 97, X/C = 0.80$
TOTAL PRESSURE LOSS CONTOURS

Figure 6.35: Thresholded contour plot of total pressure loss at 80% chord

118

$M = 7.15, Re = 5.85 \times 10^6, \alpha = 30.0°, Grid = 33 \times 97 \times 97, J = 66$
XY-COMP OF MACH NUMBER CONTOURS

INC= 0.500
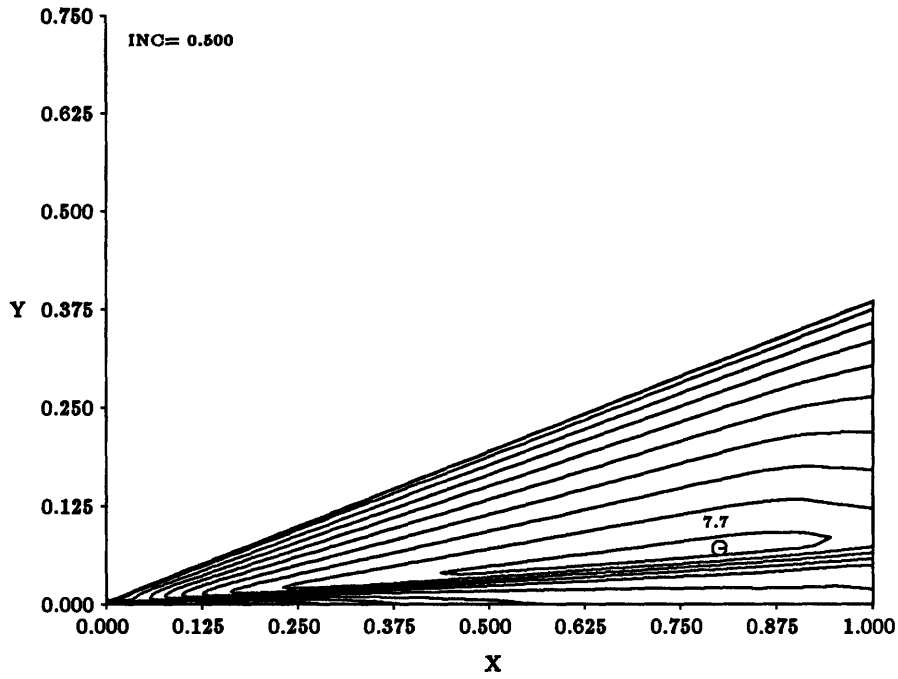
Figure 6.36: XY-component of Mach number at station $J = 66$

$M = 7.15, Re = 5.85 \times 10^6, \alpha = 30.0°, Grid = 33 \times 97 \times 97, J = 66$
U-V VELOCITY VECTOR PLOT
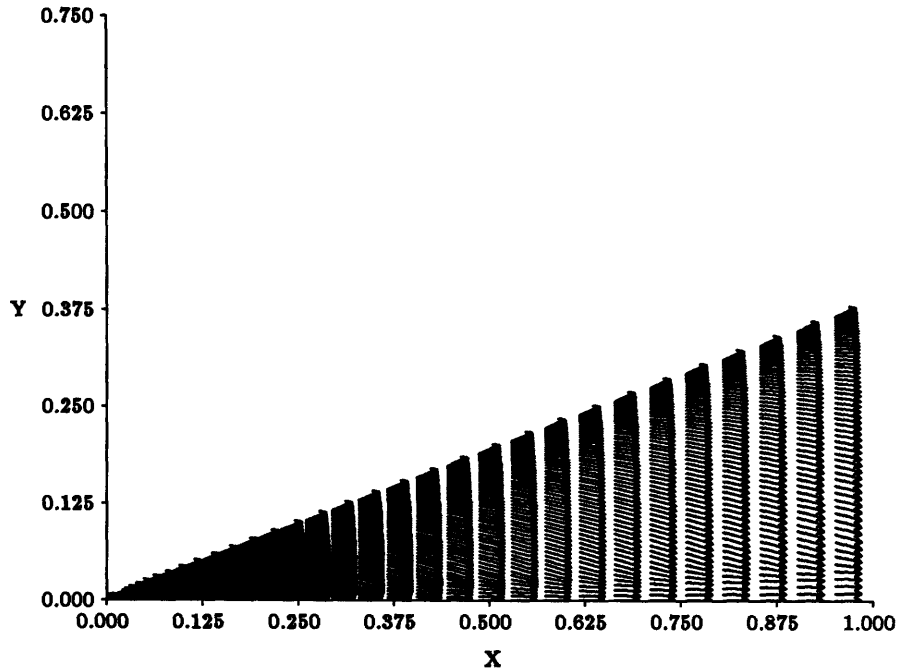
Figure 6.37: UV velocity vectors at station $J = 66$

$M = 7.15, Re = 5.85 \times 10^6, \alpha = 30.0°, Grid = 33 \times 97 \times 97, J = 66$
TOTAL PRESSURE LOSS CONTOURS
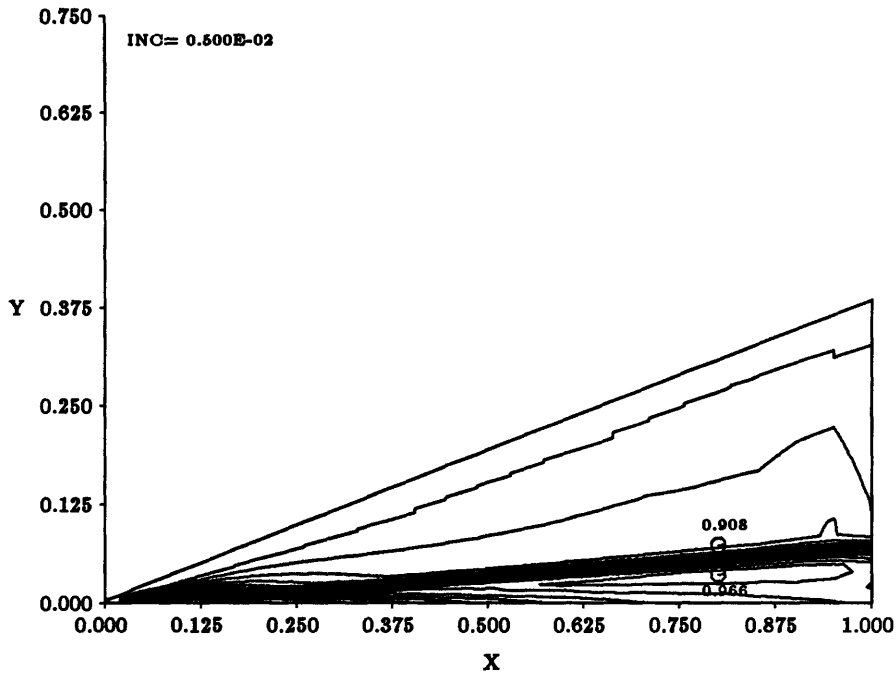
Figure 6.38: Thresholded total pressure loss at station $J = 66$

$M = 7.15, Re = 5.85 \times 10^6, \alpha = 30.00°, Grid = 33 \times 97 \times 97, X/C = 0.50$
MACH CONTOURS
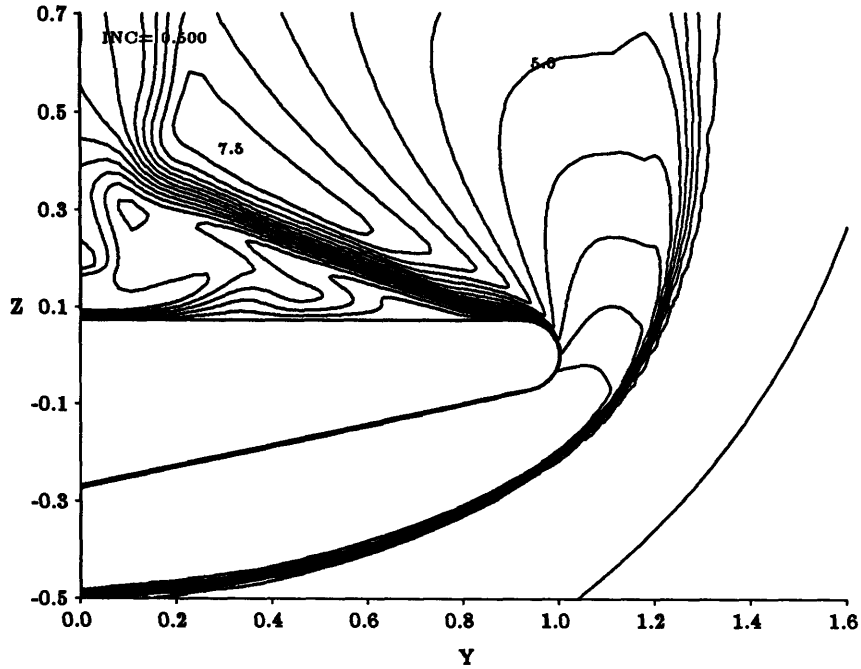
Figure 6.39: Contour plot of Mach number at 50% chord

120

$M = 7.15, Re = 5.85 \times 10^6, \alpha = 30.0°, Grid = 33 \times 97 \times 97, X/C = 0.80$
MACH CONTOURS
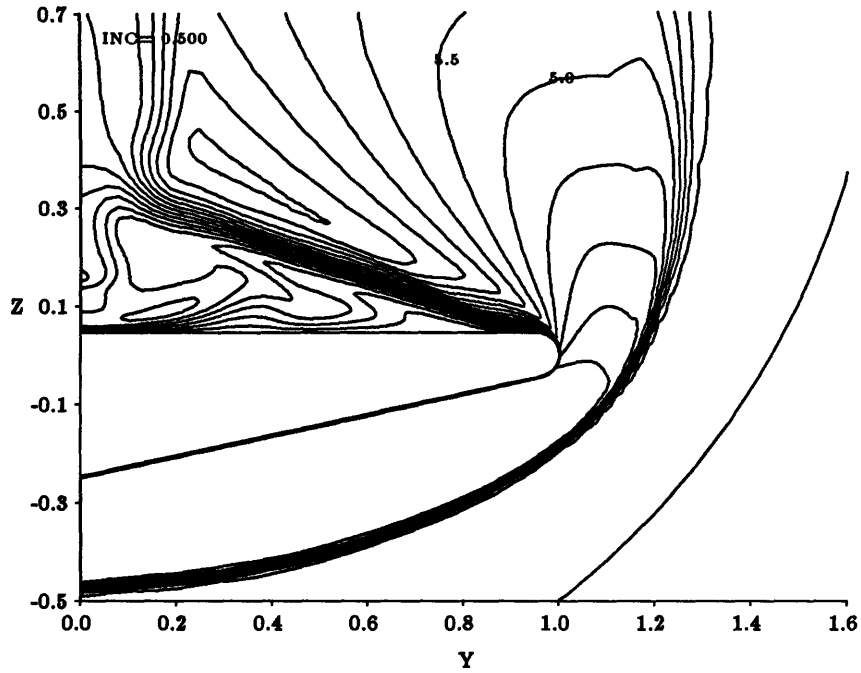


Figure 6.40: Contour plot of Mach number at 80% chord

$M = 7.15, Re = 5.85 \times 10^6, \alpha = 30.0°, Grid = 33 \times 97 \times 97, X/C = 0.50$
STANTON NUMBER ON BODY
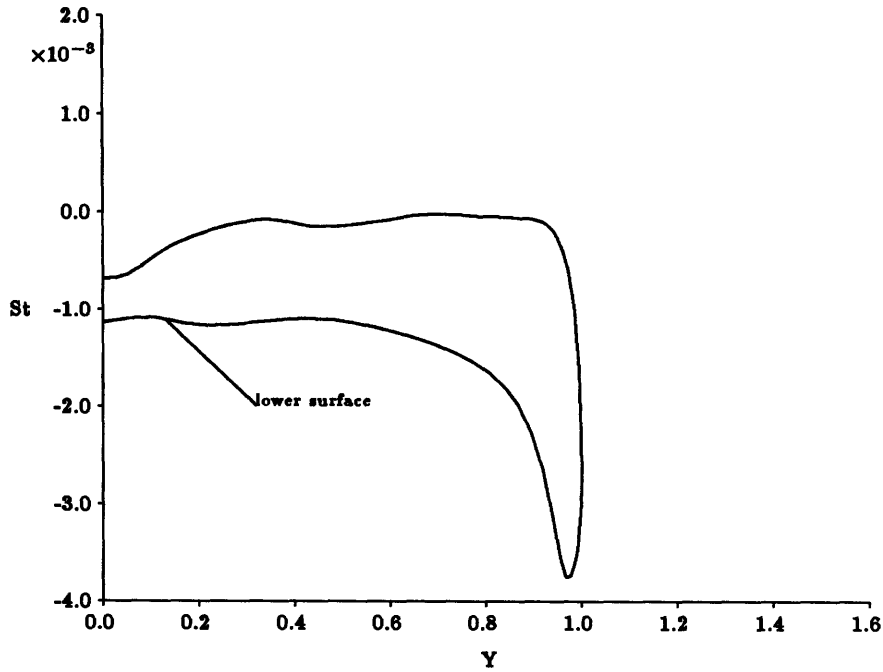
Figure 6.41: St on body at 50% chord

121

$M = 7.15, Re = 5.85 \times 10^6, \alpha = 30.0°, Grid = 33 \times 97 \times 97, X/C = 0.80$
STANTON NUMBER ON BODY
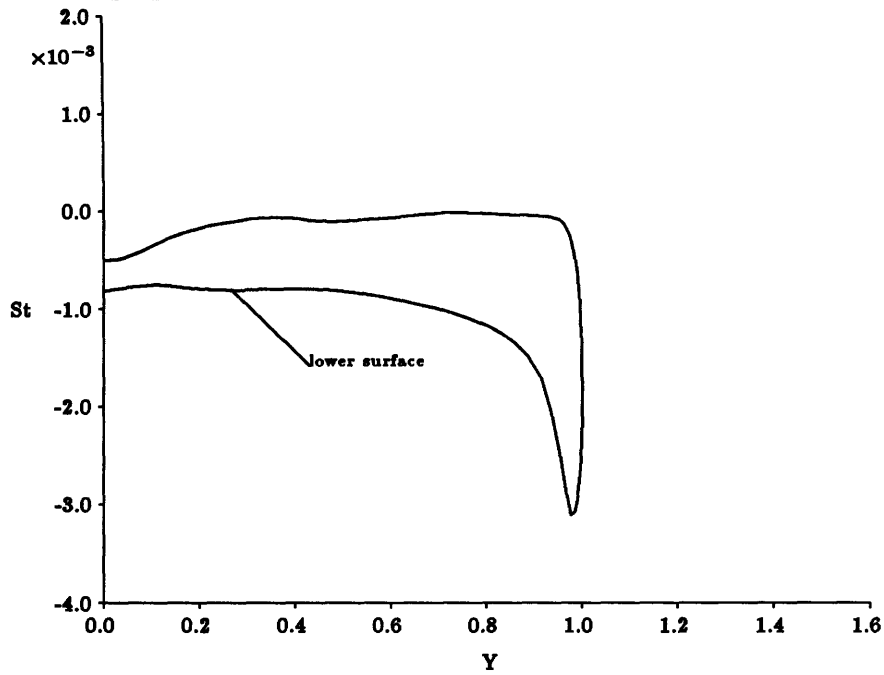
Figure 6.42: St on body at 80% chord

$M = 7.15, Re = 5.85 \times 10^6, \alpha = 30.0°, Grid = 33 \times 97 \times 97, X/C = 0.50$
C_f MAGNITUDE ON THE BODY
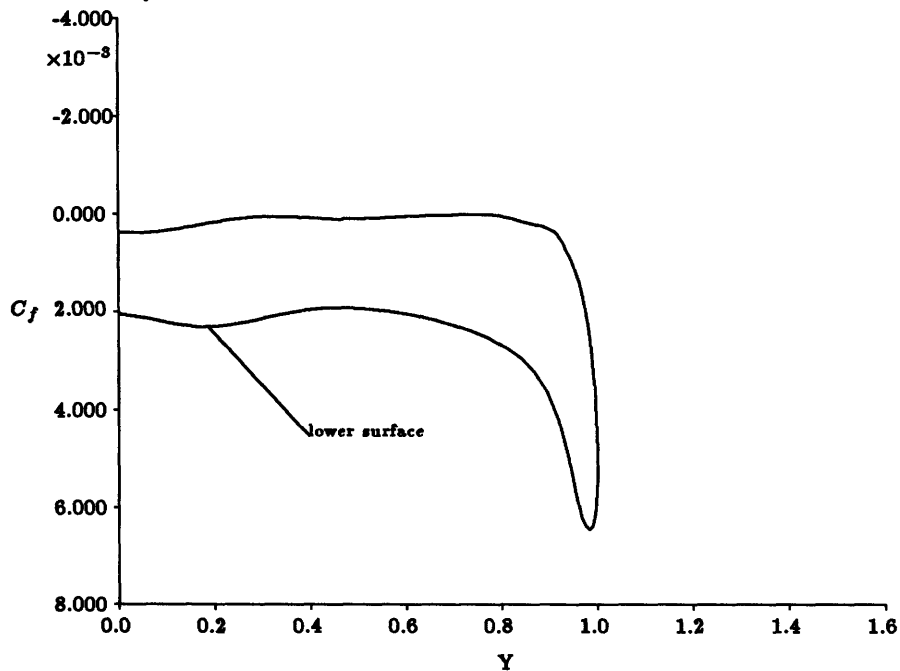
Figure 6.43: Magnitude of C_f on body at 50% chord

122

$M = 7.15, Re = 5.85 \times 10^6, \alpha = 30.0°, Grid = 33 \times 97 \times 97, X/C = 0.80$
C_f MAGNITUDE ON THE BODY

lower surface
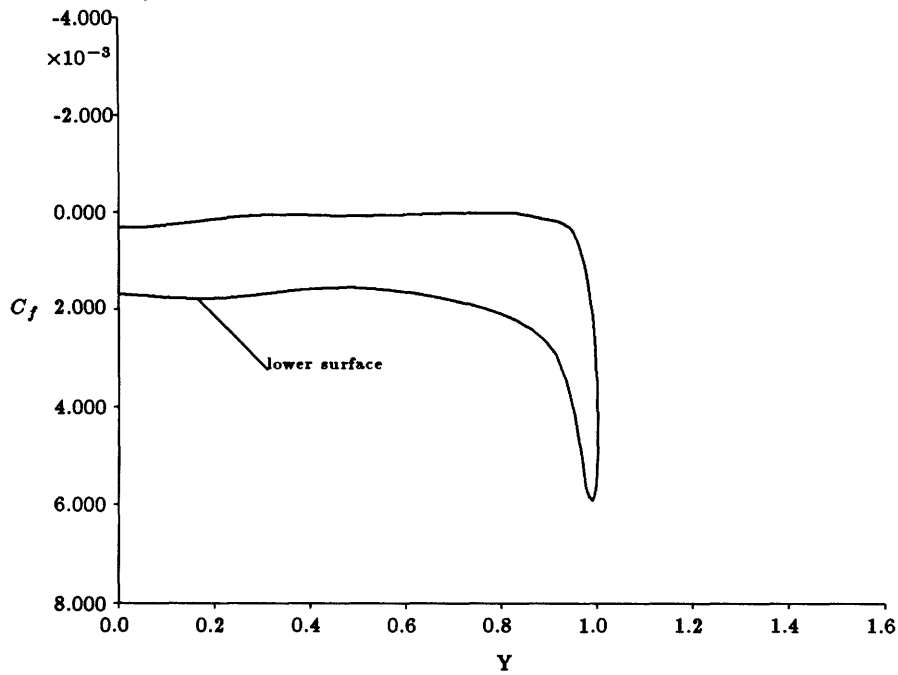
Figure 6.44: Magnitude of C_f on body at 80% chord

$M = 7.15, Re = 5.85 \times 10^6, \alpha = 30.0°, Grid = 33 \times 97 \times 97, X/C = 0.50$
Y-COMPONENT OF C_f ON THE BODY

lower surface
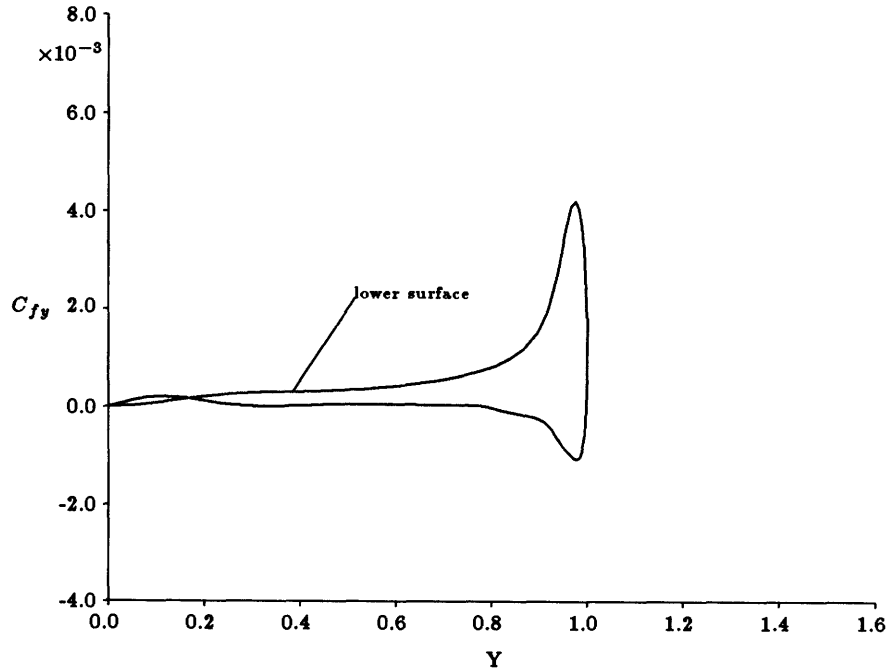
Figure 6.45: Cf_y on body at 50% chord

123
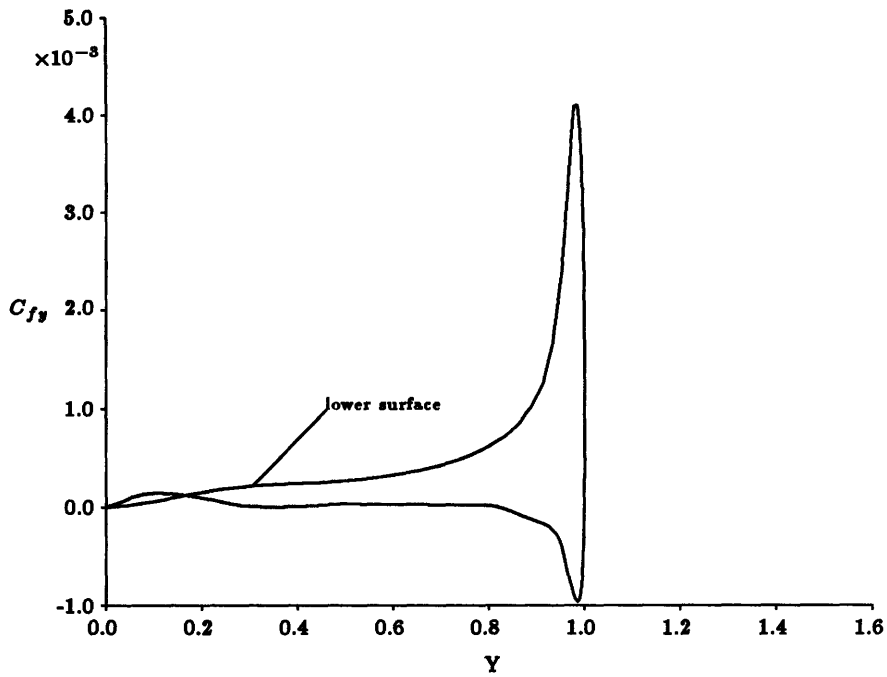
Figure 6.46: Cf_y on body at 80% chord

$M = 7.15, Re = 5.85 \times 10^6, \alpha = 30.0°, Grid = 33 \times 97 \times 97, X/C = 0.50$
TOTAL TEMPERATURE LOSS CONTOURS
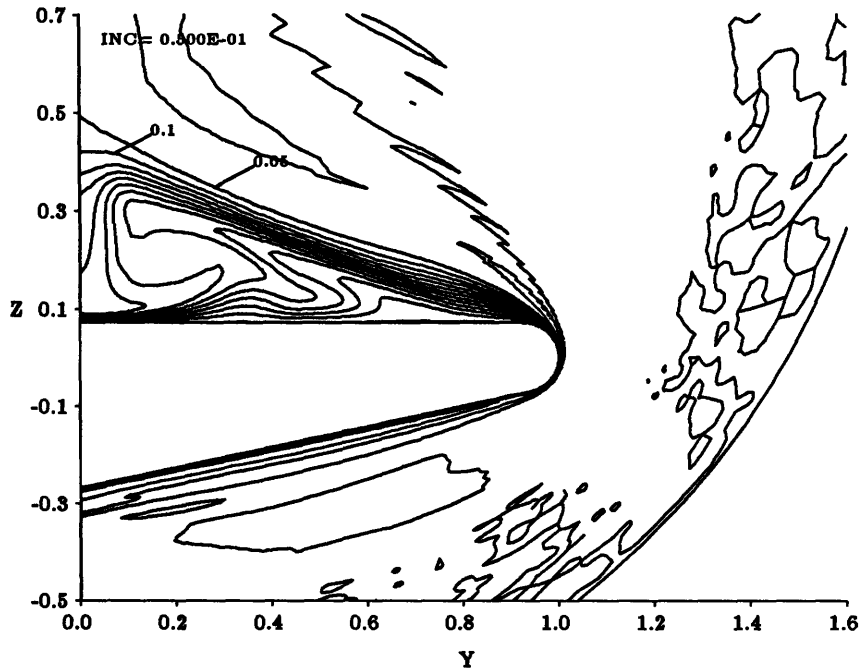
Figure 6.47: Contour plot of total temperature loss at 50% chord

$M = 7.15, Re = 5.85 \times 10^6, \alpha = 30.0°, Grid = 33 \times 97 \times 97, X/C = 0.80$
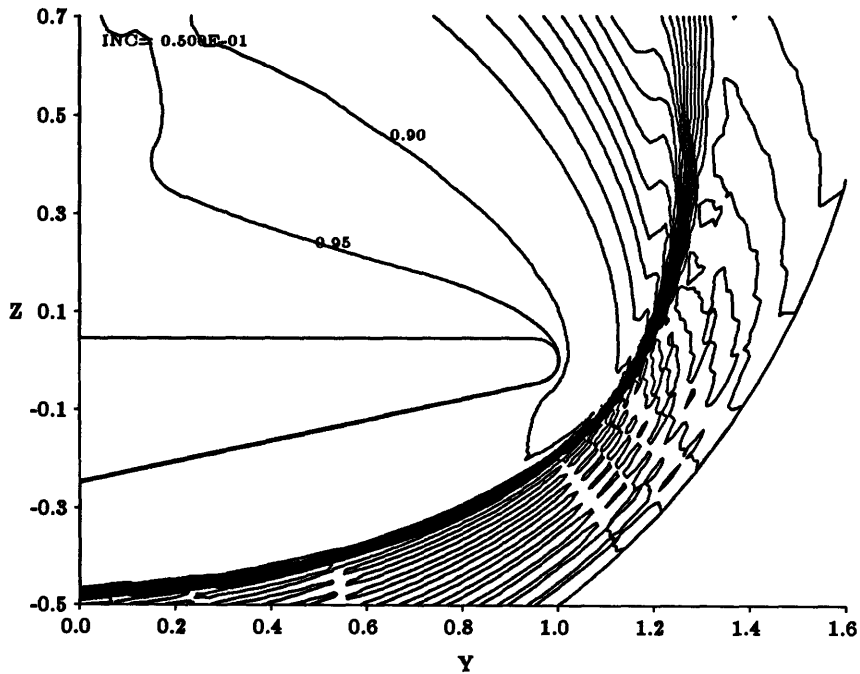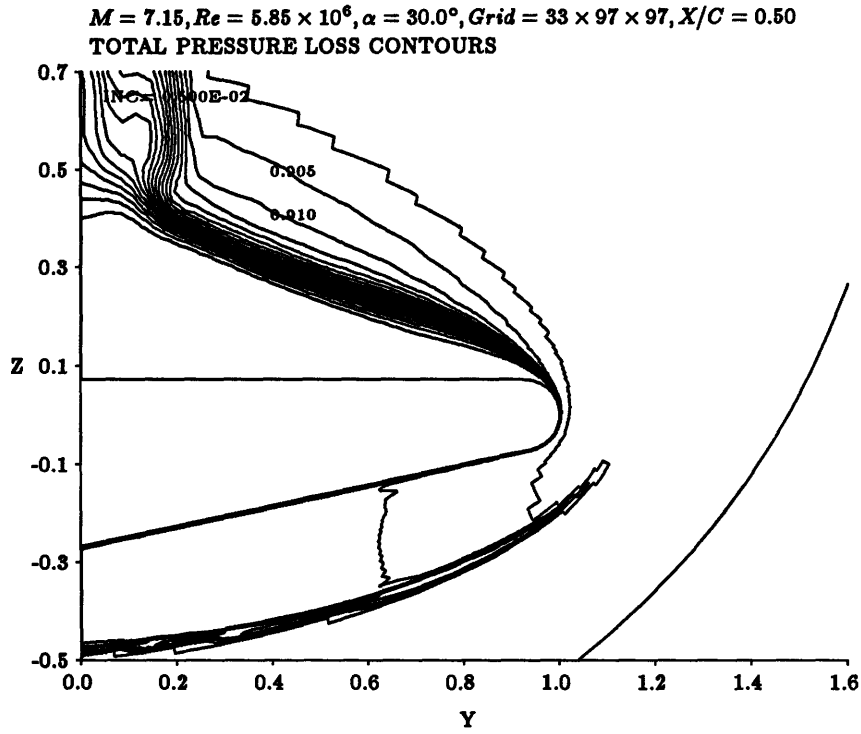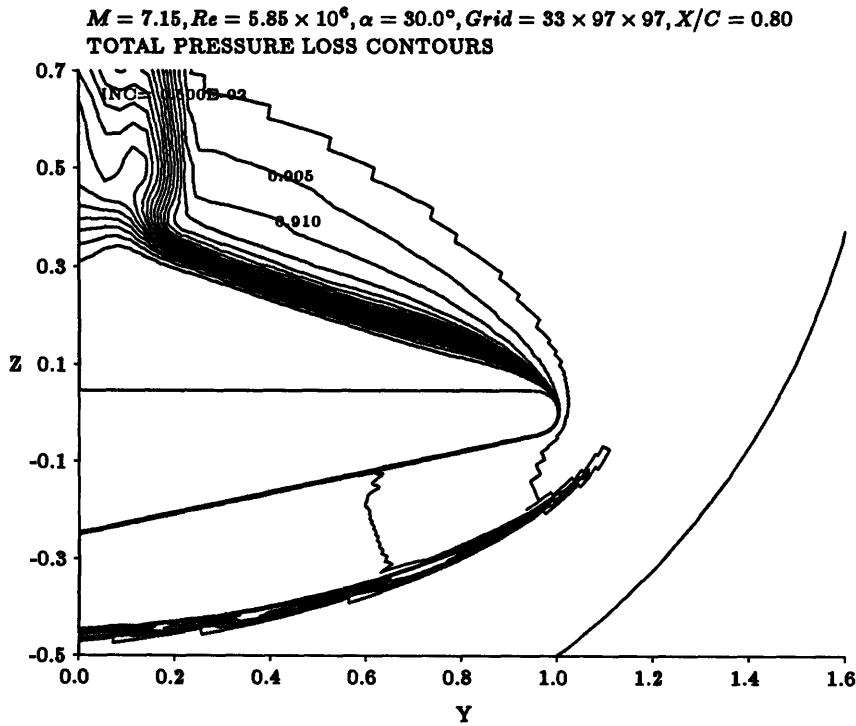**TOTAL TEMPERATURE LOSS CONTOURS**
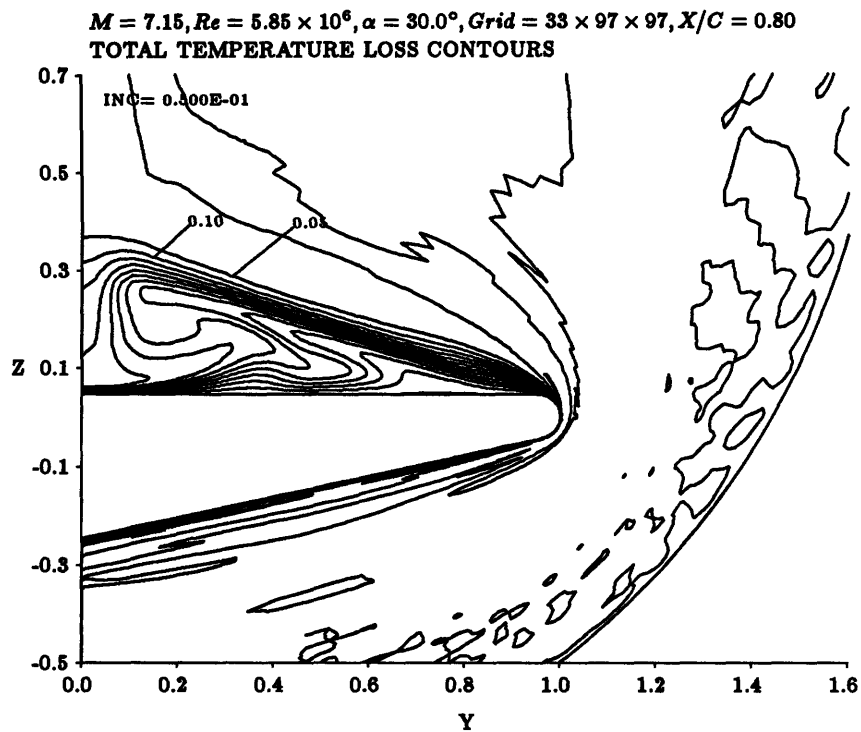
Figure 6.48: Contour plot of total temperature loss at 80% chord

$M = 7.15, Re = 5.85 \times 10^6, \alpha = 30.0°, Grid = 33 \times 97 \times 97, X/C = 0.50$
VORTICITY MAGNITUDE CONTOURS
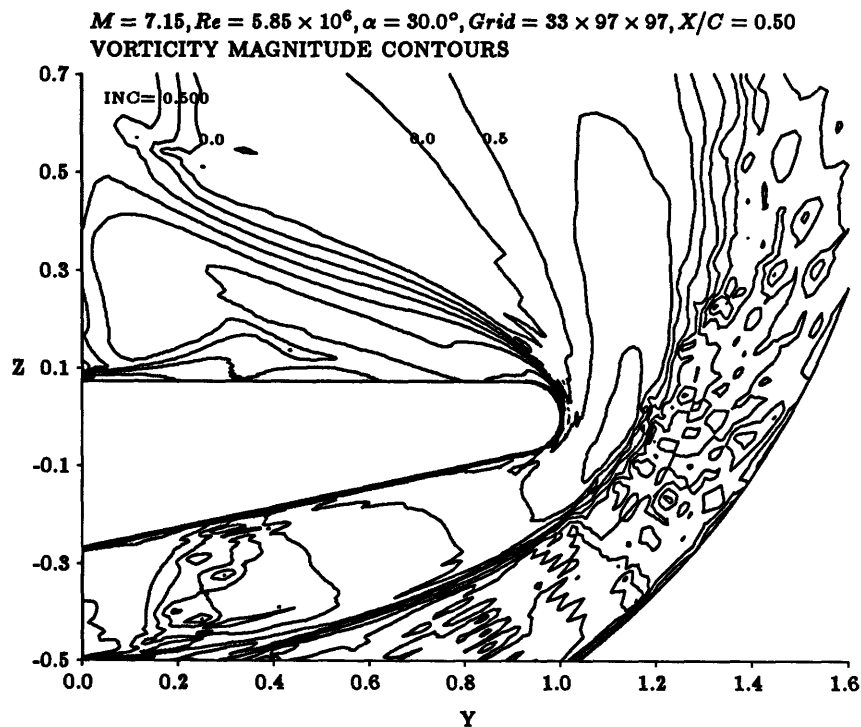
Figure 6.49: Contour plot of log_{10} of vorticity magnitude at 50% chord

$M = 7.15, Re = 5.85 \times 10^6, \alpha = 30.0°, Grid = 33 \times 97 \times 97, X/C = 0.80$

VORTICITY MAGNITUDE CONTOURS
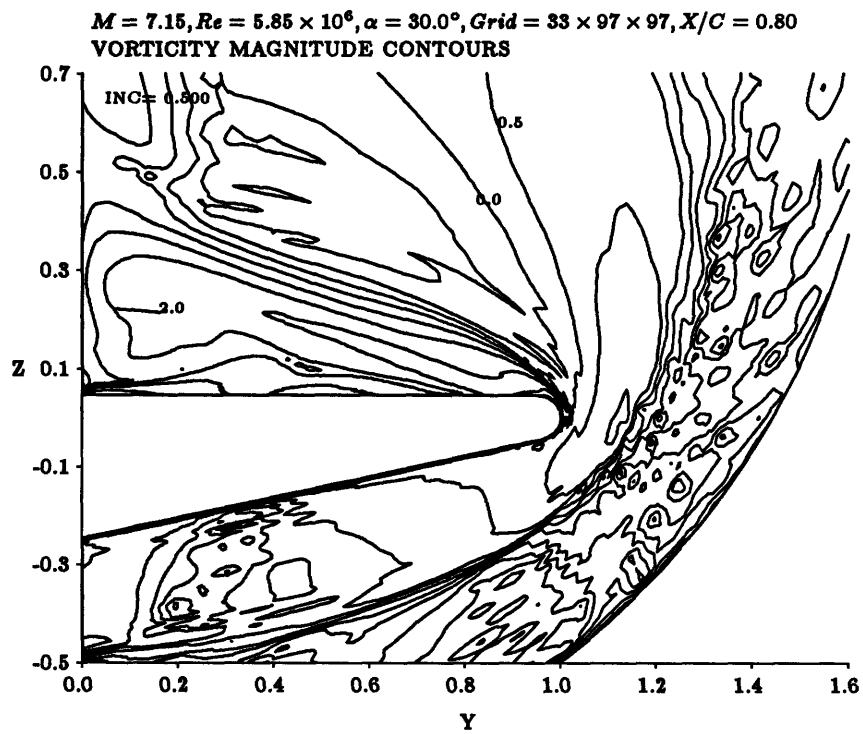
Figure 6.50: Contour plot of log_{10} of vorticity magnitude at 80% chord

Chapter 7

Comparison of Inviscid and Viscous Results

The computational cost of solutions to the Navier-Stokes equations can be prohibitively high. Therefore considerable savings can be attained if the conditions permit the use of the Euler equations in modeling the flow. From the engineering perspective, the coefficients of lift and drag are the most important quantities and the above calculations show that solutions to the two sets of equations produce very similar values. If this was the only consideration, then this flow can certainly be modeled by the Euler equations. However other requirements may be important, for example the values of heat transfer and skin friction coefficient at the wall. The purpose of this comparison is to highlight where and why the two solutions agree, so that we may be better able to judge when the solution to the Euler equations satisfies the modeling requirements.

The density contour plots show that for most of the flowfield, the distribution in the Euler and Navier-Stokes solutions are similar. The point of departure occurs on the windward surface of the wing, where rapid increase in the density takes place within the boundary layer of the Navier-Stokes simulation. This increase is the result of an isothermal wall that cools the flow in the boundary layer. This boundary layer and cooling are not captured in the Euler solutions and the corresponding increase in density near the wall is absent. On the leeward surface, the differences are not so pronounce because the separated flow results in a drastically reduced rate of heat transfer in the Navier-Stokes solutions. Therefore the density rise that comes from cooling is not observed. The differences and similarities between the two surface densities are clearly illustrated in figures 5.23, 5.24, 6.16 and 6.17.

A closer match between the two results can be found in the plots of pressure coefficient. The contour plots show remarkable similarity, with only minor variations at the primary shock that can be explained by the differences in grid quality. The shock appears more diffused in the inviscid solution because of the lower body-normal resolution of the Euler grid. Blow-ups of the pressure coefficient on the leeward surface in figures 5.41, 5.42, 6.27 and 6.29 serve to highlight the close match. The general trends are similar, even though the precise values vary slightly. The presence of a shock on the leeward surface give the inviscid results a more jagged distribution, whereas the pressure coefficient varies smoothly in the Navier-Stokes results. On the windward surface the pressure match is even better. This similarity results form the dominant nature of the primary shock. Since the body-normal pressure gradient in the boundary layer is negligible, the pressure on the windward surface is determined by the Rankine-Hugoniot conditions at the primary shock. Pressure on the lower surface of the inviscid solution is determined by the same mechanism, therefore it is hardly surprising that both results exhibit similar values. On the leeward surface the pressure is very close to zero, therefore the normal force is determined by the windward pressure. This similarity in windward pressure is the underlying cause for the the close match in lift and drag coefficients between the two results.

The total pressure loss contour plots in figures 5.48, 5.50, 6.32 and 6.33 show no major differences between the inviscid and viscous results. The viscous plots show rapid changes in the boundary layer on the windward surface, but besides this, the results look similar. However if the plots were thresholded so that only pressure losses in excess of 90% were plotted, the differences between the two flows become apparent. The viscous plots in figures 6.34 and 6.35 indicate a layer of rapid total pressure loss leaving the leading edge at an angle of 20° to the leeward surface. This layer corresponds to the shear layer separating from the wing. In the inviscid results, the unexplained total pressure loss at the leading edge results in a more dispersed total pressure loss pattern. Both plots indicate very clearly the location

of the secondary shock that runs parallel to the symmetry plane. However due to the different locations of flow separation on the leeward surfaces, the secondary shocks meet the separated layers at different distances from the body.

The similarities and differences in Mach number distribution mirror the total pressure losses discussed above. The different locations of flow separation is clearly visible from the Mach number contour plots in figures 5.33, 5.35, 6.39 and 6.40. The velocity vector plots indicate that the mechanism for flow separation is different between the two solutions. 'Inviscid separation' is observed on the leeward surface of the Euler results. This conclusion was arrived at in chapter 5, based on the observation of surface values of Mach number, total pressure loss and velocities. On the contrary the evidence indicates that separation in the viscous case results from the inability of the boundary layer to navigate the unfavorable pressure gradient on the leeward surface of the wing. The differences in mechanisms and locations of separation is the main dissimilarity between the inviscid and viscous results. Beside these and the changes in the windward boundary layer, the two results look almost identical.

Chapter 8

Conclusion

The main purpose of this thesis is to investigate the suitability of finite difference, cell centered, multi-stage temporal integration schemes in applications to hypersonic flows. To this end the explicit Jameson 4-stage integration technique was applied to the solution of the Euler equations at Mach 7.15 and 30° angle of attack. A semi-implicit variation of the above scheme was used to obtain the solution to the Navier-Stokes solution under similar conditions at a Reynolds number of 5.85×10^6, freestream temperature of $74K$ and wall temperature of $288K$.

Both results gave closely matching values of lift and drag. The lift and drag coefficients for the inviscid results are 0.547 and 0.383 respectively. The corresponding values for the viscous calculation are 0.547 and 0.386, with the skin friction contributing a meager 2.32×10^{-3} to the total drag coefficient. Most of the drag comes from the tilting for the normal force component on the wing as a result of the 30° angle of attack. It is clear that pressure is the determinant of the total lift and drag for the wing under these conditions.

Despite the close match in the values of lift and drag, the two results show quite different flows. The differences are most pronounced on the upper surface. The two flows exhibit different mechanisms for flow separation. The Euler solution displays inviscid separation, whereas the Navier-Stokes separation results from the inability of the flow to overcome an unfavorable pressure gradient. As a consequence of the different mechanisms, the flow separates at different locations; the viscous flow separates on the leeward surface just inboard of the leading edge, whereas the

inviscid flow separates at about 60% span. Differences are also observed on the windward surface. The effects of the boundary layer are clearly visible in the plots of Mach number and density. Unlike the inviscid results, the viscous solution shows rapidly changing Mach number and density near the body.

Since the purpose of this study is to investigate the suitability of the algorithm in applications to hypersonic flows, it is only fitting to discuss the problems encountered in the calculations. The most striking limitation of the technique is its sensitivity to the starting solution. Although the results are independent of the initial conditions, the stability is. Therefore it is necessary to creep up in angle of attack until the desired conditions are attained. Numerous attempts to bypass this process have not proven successful. The sensitivity appears to originate from the wall boundary conditions. When the numerical dissipation scheme was altered, the solution to the original code could not be used as the starting solution for the calculation on the new code with the modified dissipation. The whole process of creeping up in angle of attack from 0° had to be repeated, even though the final solutions appear similar between the two different versions of the code. On the contrary, when the grid was altered so that the stretching in the body normal direction was changed, but the code was left unaltered, the solution to the original grid resulted in a stable starting solution for the calculation on the the new grid. It seems probable that changing the grid structure resulted in a less drastic change to the boundary conditions at the wall than modifying the numerical dissipation.

The other issue of stability concerns the discrete time-step adopted in the temporal integration process. Since this is a steady state calculation, the ideal time-step should be defined by the flow and grid variables in the locality of the cell in equations 3.22 and 3.23. Such a time-step would lead to the fastest rate of convergence. Unfortunately when this was formulation was adopted in the semi-implicit code, instability results. [Loyd] [17] found it necessary to restrict the time step to a streamwise constant value to attain stability. In the present calculations, the re-

131

striction was relaxed somewhat, to a circumferentially constant value of the time step, so that Δt was a function of i and j only. Potentially significant improvements could be made if a truly local time-step can be used.

In hypersonic calculations where strong shock are encountered, excessive pressure overshoots are a constant problem. The present dissipation scheme requires a high second-order damping coefficient to suppress the problem. However such a high value for the coefficient raises issues of excessive numerical dissipation leading to the corruption of the results. In an attempt to overcome these problems, two other techniques were tried. The first was a shock fitting algorithm developed by [Blottner & Larson][4]. The scheme worked well with inviscid calculations on the circular cone, giving accurate results with the minimum number of grid points. The savings in grid points result from the use of the outer boundary as the shock front so that all the nodes fall within the region between the body and the shock. Furthermore it solved the problem of excessively high second order dissipation coefficient. Preliminary calculations using this technique showed that on a circular cone at 10° angle of attack, the second order dissipation coefficient needed was 0.05. It demonstrated that the main problem with calculations at hypersonic speeds is the need to capture the primary shock without adding too much dissipation in other regions. However the scheme had a number of problems. Firstly, the technique was not stable for the more complex geometry of the wing. Secondly, the shock had to be allowed to move without any restrictions. The second condition results in a final grid with a substantial degree of skewness. While this may be acceptable for an inviscid calculation, it will lead to poor Navier-Stokes results. As a consequence of these difficulties, the scheme was abandoned.

The alternative was to sick with a shock capturing technique with a dissipation scheme that was more suitable for capturing strong shocks. The flux limited dissipation scheme [Jameson][11] that could damp out pressure overshoots in the regions of strong shock was tested. This scheme modifies the code so that it could potentially

be total variation diminishing (TVD). The technique produces reasonably good results, but did not show any significant improvement over the original dissipation scheme. A decision was made to go with the original scheme but to leave the flux limited dissipation option within the present code.

In the present calculation, the thin layer approximation was used. This resulted in savings in CPU time and memory requirements. The approximation was justified by the assumption that changes in the body-tangential directions within the boundary layer were small. Away from the boundary layer where these components become significant, the viscous terms are overwhelmed by artificial dissipation and the inclusion of the tangential terms would not improve the quality of the results. However the present calculations indicate that the body-tangential components may not totally insignificant within the boundary layer and full Navier-Stokes calculations would help clarify the justifiabilty of the thin layer approximations.

The cell-centered scheme has inherent stability problems that make it difficult to obtain a starting solution. A more robust scheme must be adopted if we are to overcome the problems encountered above. The restricted stability of the semi-implicit formulation may have the same origins. However the semi-implicit technique shows strong promise and further study is necessary to realize its potential. More work also needs to be done in the area of artificial viscosity formulation. The present technique is inadequate for the needs of hypersonic flows. Even at a moderate speed of Mach 7.15, the applicability of the current dissipation scheme is stretched to its limit. Various schemes being developed recently show promise. Examples of such developments include [Radespiel & Swanson][19], [Deese et al.] [5] and [Siclaric et al.][24]. A suitable artificial viscosity model would significantly advance the goal of creating a suitable algorithm for hypersonic flows.

Bibliography

[1] Anderson, D. A., Tannehill, J. C. and Pletcher, R. H. :*Computational Fluid Mechanics and Heat Transfer*, Hemisphere Publishing Coporation, 1984.

[2] Anderson, J. D. Jr :*A Survey of Modern Research in Hypersonic Aerodynamics*, AIAA Paper # 84-1578.

[3] Beam, R. M. and Warming, R. F.: *An Implicit Factored Scheme for Compressible Navier-Stokes Equations* AIAA Journal, Vol 16, No. 4, April 1978.

[4] Blottner, F. G. and Larson, D. E. : *Navier-Stokes Code NS3D for Blunt Bodies, Part 1: Analysis, Results and Verification*, SAND88-0504/1, March '88

[5] Deese, J., Agarwal R. and Geilda T. :*Computation of Supersonic Viscous Flow About Missiles and Bodies at High Angles of Attack Using PNS and Navier-Stokes Solvers*, AIAA-89-0527.

[6] Eriksson, L.-E. and Rizzi, A.:*Analysis by Computer of the Convergence to Steady State of Discrete Approximations to the Euler Equations* AIAA Paper 83-1951 in Proceedings of AIAA Computational Fluid Dynamics Conference, Denvers, 1983.

[7] Goodsell, A. M.:*3-D Euler Calculations of Vortex Flows over Delta Wings* Master's Thesis, Massachusetts Institute of Technology, CFDL-TR-87-6, July 1987

[8] Hayes, W.D., Probstein, R. F.:*Hypersonic Flow Theory* Academic Press, 1959.

[9] Jameson, A., Schmidt, W., and Turkel, E.:*Numerical Solution of the Euler Equations Using Runge-Kutta Time Stepping Schemes*, AIAA Paper 81-1259, 1981

[10] Jameson, A.:*Solution of the Euler Equations by a Multigrid Method*, Applied Math and Computation, 13:327-356, June 1983.

[11] Jameson, A: *A Non-Oscillatory Shock Capturing Scheme Using Flux Limited Dissipation*, MAE Report # 1653, 1984, Princeton University

[12] Jameson, A. , Baker, T.J.:*Solution of the Euler equations for complex configurations*. AIAA Paper 83-1929CP, in AIAA Computational Fluid Dynamics Conference Proceedings, 1983.

[13] Jameson, A. , Lax, P. D.:*Conditions for the Construction of Multi-Point Total Variation Diminishing Difference Schemes*. MAE Report 1650, April 1984, Princeton University

[14] Jones, D.J.,:*Tables of inviscid supersonic flow about circular cones at incidence* $\gamma = 1.4$. Neuilly-sur-Seine, France, NATO, Advisory Group for Aerospace Research and Development, 1969.

[15] Kuethe, A. M., Chow, C. Y. :*Foundations of Aerodynamics, Bases of Aerodynamic Design, Fouth Edition*, John Wiley and Sons, 1986

[16] Loyd, B., Murman, E. M.and Abarbanel, S. S. :*A Semi-Implicit Scheme For The Navier-Stokes Equations*, 7th GAMM Conference on Numerical Methods in Fluid Mechanics, Louvain-la-Neuve, Belgium, Sept. 11, 1987.

[17] Loyd, B. :*A Semi-Implicit Navier Stokes Solver and its Application to a Study of Separated Flow about Blunt Delta Wings*, PhD Thesis, M.I.T., 1988.

[18] Press, W. H., Flannery, B. P., Teukolsky, S. A., Vetterling, W. T. :*Numerical Recipes, The Art of Scientific Computing* , Cambridge University Press, 1986.

[19] Radespiel, R. and Swanson, R. :*An Investigation of Cell Centered and Cell Vertex Schemes for the Navier-Stokes Equations*, AIAA-89- 0548.

[20] Rizik, Y., Chaussee, D. and Steger, J. :*Numerical Simulation of the Hypersonic Flow Around Lifting Vehicles*, NASA Technical Memorandum 89444.

[21] Roberts T. W. :*Euler equation computations for the flow over a hovering helicopter rotor*. PhD thesis, Massachusetts Institute of Technology, 1986.

[22] Sears, W. R. (editor) :*General theory of high speed aerodynamics*, volume 6, High speed aerodynamics and jet propulsion, Princeton University press, 1954.

[23] Shang, J. S. and Scherr, S. J. :*Navier-Stokes Solution of the Flow Field Around a Complete Aircraft*, AIAA-85-1509-CP, 1985.

[24] Siclari, M.J., DelGuidice, P. and Jameson A. :*A Multigrid Finite Volume Method for Solving the Euler and Navier-Stokes Equations for High Speed Flows*, AIAA-89-0283.

[25] Strang, G. :*Introduction to Applied Mathematics*, Wellesley-Cambridge Press, 1986.

Appendix A

Input for Euler equation solver.

```
'25 SEPT 89'          DATE   - Date
7.15                  MACH   - Mach number
30.                   AOA    - Angle of attack
0.                    YAW    - Yaw
1.4                   GAM    - Ratio of specific heats
1.5                   KAP2   - 2nd order dissip coef(0.02)
0.005                 KAP4   - 4th order dissip coef(0.005)
.false.               FLD    - If .true. then use flux limited dissipation
0.  0.                       - Add'l smoothing at bow shock (set to 0)
1.5                   CFL    - CFL number
0.0                   AENTH  - Enthalpy damping -- NOT USED
1000                  ITMAX  - Maximum iteration
50                    ITCOEF - Iteraton interval for coef.  output
50                    ITPRIN - Iteration interval for saving state vector
.TRUE.                BIN    - True = binary input/output
.TRUE.                CFBIN  - Force coefficient calculation
1                     ITER   - Starting iteration
1                     ICON   - ILOW 1=> lower angle solution, 0 => freestream
1.0                   EPSR   - Residual smoothing cefficient (1.0)
0.05                  RGRD   - Shock moving constant -- NOT USED
'test.gri'            GRNAME - Grid file
'regrd.gri'           RGNAME - Shock fitted grid file
'sires.dat'           RSNAME - Residuals
'siplt.dat'           STNODE - Output for Iris
'sisve.dat'           SVNAME - State vectors saved for restart
'sicof.dat'           CFNAME - Force Coeficients
'sirst.dat'           RESTRT - Restart file: old state vectors
'siinp.dat'           INPDAT - Copy of input dat
'junk'                LOWANG - Lower angle solution -- NOT IMPLEMENTED
'oldres.dat'          OLDRES - Old residuals
'freestream' cones.sol'CONSOLN- Conical starting solution -- NOT USED
.false.               SEMIIMP- Semi-implicit = true, explicit = false
0.005                 MUSI   - Implicit smoothing coefficient ~.005
0.                    REYNUM - Re=physical/mach number, inviscid = 0
74.,  288.            Tinf,Twall - Temp at inf , wall (if 0 -- adiabatic)
.72, .9               PR,PRT - Laminar, turbulent Prandtl number
```

Appendix B

Input for semi-implicit Navier-Stokes solver.

```
'25 SEPT 89'             DATE    - Date
7.15                     MACH    - Mach number
30.                      AOA     - Angle of attack
0.                       YAW     - Yaw
1.4                      GAM     - Ratio of specific heats
1.                       KAP2    - 2nd order dissip coef(0.02)
0.005                    KAP4    - 4th order dissip coef(0.005)
.false.                  FLD     - If .true. then use flux limited dissipation
0.  0.                           - Add'l smoothing at bow shock (set to 0)
.5                       CFL     - CFL number
0.0                      AENTH   - Enthalpy damping -- NOT USED
1000                     ITMAX   - Maximum iteration
50                       ITCOEF  - Iteraton interval for coef.  output
50                       ITPRIN  - Iteration interval for saving state vector
.TRUE.                   BIN     - True = binary input/output
.TRUE.                   CFBIN   - Force coefficient calculation
1                        ITER    - Starting iteration
1                        ICON    - ILOW 1=> lower angle solution, 0 => freestream
1.0                      EPSR    - Residual smoothing coefficient (1.0)
0.05                     RGRD    - Shock moving constant -- NOT USED
'test.gri'               GRNAME  - Grid file
'regrd.gri'              RGNAME  - Shock fitted grid file
'sires.dat'              RSNAME  - Residuals
'siplt.dat'              STNODE  - Output for Iris
'sisve.dat'              SVNAME  - State vectors saved for restart
'sicof.dat'              CFNAME  - Force Coeficients
'sirst.dat'              RESTRT  - Restart file: old state vectors
'siinp.dat'              INPDAT  - Copy of input dat
'junk'                   LOWANG  - Lower angle solution -- NOT IMPLEMENTED
'oldres.dat'             OLDRES  - Old residuals
'freestream' cones.sol'CONSOLN- Conical starting solution -- NOT USED
.true.                   SEMIIMP- Semi-implicit = true, explicit = false
0.005                    MUSI    - Implicit smoothing coefficient ~.005
818.182e3                REYNUM  - Reynolds number = physical/mach number
74.,   288.              Tinf,Twall - Temp at inf , wall (if 0 -- adiabatic)
.72, .9                  PR,PRT  - Laminar, turbulent Prandtl number
```